CHEMICAL REVIEWS

pubs.acs.org/CR

Review

Plate-Like Colloidal Metal Nanoparticles

Leonardo Scarabelli,* Muhua Sun, Xiaolu Zhuo, Sungjae Yoo, Jill E. Millstone,* Matthew R. Jones,* and Luis M. Liz-Marzán*

Cite This: *Chem. Rev.* 2023, 123, 3493−3542

Read Online

ACCESS | Metrics & More | Article Recommendations

ABSTRACT: The pseudo-two-dimensional (2D) morphology of plate-like metal nanoparticles makes them one of the most anisotropic, mechanistically understood, and tunable structures available. Although well-known for their superior plasmonic properties, recent progress in the 2D growth of various other materials has led to an increasingly diverse family of plate-like metal nanoparticles, giving rise to numerous appealing properties and applications. In this review, we summarize recent progress on the solution-phase growth of colloidal plate-like metal nanoparticles, including plasmonic and other metals, with an emphasis on mechanistic insights for different synthetic strategies, the crystallographic habits of different metals, and the use of nanoplates as scaffolds for the synthesis of other derivative structures. We additionally highlight representative self-assembly techniques and provide a brief overview on the attractive properties and unique versatility benefiting from the 2D morphology. Finally, we share our opinions on the existing challenges and future perspectives for plate-like metal nanomaterials.

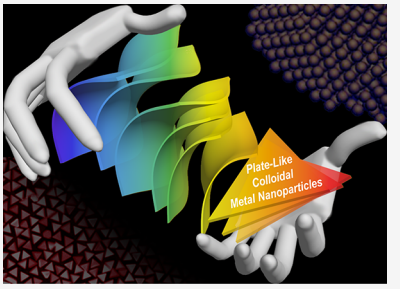

CONTENTS

1. Introduction 3494
1.1. Motivation 3494
1.2. Geometry of a Nanoplate 3494
2. Mechanistic Components of Nanoplate Synthesis 3494
2.1. General Considerations for *fcc* Crystals 3494
2.2. The Role of Seeds as Precursors 3496
2.3. The Role of Twinning in Plate Growth 3497
2.4. The Role of Ligands in Plate Formation 3498
2.5. Plasmon-Mediated Nanoplate Growth 3500
2.6. Use of Nanoplates as Scaffolds for Colloidal Growth 3500
2.6.1. General Processes in Postsynthetic Modification of Metal Nanoplates 3500
2.6.2. Nanoislands on Nanoplates 3502
2.6.3. Nanoframes 3504
2.6.4. Epitaxial Growth 3504
3. Other Crystal Lattices and Compositions 3505
3.1. *fcc* Metals 3505
3.1.1. Copper 3506
3.1.2. Palladium 3507
3.1.3. Platinum 3508
3.1.4. Nickel 3509
3.1.5. Rhodium 3510
3.1.6. Aluminum 3511
3.1.7. Iridium 3511
3.1.8. Lead 3511
3.1.9. Ytterbium 3512
3.2. *hcp* Metals 3512
3.2.1. Magnesium 3513
3.2.2. Cobalt 3514
3.2.3. Zinc 3514
3.2.4. Ruthenium 3514
3.3. *bcc* Metals 3515
3.3.1. Lithium 3515
3.3.2. Iron 3516
3.4. Metals with Other Crystallographic Habits 3516
3.4.1. Indium 3516
3.4.2. Bismuth 3516
4. Self-Assembly 3517
5. Properties and Applications 3519
5.1. Plasmonics/Optics 3519
5.1.1. LSPR Modes and Characterization 3519
5.1.2. Spectroscopies 3522
5.1.3. Sensing 3523
5.2. Catalysis 3524
5.3. Magnetism 3525
5.4. Mechanics 3526
6. Summary and Prospects 3526
Author Information 3527
Corresponding Authors 3527
Authors 3528
Author Contributions 3528
Notes 3528
Biographies 3528

Special Issue: Anisotropic Nanomaterials

Received: January 14, 2023
Published: March 22, 2023

https://doi.org/10.1021/acs.chemrev.3c00033
Chem. Rev. 2023, 123, 3493−3542

Acknowledgments 3529
Abbreviations 3529
References 3529

1. INTRODUCTION

1.1. Motivation

Since the earliest days of nanoparticle synthesis, anisotropic morphologies have appeared as reaction products, typically in small numbers compared to spherical particles.[1,2] Indeed, the citrate-based reduction of $HAuCl_4$ to generate gold colloids developed by Turkevich and co-workers included numerous anisotropic particle impurities in the original 1951 publication (see Figure 1A).[1] Despite many decades of progress in colloid chemistry, it was not until the early 2000s that multiple groups reported high-yielding colloidal syntheses of anisotropic metal nanostructures with high uniformity: Xia and co-workers for Ag cubes,[3] Murphy and El-Sayed and co-workers for Au rods,[4,5] and Mirkin and co-workers for Ag plates.[6] Since these initial findings, dozens of additional shapes have been reported, representing an explosion in the field of synthetic nanochemistry.[7−13]

Interestingly, although rod-shaped particles have generally garnered the most attention,[5,14,15] plate-shaped particles are appealing for numerous reasons relating to their unique morphology and properties. For example, because many nanoscale phenomena arise from particle shape, the degree to which a particle is anisotropic can be taken as a measure of the tunability of shape-dependent properties. Because for a given aspect ratio, nanoplates are more anisotropic compared to rods (see section 1.2), their properties will span a larger range of values and therefore be more easily tuned as a function of particle morphology. In addition, mechanistic understanding of nanoplate formation and growth is perhaps the most well-developed of any metal nanostructure (see section 2), allowing for greater predictive power in synthetic and postsynthetic reactions.

Although early synthetic work centered on gold and silver, an extensive library of different metals can now be generated as plate-like particles, expanding the set of available properties (see section 3). Furthermore, nanoplates are capable of self-assembling into well-defined superlattices (see section 4), with symmetries and dimensionalities that are quite different from those formed by other anisotropic particles.[16] Finally, the planar morphology of nanoplates leads to a variety of interesting plasmonic,[17] mechanical,[18] and catalytic properties (see section 5) that highlight the importance of plate-like metal nanomaterials as components in future nanoscale devices.

In this review, we explore the current state of the art in the formation, properties, and applications of metal nanoplates. We have restricted ourselves to solution-phase colloidal methods of synthesis, to distinguish these nanomaterials from planar thin films formed by evaporation or other deposition methods. Although the structures discussed herein are pseudo-two-dimensional, we take care to avoid discussion of so-called "two-dimensional materials" like graphene, transition metal dichalcogenides, and other exfoliated van der Waals structures which have been covered in excellent review articles recently.[19−24] We intended to take a critical view on the current state of the art, while attempting to unify or at least find similarities between proposed mechanisms and their outcomes. Finally, an outlook is provided to indicate our own view on where the field is going and what remains to be achieved, for a complete understanding of nanoplate growth and practical application of these exciting materials.

1.2. Geometry of a Nanoplate

Here, we define a nanoplate as an object extended in two dimensions and shortened in a third one, i.e., having an aspect ratio (edge length/thickness) greater than 1, with at least one dimension smaller than 100 nm. Nanoplates are among the most anisotropic structures available, which can be shown mathematically by defining a parameter called "anisotropicity" (α), as follows:

$$\alpha = 1 - \Psi = 1 - \frac{\pi^{1/3}(6V_p)^{2/3}}{A_p}$$

where V_p and A_p are the volume and surface area of the particle, respectively. Ψ is the "sphericity" of an object, which compares the surface area of a shape to the surface area of a sphere with the same volume. Because a sphericity of 1 indicates a perfect sphere, $1 - \Psi$ indicates the deviation from a perfect sphere, i.e., the anisotropicity. Comparison of rod and plate-shaped objects, both with a circular cross-section, shows that the two-dimensional structure maximizes anisotropicity for a given aspect ratio and is therefore expected to provide the greatest degree of property control (Figure 1).

2. MECHANISTIC COMPONENTS OF NANOPLATE SYNTHESIS

Plate-like nanostructures with many different compositions have now been synthesized (see section 3), but for all but the simplest of systems, there remain many questions regarding the mechanistic details of the reaction. A prevalent theory to explain the emergence of many types of anisotropic growth is the "facet-selective adsorption hypothesis", in which an organic ligand is thought to bind to a particular crystal facet selectively, lowering its surface energy (thermodynamic control) or slowing the rate at which new material is added (kinetic control) relative to the other facets.[25−29] For materials whose atomic lattice is described by the hexagonal close packed (*hcp*) crystal system, this hypothesis straightforwardly explains the appearance of a single-crystalline plate-like morphology because the natural asymmetry between the *a* and *c* axes of the unit cell leads to different surface features and ligand adsorption properties along two dimensions, relative to the third.[30] However, the vast majority of literature examples of nanoplate particles possess highly symmetric crystal structures (e.g., face-centered cubic, *fcc*), which require a breaking of the unit cell symmetry to generate a 2D particle. Consequently, the mechanistic processes that generate these particles remain the subject of ongoing research. In the following section, we focus the discussion on the case of *fcc* metals, which represent the benchmark for shape-controlled colloidal growth; other crystal structures will be analyzed in section 3 of this review.

2.1. General Considerations for *fcc* Crystals

For *fcc* metals, atoms are arranged in a close-packed *ABCABC* stacking along the [111] direction (Figure 2A,B), implying a coordination number (CN) of 12 for each internal atom. The three low-index surfaces, {111}, {100}, and {110}, present CNs of 9, 8, and 7, respectively (Figure 2C−E). A higher CN translates into a higher planar density and, ultimately, into a lower surface energy γ, identifying a clear order of decreasing stability as surface energy increases, i.e., $\gamma_{\{111\}} < \gamma_{\{100\}} < \gamma_{\{110\}}$.[31,32] As mentioned in the previous paragraph, the

https://doi.org/10.1021/acs.chemrev.3c00033
Chem. Rev. 2023, 123, 3493−3542

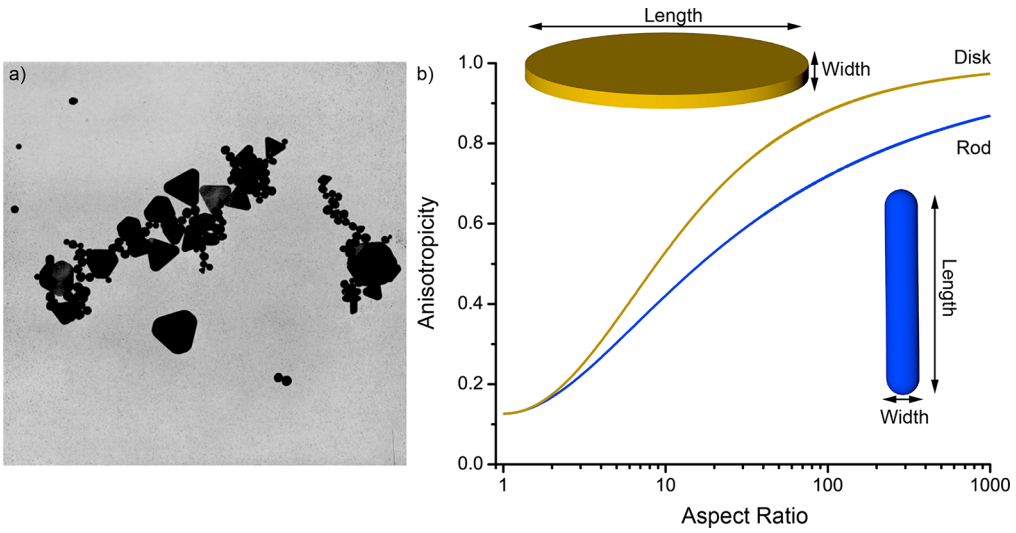

Figure 1. (a) Image from original 1951 Turkevich paper on gold nanoparticle synthesis showing numerous anisotropic nanoplate impurities. Magnification is indicated in the original manuscript as 50 000 diameters. Reproduced with permission from ref 1. Copyright 1951 Royal Society of Chemistry. (b) Calculation of anisotropicity value (α, defined in text) for a plate (gold solid line) and a rod (blue solid line) both with circular cross-section. Aspect ratio is defined as length/width.

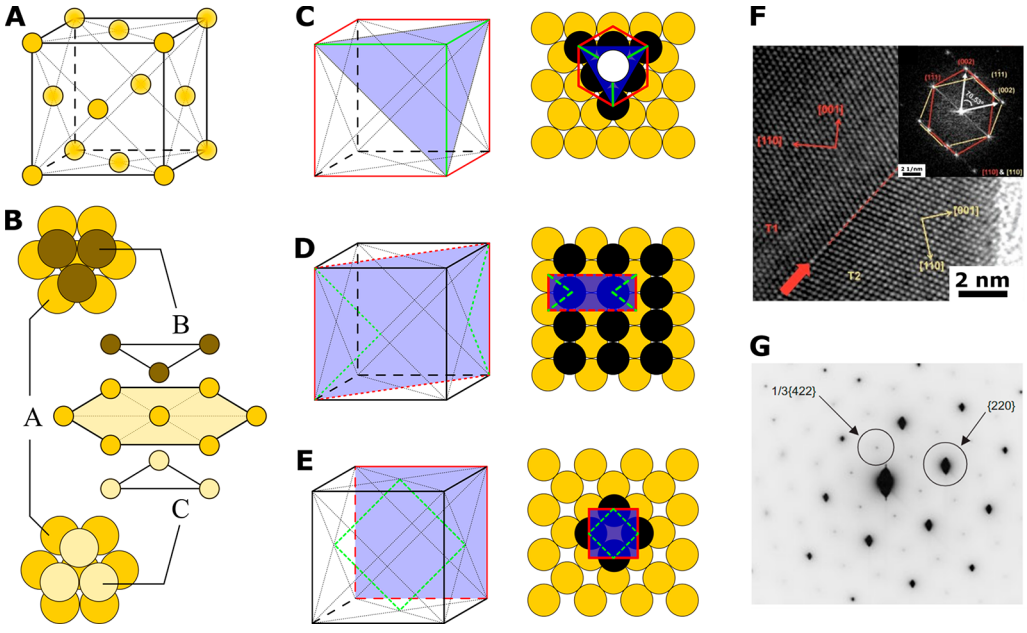

Figure 2. *fcc* crystallographic habit.[41] (A,B) Three-dimensional spatial arrangement of the unit cell in an *fcc* crystal. (C−E) Projection perspective (left) an top view (right) representations of the three main crystallographic directions in order of stability (from top to bottom) from the most stable: {111} (C), {100} (D), and {110} (E). (F) High resolution transmission electron microscopy (HRTEM) analysis of a nanocrystal presenting a single twin-defect. Adapted with permission from ref 37. Copyright 2016 Wiley-VCH. (G) Diffraction pattern of an *fcc* nanoplate, showing the forbidden that in 1/3{422} reflections, indicating the formation of stacking faults. Adapted with permission from ref 39. Copyright 2005 Wiley-VCH.

formation of platelets in *fcc* structures requires a symmetry breaking event.[33] The most common manner in which asymmetry is created for cubic crystal systems is the appearance of 2D defects called "twin planes".[34,35] Such defects appear when the ordinary stacking of planes along a particular crystal axis (i.e., ABCABC) is disrupted in a way that creates a plane with mirror symmetry (e.g., ABCBA). Although for most crystal structures and crystal planes such defects are highly unfavorable, for highly symmetric systems there is often a single family of planes for which twin formation is accompanied by a negligible energetic penalty. This is the case for the stacking of {111} planes along the [111] direction in an *fcc* crystal. Atoms located at twin defects of this type have the same coordination number as atoms in the perfect bulk crystal and, as a result, {111} twin planes appear frequently in *fcc* metal nanoparticles.

It is the intrinsic two-dimensionality of twin planes that is responsible for the symmetry breaking that gives rise to most of the two-dimensional nanoplates discussed in this review. It is important to note that there are two distinct plate-like *fcc* nanoparticle morphologies, both of which present extended {111} facets and appear identical in TEM images but can be differentiated by the details of their internal twinning. Although this distinction has largely been ignored in the literature, plate-like particles with a single twin plane have genuine mirror

https://doi.org/10.1021/acs.chemrev.3c00033
Chem. Rev. 2023, 123, 3493−3542

symmetry when viewed edge-on and are best described as truncated bipyramids.[36] However, particles with multiple parallel twins (sometimes referred to as "stacking faults" when they are closely spaced) lack perfect mirror symmetry but nonetheless appear plate-like; these will be referred to in this review as platelets. These two shapes are frequently confused because both can appear as pseudo-two-dimensional, with triangular cross sections, but can be distinguished by their selected area electron diffraction (SAED) patterns. Whereas diffraction from truncated bipyramids show a superposition of the same peaks but rotated with respect to each other in reciprocal space (Figure 2F),[37,38] platelets show forbidden 1/3{422} reflections (Figure 2G).[39,40] Although many of the mechanistic factors governing plate-like growth are similar for truncated bipyramids and platelets, differences in the cross-sectional shape (e.g., triangular, hexagonal, truncated triangular) of nanoplates can be traced to the number of internal twins (see section 2.3). The initial appearance of twins, the manner in which they act to maintain 2D growth after they have formed, and the role of surface ligands in promoting twin-based growth all constitute important mechanistic components of nanoplate synthesis that will be discussed below.

2.2. The Role of Seeds as Precursors

Essentially all syntheses of nanoplate particles follow a two-stage protocol in which nucleation and anisotropic growth processes are separated into distinct steps. Often referred to as seed-mediated growth, small nanoparticle "seeds" are first homogeneously nucleated by rapid reduction of a metal ion precursor, followed by a second reaction in which the seeds are used as heterogeneous nucleation sites for the slow and controlled deposition of additional metal ions. Given the primacy of twin defects in explaining the appearance of plate-like morphologies, considerable effort has been devoted to understanding the processes by which twins appear in the seed nanoparticles under the assumption that, once present, they will continue to drive 2D growth.

Most seed syntheses generate particles with a range of different twinning structures that can be described in three categories: single crystalline (zero twins), multiply twinned (5−20 twin planes), and planar twinned (1−4 twins).[7] Single crystalline particles are free of twin defects and are generally thought to evolve into polyhedral particles (e.g., cubes, octahedra, rhombic dodecahedra), the shape of which match the point group of the *fcc* unit cell (O_h symmetry).[33,42−46] Multiply twinned particles consist of a three-dimensional (3D) arrangement of twin defects that give rise to pentagonal decahedron and icosahedron-shaped particles (D_{5h} and I_h symmetry).[47,48] Planar twinned seeds consist of one to several twins spanning the entire length of the particle with the requirement that they all be parallel (C_3 symmetry).[47,49] Although it is this latter class of seeds that are thought to evolve into nanoplate morphologies, Mirkin and co-workers have shown that Au nanoplates can form from a variety of seeds that lack twin planes, including some that are nonspherical or even consist of different compositions and crystal structures (e.g., CdSe).[50] However, in that case, it is believed that the added seed particle is not playing the role of a heterogeneous nucleation site but instead is acting as a catalyst for the *in situ* formation of planar twinned particles that ultimately grow into plates. In aggregate, these studies suggest that increasing the population of planar twinned particles in the seed solution will increase the yield and uniformity of nanoplates in the final growth reaction product.

Although it has been identified that stacking faults in seed particles are a key factor in dictating the 2D growth behavior of nanoplates, the genesis of twin defects is a topic much less studied than their growth-promoting effects. Historically, there have been two schools of thought regarding the formation of twin defects. The first school posits that the seed particle is twinned itself, while the second perspective suggests that twins arise naturally due to errors in the stacking of {111} planes during growth.[33,51,52] The latter is often referred to as the "growth accident hypothesis." If the "growth accident hypothesis" is appropriate, then one might suppose that twinning is a purely stochastic event, which is contradictory to the experimental observations that lamellar twins already exist in seed particles and the population of twinned seeds is comparable to that of the resultant nanoplates when a purification procedure is not applied. Thus, the formation of twins during the nucleation stage may be considered a deterministic process.

Further research is needed to elucidate the mechanisms for twin nucleation. For example, according to classical nucleation theory, small particles formed via homogeneous nucleation have fluctuating structures that stabilize once their size surpasses a critical value. However, it is known that Au and Ag particles less than ∼2 nm typically exist as so-called "nanoclusters", which are distinguished from nanoparticles in that they consist of a precise number of metal atoms and surface ligands. An enormous variety of metal nanoclusters have been discovered,[53−56] including an interesting example by Jin and co-workers, who demonstrated the existence of an Au_{56} compound with a triangular nanoplate structure and Br^- surface ligands.[57] This finding provides the first suggestion that the nanoplate morphology may be established in particles that are atomically precise and ∼1 nm in size.[57] In addition, a recent report by Jones and co-workers has shown that many of the "seed" particles used in anisotropic nanoparticle syntheses are actually atomically precise nanoclusters capped by quaternary ammonium surfactants.[58] These examples suggest that the energy landscape for sub-2 nm seeds is highly complex and discontinuous with particle size, making the predictive synthesis of structures with a desired (planar) twinning structure a grand challenge for the field. To answer the above questions, we must harness the new capabilities in both *in situ* imaging and *ex situ* characterization methods. Beyond those state-of-art techniques, we note that liquid cell TEM has gained attraction in the nanomaterials community because it permits the direct observation of subcritical nuclei in solution.[59−62] This method would enable researchers to capture, identify, and monitor such nuclei with the necessary temporal resolution. Such information would be invaluable in correlating synthetic parameters with nuclei and eventual nanocrystal structures.

Despite the fact that most seed syntheses generate a mixture of single crystalline, multiply twinned, and planar twinned particles, several particle growth protocols have shown that nanoplates can be formed in nearly quantitative yield. As a result, it must be concluded that certain conditions can favor the formation of planar twinned seeds and extensive effort has been applied to understanding how this occurs. To ensure tight control over the population of seeds with different internal twinning structures, both thermodynamic and kinetic factors must be considered.[63] In a pioneering work by Xia et al., a method was developed to quantitatively analyze the reaction kinetics involved in a polyol synthesis of noble-metal nano-

https://doi.org/10.1021/acs.chemrev.3c00033
Chem. Rev. 2023, 123, 3493−3542

crystals and revealed a quantitative correlation between the initial reduction rate and the twining structure taken by seeds and nanocrystals.[52] With Pd as an example, they showed that simple spectroscopic measurements could reveal kinetic parameters involved in the reduction of $PdCl_4^{2-}$ by a polyol, including the rate constant, activation energy, and initial rate. By manipulating the initial reduction rate, Pd nanocrystals with distinct defect structures, including single crystal, multiply twinned, and stacking-fault-lined, could be deterministically obtained in high purity (Figure 3A).

An alternative hypothesis is that the as-synthesized seeds are unavoidably heterogeneous in their twinning structure, but certain species are more susceptible to oxidation than others and the conditions being used in high-yield nanoplate reactions select for the planar twinned seeds.[64] In the synthesis of high-purity Au nanoplates, Zhang et al. demonstrated that iodide ions could selectively remove (during growth) other less stable shape impurities through oxidative etching by forming I_3^-, while facilitating the formation of nuclei with a dominant planar twinned structure (Figure 3B).[65] Based on this oxidative etching synthetic route, they achieved monodispersed triangular Au nanoplates with high morphological yield above 90%, in a rapid one-pot growth. Separately, Yin et al. introduced an oxidant (H_2O_2) in the synthesis of Ag nanoplates and revealed that H_2O_2 favors the production of Ag nanoplates by inducing the formation of planar twin defects and removing other less stable structures.[27] By harnessing the oxidative power of H_2O_2, various Ag sources including metallic Ag can now be directly converted to Ag nanoplates with the assistance of an appropriate capping ligand, thus significantly enhancing the reproducibility as well as the shape yield of the nanoplate synthesis. However, it should be pointed out that single crystals are more resistant to oxidative etching than twinned particles with less stable features at their surface.[64] Therefore, oxidative etching should be controlled in such a way as to remove single crystal structures and leave behind twin defects in the nanocrystals.[64,66] Generally, the population of twinned seeds can be increased by (i) removing O_2 from the reaction system by bubbling an inert gas through,[66] and (ii) blocking oxygen adsorption to the seeds through the selection of suitable capping agents (e.g., citrate). The control of defect formation in seeds was proven extremely successful in improving the yield and size dispersity of both single-crystal and penta-twinned nanoparticles;[43,45,47,67,68] However, a direct synthesis of exclusively planar twinned Au seeds remains elusive.

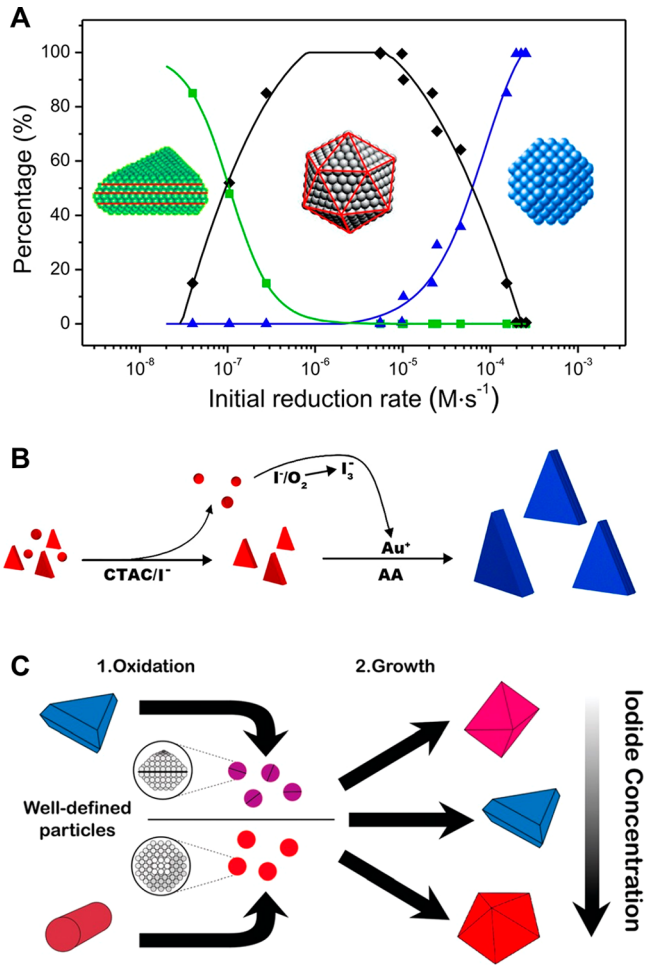

Figure 3. (A) Plot showing the relative distribution of the twin structure of Pd nanocrystals as a function of the initial reaction rate (r_0) in a synthesis. Reproduced with permission from ref 52. Copyright 2015 American Chemical Society. (B) Proposed growth pathway of Au nanoplates through oxidative etching. Reproduced with permission from ref 65. Copyright 2014 American Chemical Society. (C) Schematic representation of the experimental procedures for oxidative etching of Au nanoplates and Au nanorods to obtain seeds with selected size (12 and 20 nm) and crystallinity (monotwinned and single-crystal), and subsequent seeded growth under specific conditions (different iodide concentrations) to investigate the effect of size and twinning on the shape evolution of Au nanoparticles. Reproduced with permission from ref 46. Copyright 2017 Royal Society of Chemistry under CC BY-NC 3.0.

To further elucidate the formation mechanism of twin defects and their impact on shape yield, Liz-Marzán and co-workers attempted to disentangle the effect of size and twinning on the shape evolution of Au nanoparticles under optimized reaction conditions. Specifically, "enriched" planar twinned seeds of different diameters were prepared through careful oxidation of presynthesized and purified Au nanotriangles and were subsequently grown using identical growth conditions as those designed for single-crystal, planar-twinned, and penta-twinned products (Figure 3C).[46] The authors found that the introduction of twin defects during growth in a single-crystal structure becomes significantly harder (i.e., more energetically demanding) for larger 20 nm seeds compared to 12 nm seeds. The systematic investigations in this work suggested that optimization of protocols for better defined seeds toward the growth of Au nanoplates should focus on nanoparticles with larger diameter so as to achieve a better control over their crystallographic structure and evolution during growth.

2.3. The Role of Twinning in Plate Growth

Assuming the existence of planar twinned seeds, there must be separate processes that preserve the planar structure and promote plate-like growth over isotropic growth. Crystal twinning that leads to plate-like structures was first proposed by Berriman and Herz to account for the plate-like morphology of AgBr crystals.[69] Later, Lofton and Sigmund considered the similarity between the plate-like metal and metal halide morphologies, to propose an analogous explanation for the growth of Ag and Au nanoplates involving the formation of twin planes parallel to {111} faces.[39] In the simplest case of seed particles with a single twin, the resulting nucleus at the early stages of growth is a hexagonal plate due to the 6-fold symmetry of the *fcc* structure.[70] When viewing the side facets around the periphery of the hexagon, each of them will have alternating

https://doi.org/10.1021/acs.chemrev.3c00033
Chem. Rev. 2023, 123, 3493−3542

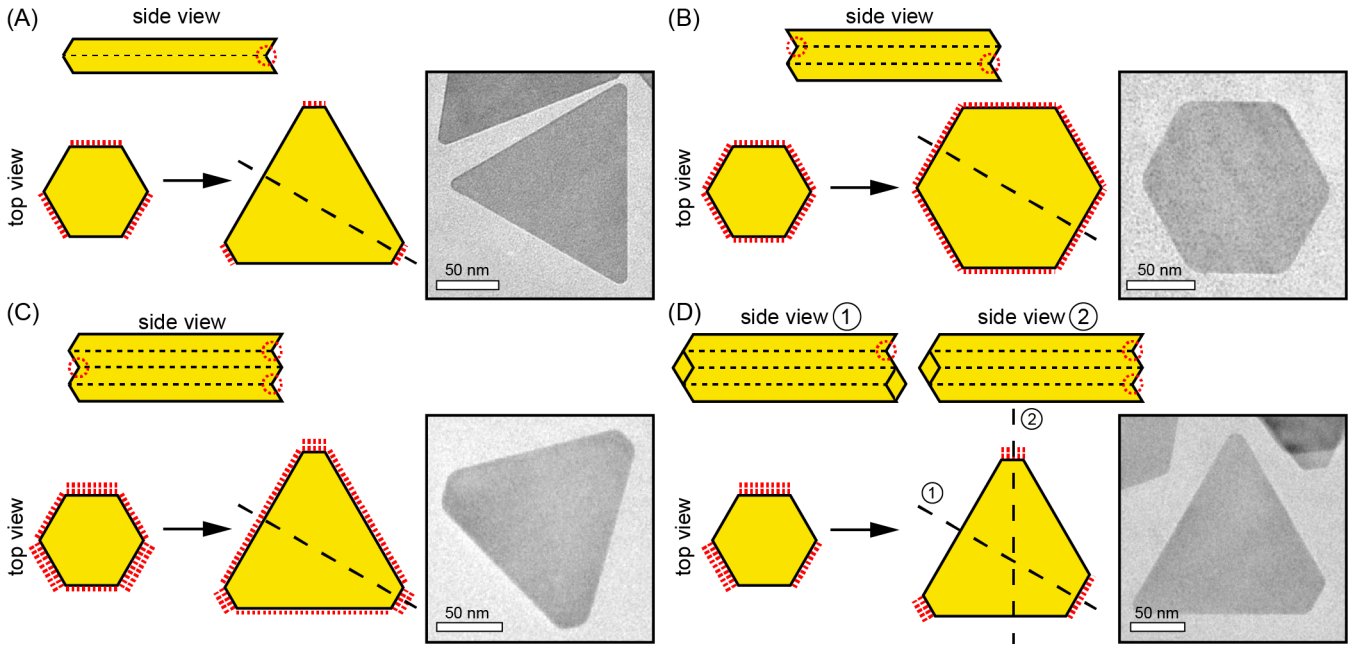

Figure 4. (A) Scheme showing the single-twin growth mechanism responsible for the formation of triangular platelets; concave and convex edges of the platelet are marked with "A" and "B," respectively. Reproduced with permission from ref 74 Copyright 2016 American Chemical Society. (B–D) Schematic illustrations of the (B) double-twinned growth mechanism of hexagons, (C) triply twinned primary growth mechanism of nonequilateral hexagons, and (D) secondary growth on triply twinned particles that yields nonagons or nonequilateral hexagons. Reproduced with permission from ref 75. Copyright 2011 American Institute of Physics. The red circles indicate the positions of re-entrant grooves.

concave or convex features because of the presence of the twin plane (Figure 4); the three concave sides are also called "re-entrant grooves". When atoms diffuse toward the nucleus and adsorb to the growing nanocrystal, attachment onto the concave sides will be preferred because their CN will be 4, compared to 3 on a flat {111} plane. On this basis, the concave sides grow selectively until a trigonal plate structure is reached (Figure 4A), at which point the concave re-entrant grooves have disappeared and the triangular shape is permanent.[71] This model has been corroborated in multiple independent reports of planar twin stacking faults parallel to the basal (111) planes being observed in metal nanoplates and can thus explain the observation of 1/3{422} forbidden reflections in SAED patterns oriented along the [111] zone axis.[40]

Interestingly, because nanoplates can contain multiple parallel twins, the evolution of the cross-sectional shape (triangular, hexagonal) can be more complicated. If a second twin plane is parallel to the first one, all six sides of the hexagonal nucleus will exhibit both a concave and a convex feature, equalizing the stabilization energy for adatoms and leading to a similar growth behavior along the six directions (Figure 4B), thereby maintaining the hexagonal cross-section. In this case, out-of-plane growth is still disfavored because atoms prefer to adsorb on concave surfaces rather than on flat surfaces. One can further imagine the effect of a third parallel twin plane where all six sides have at least one re-entrant groove, resulting in growth along all six directions but with different rates depending on the number and precise configuration of concave and convex features. These particles will yield truncated triangular or nonequilateral hexagonal nanoplates (Figure 4C,D). Such growth behaviors have been observed in liquid cell TEM observation of Au nanoplate growth at the single particle level, clearly illustrating the critical role of twin planes in dictating the actual evolution pathways of nanoplates.[72,73] Furthermore, this model suggests that the key to controlling the cross-sectional morphology of *fcc* metal nanoplates lies in developing synthesis methods that can control the number and placement of interior twins.

It is important to note that, to continuously sustain the growth rate differences between side facets and basal planes of nanoplates, it is essential to maintain a suitably low supersaturation of gold precursor during growth.[73] When under high supersaturation, the nucleation barrier can be overcome on any facet, resulting in the in-plane and out-of-plane growth of nanoplates occurring simultaneously, ultimately resulting in smaller and thicker particles with a reduced 2D anisotropy. This explains why syntheses for ultrahigh aspect ratio nanoplates add metal precursors into growth solutions dropwise or in several sequential steps to maintain a low supersaturation and promote a greater selectivity for side-facet vs thickness growth.[28]

2.4. The Role of Ligands in Plate Formation

Crystallography alone is not enough to guarantee *fcc* structured metals grow into 2D morphologies. Selective binding of ligands used in colloidal synthesis is a complementary element that may promote anisotropic growth, modifying both thermodynamic and kinetic factors.[76] The presence of capping ligands will change the surface energies of crystallographic planes, and the degree of their impact will depend on both the chemical nature of the ligand and the crystal facet onto which it adsorbs. A facet that is selectively adsorbed by certain capping agents would have surface atoms being stabilized, and therefore the corresponding surface energy would be lowered. On the other hand, surface ligands can also affect the shape of nanocrystals from the kinetic perspective. Instead of lowering the surface energy, the adsorption of a capping agent on certain crystal facets can pose a physical barrier to the surface. As such, the capping layer will slow down the deposition rate of metal atoms, additionally becoming a passivating layer that will retard the surface diffusion of adatoms. Both effects result in particles that present more of

https://doi.org/10.1021/acs.chemrev.3c00033
Chem. Rev. 2023, 123, 3493–3542

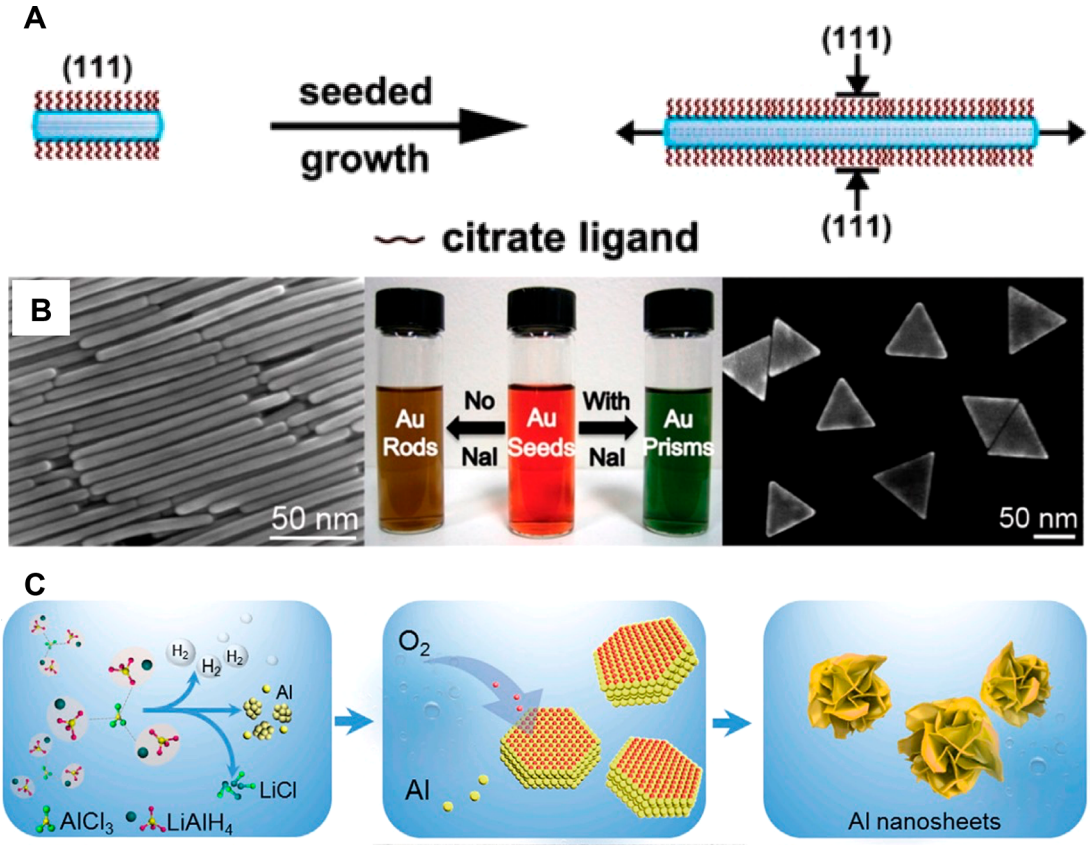

Figure 5. (A) Citrate ions selectively protect the {111} basal facets of Ag nanoplates and only allow lateral overgrowth. Reproduced with permission from ref 28. Copyright 2010 American Chemical Society. (B) Role of iodide ions in the growth of Au nanoplates enclosed by {111} facets: Presence of iodide ions leads to the formation of Au nanoplates through seeded-growth, while its absence yields nanorods when iodide-free CTAB is used as a surfactant. Reproduced with permission from ref 90. Copyright 2018 American Chemical Society. (C) Schematic illustration showing the synthesis of Al nanosheets, where selective binding of O_2 on {111} basal planes promotes the formation of ultrathin Al nanosheets. Reproduced with permission from ref 89. Copyright 2020 Cell Press.

the ligand-bound facet, but disentangling the dominant driving forces remains difficult.

Regardless of kinetic or thermodynamic drivers, slowing down the growth of well-passivated facets compared to the others, may facilitate plate-like growth. A typical example can be found in the synthesis of Ag nanoplates. In a classic synthesis, citrate bound preferentially to Ag(111) limits adadtom adsorption onto this facet and thereby hinders the increase in plate thickness (Figure 5A).[28] Mirkin and co-workers demonstrated that, by adjusting the ratio of Ag precursor to citrate, Ag nanoplates with controllable lateral dimension and thickness could be obtained.[77] A possible explanation for this tunability can be attributed to the match in symmetry and dimensions between citrate and the Ag(111) surface,[78] as it has also been reported that citric acid shows a better match and stronger binding to Ag(111) surfaces as well as Pd(111) facets.[79−81] Yin et al. also demonstrated that citrate can be replaced by other carboxyl compounds containing two carboxylate groups because the preferential binding affinity of such compounds is ascribed to the two nearest carboxylate groups, which are separated from each other by two or three carbon atoms.[27] In a recent paper, Wiley et al. quantified the effect of citrate to block atomic addition to certain facets by combining single-crystal electrochemistry measurements during anisotropic nanocrystal growth.[82] They showed that citrate lowers the rate of atomic addition to Ag(100) and Ag(111) single crystals by 3.2 and 15 times, respectively. They also pointed out that seeds with planar defects exhibit anisotropic growth that is 30−100 times greater than can be explained by a facet-selective passivation by citrate, which is consistent with the statement that 2D nanoplate formation cannot be explained by facet specific capping ligands alone.

The wet-chemical synthesis of Au nanoplates relies exclusively on the presence of iodide in the growth solution (Figure 5B). Mirkin et al. suggested that iodide preferentially binds to {111} facets of Au nanoplates, favoring anisotropic growth, which was also validated in a series of subsequent reports.[83−85] The effect of iodide was explored further by Liz-Marzán et al. in a double stage growth protocol. They found that the timing of iodide addition into the growth mixture plays an important role in maximizing shape yield. Specifically, by introducing a small amount of iodide during the first overgrowth stage, Au nanotriangles could be prepared with a shape-yield around 70% and an edge-length polydispersity below 10%.[86,87] Such an improvement of shape yield was ascribed to the early modification of the crystallographic structure of the seeds, which is essential to driving the symmetry-breaking event toward the development of a triangular shape. Selective passivation of facets by surface ligands also plays an important role in synthesizing other metallic nanoplates (see section 3). For example, Zheng et al. reported the synthesis of free-standing 2D Pd nanosheets and claimed that the strong adsorption of CO molecules on the basal (111) planes prevents growth along the [111] direction, thus being responsible for the formation of a

https://doi.org/10.1021/acs.chemrev.3c00033
Chem. Rev. 2023, 123, 3493−3542

sheet-like structure.[88] In the synthesis of sub-2 nm-thick Al nanosheets, it was found that the preferential adsorption of O_2 on the (111) plane of Al is crucial for the formation of 2D structures (Figure 5C).[89]

2.5. Plasmon-Mediated Nanoplate Growth

In 2001, Mirkin and co-workers discovered a light-driven synthesis of Ag nanoprisms. In this process, spherical Ag particles are converted into triangular nanoplates through a series of Ag redox cycles where oxidative dissolution of Ag particles produces Ag^+ ions, which are then reduced by citrate onto the Ag particle surface when irradiated with visible light (Figure 6A).[6] Brus and co-workers confirmed these findings and both Brus and Mirkin proposed that the photo-oxidation of citrate by plasmon generated "hot" holes creates a cathodic photovoltage on the seed particles, which in turn facilitates the reduction of Ag^+ onto the growing particles (Figure 6B).[91] Some of the most compelling evidence for the triangular nanoplates being generated by Ag^+ reduction is that, under appropriate conditions, the spherical Ag nanoparticle seeds can be replaced with a Ag^+ salt (most commonly, $AgNO_3$), and triangular nanoplates can still be produced.[92,93] This indicates that an important role of the Ag seed particles in this reaction is to provide a source of Ag^+ that can then be redeposited onto the growing Ag nanoplate structures. Interestingly, it has been pointed out that, when citrate was replaced by other chemically related molecules, such as citric acid, tricarballylate, citramalate, or aconitate in the spherical seed solution, the formation of triangular nanoplates seemed to be inhibited. The reason behind the effect of citrate in plasmon-mediated Ag nanoplates formation is not completely understood, but it might be consistent with the role of citrate in promoting the formation of twinned particles in wet-chemical syntheses of Ag nanoplates. In addition, although most studies have concluded that the conversion of spheres into nanoplates happens by a process of oxidation and redeposition of Ag, a recent liquid cell TEM work demonstrated that adjacent spherical particles can coalesce with each other under electromagnetic field enhancement and form large nanoplates (Figure 6C).[93] More recently, Zhai et al. also elucidated that a controllable plasmon-driven nanoparticle-coalescence mechanism could enable the production of well-defined anisotropic Ag nanoplates.[94] Au nanostructures are anticipated to provide an alternative system for exploring the plasmon-mediated growth process. Wei et al. demonstrated that when irradiating pseudospherical Au particles with 500 nm light for 2 h Au nanoplates were obtained with about 21% yield, consistent with the percentage of planar-twinned nanocrystals observed in the seed solution. This is a further confirmation that plasmon-mediated nanoplate growth is predominantly determined by the crystallographic structure of the seed particles, which is consistent with the mechanism underlying wet-chemical syntheses of Ag or Au nanoplates.[95]

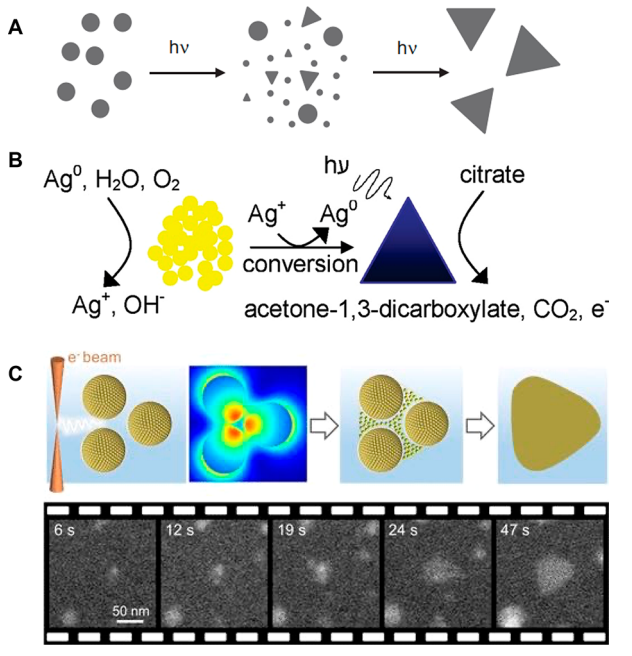

Figure 6. (A) Proposed photomediated growth pathways of Ag nanoplates from spherical nanoparticles. Reproduced with permission from ref 6. Copyright 2001 AAAS. (B) Proposed photovoltage mechanism for light conversion of citrate-stabilized Ag nanocrystal seeds into large nanoplates. Reproduced with permission from ref 91. Copyright 2008 American Chemical Society. (C) Liquid cell TEM observation of 2D nanoplate growth, mediated by plasmon-enhanced nanoparticle coalescence. Reproduced with permission from ref 93. Copyright 2020 American Chemical Society.

2.6. Use of Nanoplates as Scaffolds for Colloidal Growth

Given the exceptional optoelectronic and mechanical features of nanoplates, it is not surprising that significant research effort has been made to build heterostructures based on these particles as scaffolds. Such postsynthetic modifications can take many forms, but generally employ techniques from wet-chemical metal nanoparticle syntheses and leverage additional redox processes such as galvanic replacement reactions (GRR) and underpotential deposition (UPD). The outcomes of these synthetic techniques are influenced by properties of the metal substrate and the metal(s) added relative to one another. For example, the bond dissociation energy of the homometallic and heterometallic bonds, as well as the degree of lattice mismatch, are two important parameters that can direct the morphology of postsynthetic nanoplate modification. Building from nanoplate substrates, three broad classes of nanoheterostructures have emerged: nanoislands, nanoframes, and epitaxially grown structures, although within these classifications there can be overlap. As a summary, we list in Table 1 the results from postsynthetic modifications of metal nanoplates described in this section.

2.6.1. General Processes in Postsynthetic Modification of Metal Nanoplates. To contextualize the intrinsic and extrinsic factors that drive synthetic outcomes in postsynthetic modification of metal nanoplates, we briefly review common metal redox processes and metal deposition on metal thin films. As we have already seen in the initial synthesis of nanoplates, interactions between metal ions and reduced metal species can dramatically impact final particle outcomes. Two processes that are widely used for nanoplate modification are GRR and UPD. GRRs involve the oxidation of a zerovalent metal particle or substrate by an incoming metal ion of higher reduction potential.[96−101] UPD refers to the deposition of metal monolayer(s) on another metal substrate at a potential that is less negative than the equilibrium reduction potential of the depositing metal, and it is typically attributed to strong electronic interactions between substrate and depositing metal, which alter the reduction potential of the depositing metal from its bulk value.[102−104]

In addition to these redox processes, principles from thin film metal deposition can also predict outcomes in nanoplate

https://doi.org/10.1021/acs.chemrev.3c00033
Chem. Rev. 2023, 123, 3493−3542

Table 1. Summarized Outcomes and Proposed Driving Forces for Post-Synthetic Modifications of Metal Nanoplates Described in section 2.6

substrate materials	introduced elements	observed morphology	(proposed) driving force(s)	related refs
Au nanospheres	Pt	ultrathin Pt layers on Au nanoplates	VW growth modes due to Pt−Pt vs Pt−Au bond energies	109
Au nanoplates	Pt	Pt nanoislands on Au nanoplates		110, 111, 113, 115, 116, 117
Au electrode with (111) and (100) surface	Pt	Pt clusters on Au electrodes		112
Au cubes, octahedrons, and nanorods	Pt	Pt islands on Au nanoparticles		114
Ag nanoprisms	Au	triangular Au/Ag nanoframes	galvanic replacement	118,119
Ag nanoprisms	Au	particle-in-a-frame		120
Ag nanoprisms	Au	triangular Au nanoframes	FM growth modes due to Au−Au vs Ag−Au bond energies; galvanic etching	121
Pd nanosheets	Au	Au islands on Pd nanosheets and Au nanorings	VW growth modes due to Au−Au vs Pd−Au bond energies	122
Au nanodisks	Pt	Pt islands on Au nanodisks and PtAu nanorings	VW growth modes due to Pt−Pt vs Pt−Au bond energies	123
Au octahedrons	Ag, Pd	Pd and Ag nanocubes	FM growth modes due Ag−Ag vs Ag−Au, and Pd−Pd vs Ag−Au bond energies	124
Au nanoprisms	Au	Au nanoprisms with tunable edge lengths	FM growth modes due to lattice matching	125, 126,
Au nanoprisms	Au	Au hexagonal nanoplates		127, 128
Ag nanoprisms	Ag	Ag nanoplates with tunable edge length and thickness		129
Au nanodisks	Ag	dodecahedron and elongated polyhedral Au@Ag nanostructures	FM growth modes due to Ag−Ag vs Ag−Au bond energies	130
Au nanoprisms	Au	Au nanotripods	different redox potentials of nanoplate edges and tips	131
Au nanoplates, nanorods, octahedra, concave rhombic dodecahedra, decahedra	Au	corner-, edge-, deposited Au nanoparticles and aggregates	ligand-mediated surface blocking methods	132

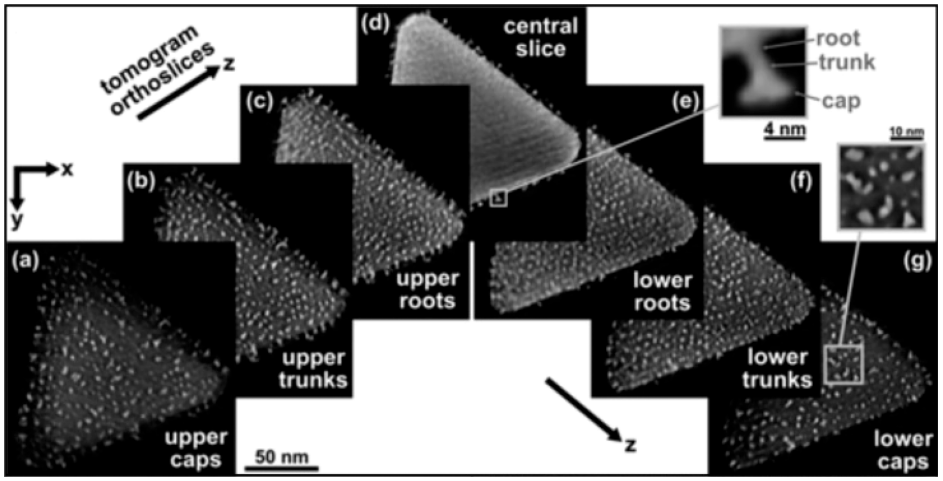

Figure 7. Tomographic sequential orthoslices of Pt islands in epitaxial contact with the Au nanoplate surface indicating the root, trunk, and cap island morphologies. Reproduced from ref 111. Copyright 2016 American Chemical Society.

modification. Factors such as lattice mismatch and bond dissociation energy direct metal-on-metal deposition outcomes and have been classified into three categories, depending on the final morphology of the deposited metal: island, layered, and layer + island.[105,106] For island growth modes, a portion of the underlying substrate remains exposed after metal deposition (provided there is no postsynthetic fusion or ripening processes). This growth mode, also called Volmer−Weber (VW) growth, leads to islands of the depositing metal, even at surface coverages equivalent to greater than one monolayer, and is typically attributed to the incoming metal having more favorable enthalpic interactions with itself than with the substrate. Layered growth, also referred to as Frank−van der Merwe (FM) deposition, proceeds by the successive formation of continuous monolayers of the depositing metal.[107] Here, a complete monolayer of the secondary metal is deposited prior to the formation of additional atomic layers. A combination of layer + island growth may also be observed and is called Stranski−Krastanov (SK) growth. In SK growth, layered growth

https://doi.org/10.1021/acs.chemrev.3c00033
Chem. Rev. 2023, 123, 3493−3542

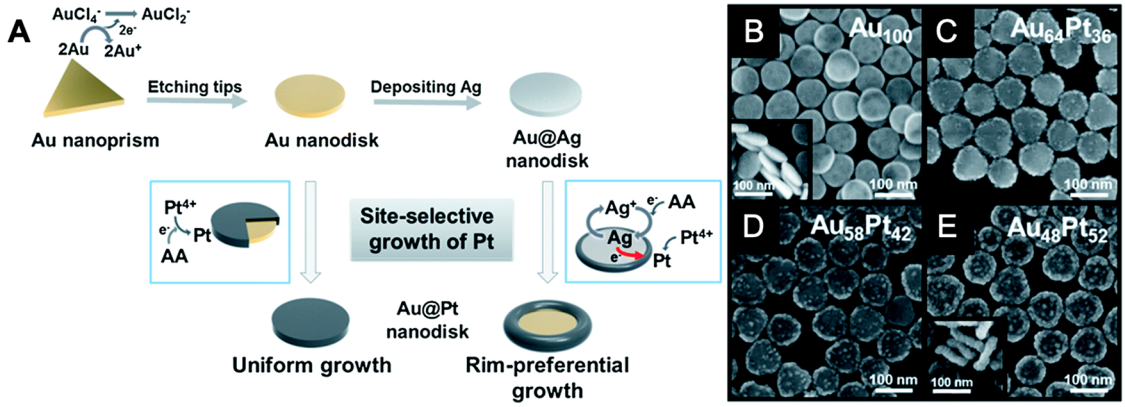

Figure 8. (A) Synthetic scheme for Au@Pt nanodisks. (B–E) SEM images of Au nanodisks (B), rim-preferentially Pt-coated Au nanodisks (Au@Pt(rim) nanodisks) (C–E) with increasing the concentration of Pt precursors. Atomic percent of Au and Pt is indicated at the upper right side of each image, which was obtained from EDS analysis. The insets in B and E show side views. Adapted with permission from ref 117. Copyright 2014 The Royal Society of Chemistry.

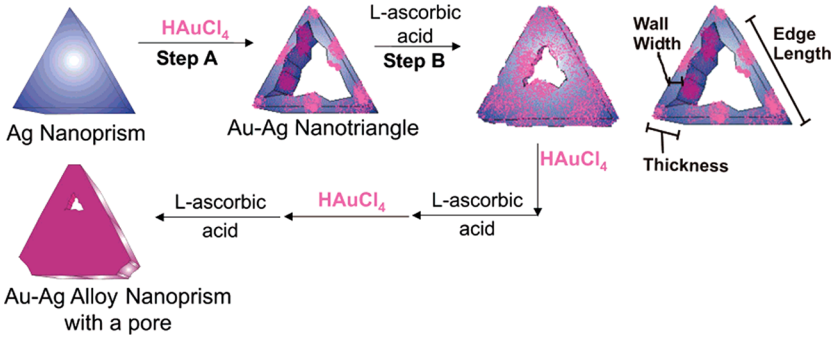

Figure 9. Scheme of Au–Ag alloy triangular nanoframe synthesis. Reproduced with permission from ref 118. Copyright 2003 American Chemical Society.

transitions into an island growth pathway after reaching a critical surface coverage threshold.[108]

2.6.2. Nanoislands on Nanoplates. Like in the case of thin films, island deposition on nanoplates may be driven by metal–metal interactions such as bond enthalpies, lattice mismatch, and redox interactions. However, in the case of nanoplates, the secondary metal deposition may also be guided by surface ligand modifications. For nanoisland formation on nanoplates, the most frequently studied metal combination has been Pt deposition on Au, where Pt is known to deposit on Au substrates via VW growth modes due to the enthalpic driving forces of Pt–Pt bond formation vs Pt–Au, and this deposition motif has been observed on other Au nanoparticle substrates as well.[109]

Synthesis of nanoisland morphologies on nanoplates adapt the same seed-mediated approach used for the preparation of metal nanoplates, where the underlying metal nanoplate is synthesized separately and then introduced to a new chemical environment that facilitates the growth of island deposits. Studies have shown that reaction kinetics are important in determining the driving forces that dominate the observed deposition morphologies.[110] In the case of Pt islands on Au, using ^{195}Pt-NMR studies of Pt(IV) speciation in water, the populations of various Pt(IV) complexes could be identified, and showed that Pt(IV) precursor species that were more aggressive oxidants led to competitive GRRs in solution, ultimately creating heterogeneous Pt–Au alloyed triangular frames. However, when speciation of Pt(IV) produced a less aggressive oxidant, the surface chemistry of the underlying Au platelet, combined with Pt–Pt and Pt–Au bond enthalpies, explained Pt deposition patterns that arose in regular arrays of Pt islands (Figure 7). A tilt series of high-angle annular dark field scanning transmission electron microscopy (HAADF-STEM) images were used to study the 3D structure of Pt islands via tomographic reconstruction (Figure 7).[111] Similar to Pt deposition on films of Au(100) and Au(111),[112] the Pt islands were found to exhibit irregular "tree-like" morphologies, where islands branch outward as they grow longer, consistent with a dendritic growth pathway often observed for larger Pt nanoparticles.[113]

When considering the driving forces that determine the arrangement and size of nanoislands, as well as their development vs other redox-mediated seed modifications, it may be difficult to decouple the influence of surface crystallinity and surface chemistry for a specific pathway of metal deposition. In 2010, Han and co-workers investigated the impact of substrate crystallinity on the observed mode of island deposition.[114] Here, Au nanoparticles bound by low index facets (e.g., Au(100), Au(110), and Au(111)) were used as substrates for Pt island deposition. Epitaxial deposition of Pt islands was observed on all facets, suggesting no crystallographic preference for Pt island nucleation and growth. However, when there is a large difference in crystal facet reactivity, due to either the surface energy or facet–ligand interactions, facet-selective island deposition is observed. For example, Millstone et al. have shown the ability to site selectively deposit Pt and Pd metals onto Au nanoplates using surface ligands to selectively block growth on well-passivated sites.[110,111,115]

https://doi.org/10.1021/acs.chemrev.3c00033
Chem. Rev. 2023, 123, 3493–3542

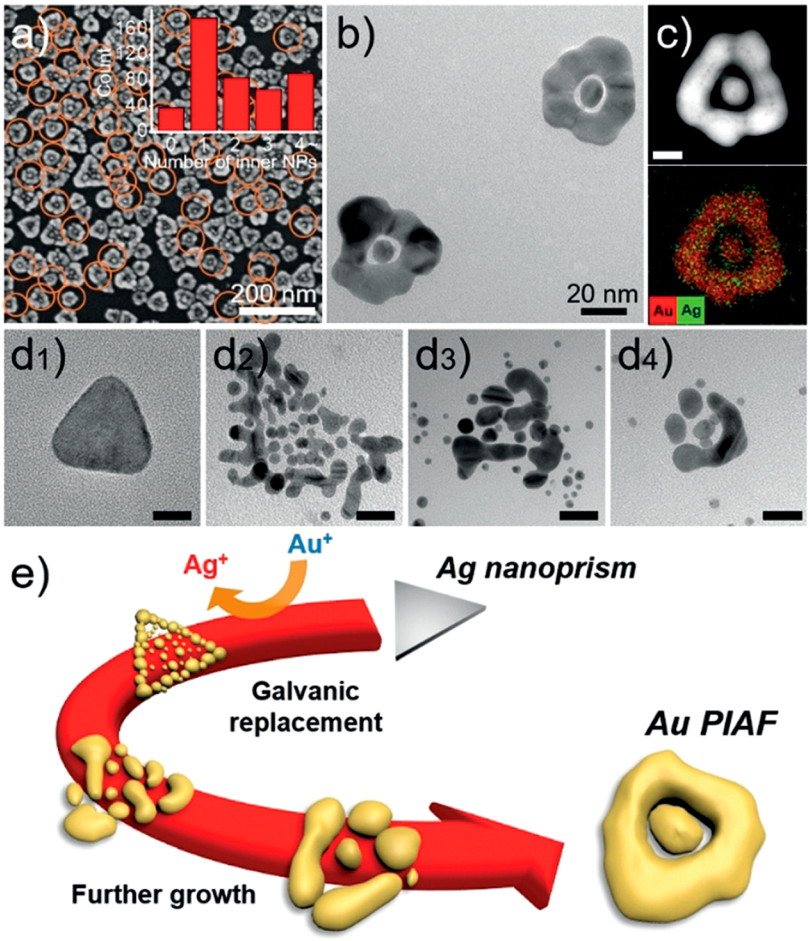

Figure 10. (a) SEM image of particles-in-a-frame nanostructures (PIAFs). Au PIAFs containing one inner nanoparticle are marked by orange circles. (b) TEM image of Au PIAFs containing one inner nanoparticle. (c) HAADF-STEM image and corresponding EDX elemental mapping image of an Au PIAF (scale bar: 10 nm). (d) Representative TEM images of nanostructures in the samples collected at different reaction times during the formation of Au PIAFs: (d1) 0, (d2) 5, (d3) 60, (d4) 300 s. Scale bars: 20 nm. (e) Illustration of hypothesized growth pathway of Au PIAFs. Adapted with permission from ref 120. Copyright 2019 Wiley-VCH.

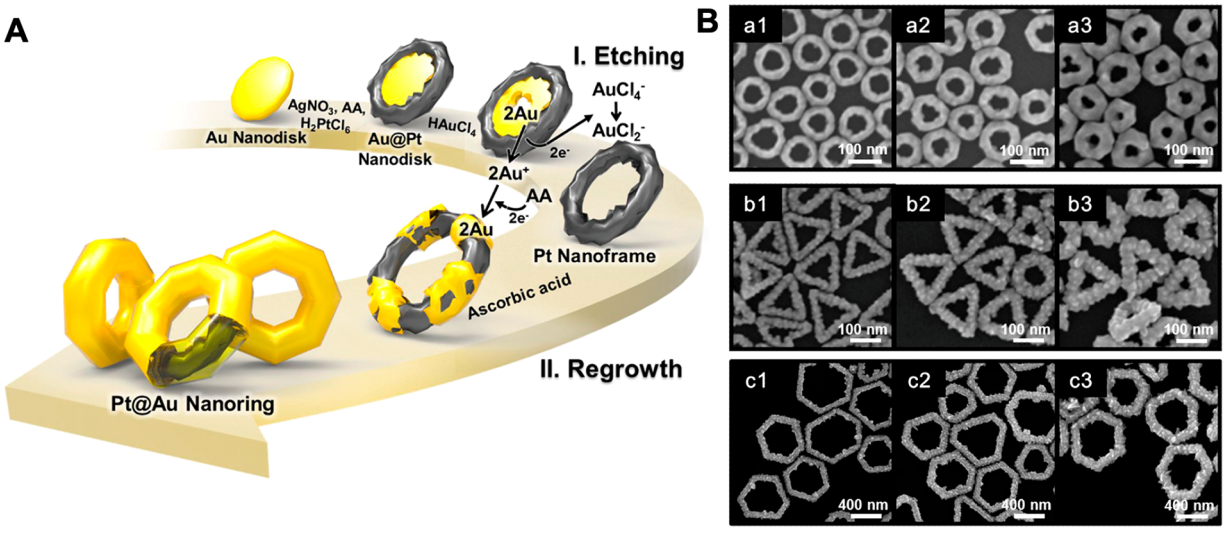

Figure 11. (A) Schematic illustration of the experimental procedures for synthesizing Pt@Au nanorings. (B) SEM images of Pt@Au circular nanorings (a1−a3), Pt@Au triangular nanorings (b1−b3), and Pt@Au hexagonal nanorings (c1−c3), having different thickness. Adapted with permission from ref 123. Copyright 2014 American Chemical Society.

Redox processes such as UPD and GRRs can also strongly influence the mode of island/secondary metal deposition on nanoparticle substrates, leading to hybrid and ultimately frame-like structures. For example, Park and co-workers synthesized

https://doi.org/10.1021/acs.chemrev.3c00033
Chem. Rev. 2023, 123, 3493−3542

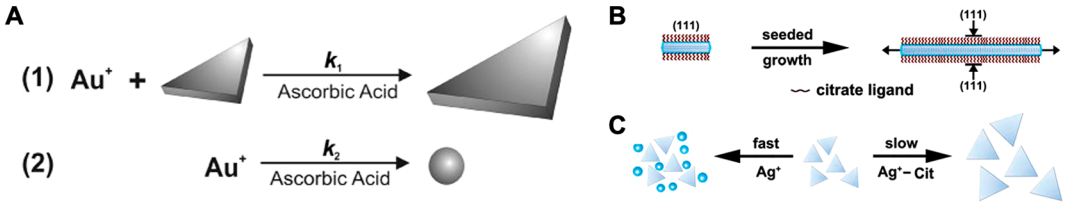

Figure 12. (A) eqs 1 and 2 represent the competing reactions during the particle growth process. When given amounts of Au ions and reducing agent are added stepwise, $k_2 < k_1$. However, when the same amount is added "all-in-one", $k_2 > k_1$. Adapted from ref 125. Copyright 2006 Wiley-VCH. (B) Schematic Illustration of the anisotropic seeded growth of Ag nanoplates based on selective ligand adhesion. (C) Schematic Illustration of the consequences of seeded growth at different reaction rates. Adapted from ref 28. Copyright 2010 American Chemical Society.

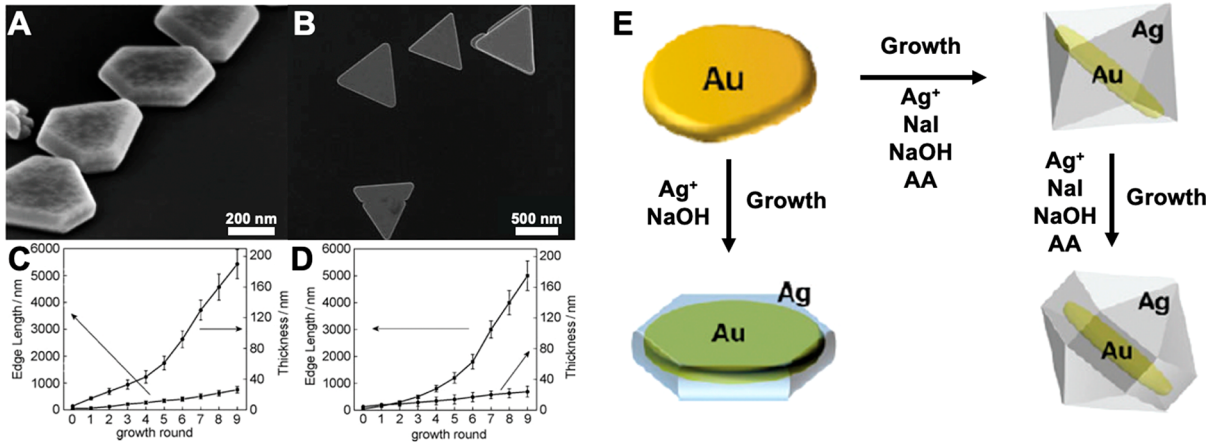

Figure 13. SEM images of Ag nanoplates synthesized in the presence of (A) trisodium citrate and (B) poly(vinylpyrrolidone) (PVP) as capping agents, respectively. (C,D) Plots of both edge length and thickness of the Ag nanoplates as a function of the number of growth rounds for (C) trisodium citrate and (D) PVP capping ligands. Adapted from ref 129. Copyright 2011 Wiley-VCH. (E) Scheme of core@shell Au@Ag nanostructure formation with and without added iodide. Adapted from ref 130. Copyright 2011 American Chemical Society.

Au@Pt nanoplates. Here, a Ag UPD layer was precoated on the surface of Au nanodisks and then Pt atoms were selectively grown on the periphery of Au nanodisks via a GRR between the Ag UPD layers and Pt (IV) species, leading to the formation of Au@Pt nanodisks (Figure 8).[116,117]

2.6.3. Nanoframes. In addition to producing island-like hybrid structures, processes such as GRR and UPD can build from nanoplate scaffolds to yield a wide array of both compositionally and architecturally complex nanostructures. One of the earliest demonstrations of these plate-to-frame transformations used Ag nanoplates as a starting template. Here, Au/Ag triangular and circular nanoframes were obtained via GRR between Ag nanoplates and Au(III) precursors.[118,119] Au(III) reacted with (111) facets of the Ag nanoplates, and led to the formation of central voids while retaining the triangular shape (Figure 9).

Over the past two decades, GRRs have been used to synthesize progressively more complex systems via further refinement of reaction conditions. For example, Han and co-workers synthesized particle-in-a-frame (PIAF) nanostructures by conducting the reaction at low temperature (0 °C). The lower temperature allowed site-selective GRR on the edge regions of Ag nanoplates (due to higher surface energy of the nanoplate edges relative to their terrace regions). This process first creates isolated Au deposits which then grow and ultimately fuse over the course of the reaction yielding Au PIAF nanostructures (Figure 10).[120]

In addition, multistep chemical reactions including successive and selective deposition and etching steps have been shown to create framed structures from nanoplate starting materials.[121,122] For example, Park and co-workers have developed a versatile synthetic approach that includes successive redox-mediated reactions such as metal deposition of Pt via GRR between Ag UPD layers and Pt(IV) ions, and selective etching of the Au domain via the comproportionation reaction of Au ions. Thus, Au nanodisks could be transformed into PtAu nanorings with various shapes (e.g., circular, triangular and hexagonal shapes) could be synthesized by applying this synthetic strategy to other shapes of Au nanoplates (Figure 11).[123]

2.6.4. Epitaxial Growth. Epitaxial growth of secondary metals on metal nanoplates has also produced a wide range of nanoplate-based heterostructures. In nanoisland deposition, VW growth modes dominate. In the following examples, secondary metal deposition proceeds either by FM or SK growth modes and produces additive rather than hollow nanostructures, with fundamental symmetries imposed by the original plate-like particle shapes. For epitaxial growth of secondary metals on preformed nanoparticles, a commonly quoted rule of thumb is that a lattice mismatch between seeds and secondary metals must be smaller than ~5%.[124]

Epitaxial secondary metal growth has been shown for both homogeneous and heterogeneous metal combinations. In the homogeneous case, the same metal as the starting platelet is added to the nanoplate solution and used to control nanoplate edge length, thickness, or shape. In one example, Mirkin and co-workers investigated the mechanism of selective growth of Au on the edge regions of Au nanoplates with respect to surface crystallinity and suggested a synthetic strategy for controlling the lateral size of Au nanoplates via multistep overgrowth of Au (Figure 12A).[125] Yin and co-workers investigated how the

https://doi.org/10.1021/acs.chemrev.3c00033
Chem. Rev. 2023, 123, 3493−3542

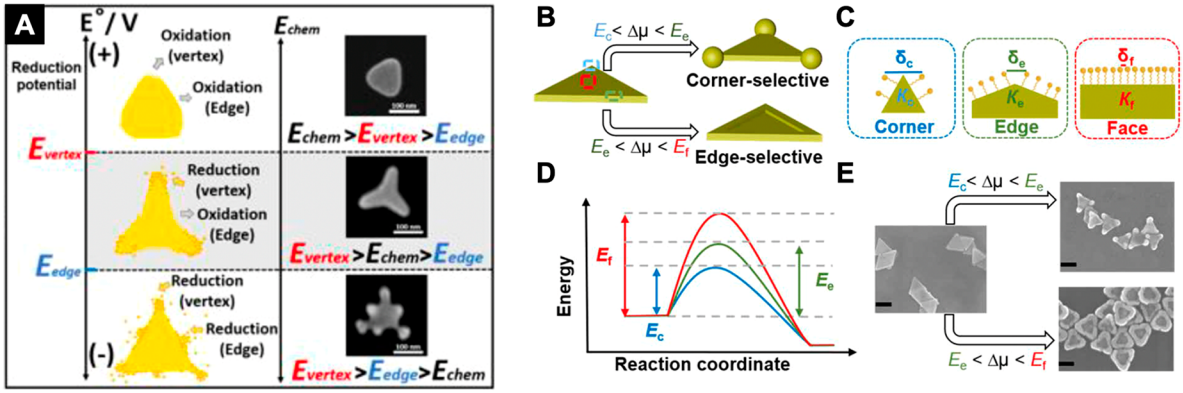

Figure 14. (A) Reduction potential diagram of the shape transformation reaction. Adapted from ref 131. Copyright 2021 American Chemical Society. (B) The $\Delta\mu$ for NC growth can be tuned to favor corner- and edge-selective growth. $\Delta\mu$ is defined as the difference between chemical potential of the solute in solution (e.g., Au^0 atoms) and that of the solid crystal (e.g., Au seed). (C) Pictures depicting different regions [corners (c), edges (e), and faces (f)] of a Au nanoplate with varying curvatures and, therefore, different ligand distributions. The higher the curvature (K), the larger the average distance between the ligands (δ) (here, $K_c > K_e > K_f$ such that $\delta_c > \delta_e > \delta_f$). (D) Schematic showing the general energy profile for nanocrystal growth, which is dictated by the degree of particle curvature $E_c < E_e < E_f$. (E) SEM images showing corner- and edge-selective nucleation on Au nanoplates. Scale bars: 100 nm. Adapted from ref 132. Copyright 2021 AAAS under CC BY 4.0 http://creativecommons.org/licenses/by/4.0/.

reduction rate of Ag and the presence of citrate ions as a facet-blocking agent impact the lateral size of resulting Ag nanoplates (Figure 12B,C).[28] A similar effect was reported by Kuttner et al.[126]

Shape and thickness of nanoplates can also be controlled through epitaxial growth of secondary metals on nanoplates. In one example, Park and co-workers controlled the shape of nanoplates from circular to hexagonal via deposition of Au in the presence of cetyltrimethylammonium bromide (CTAB) and I^- (which can preferentially block Au (111) facets).[127] Wang and co-workers modulated the thickness of Au hexagonal nanoplates by controlling the amount of Au added onto the Au nanodisks and the concentration of CTAB in the absence of iodide ions.[128]

Like halide ions in the previous examples, different ligand types have been used to modulate epitaxial growth. For example, the growth mode of Ag on Ag nanoplates (e.g., edge- vs face-favored growth) could be modulated by considering different affinities of polyvinylpyrrolidone (PVP) and citrate ions toward (111) and (100) facets of Ag nanoplates, respectively.[129] Iodide ions again play a crucial role in the growth of Ag on Au nanodisks. In the presence of iodide ions, Ag atoms could be deposited on both the top and bottom faces of Au nanodisks because iodide ions tend to preferentially adsorb on Au (111) facets and Ag ions readily react with iodide ions due to their high affinity for AgI ($K_{sp}(AgI) = 8.3 \times 10^{-17}$), and these processes ultimately lead to 3D Au@Ag dodecahedra. On the other hand, in the absence of iodide ions, Ag atoms were uniformly deposited on the entire surface of Au nanodisks resulting in Au@Ag core−shell nanoplates (Figure 13).[130]

Interestingly, ligands have even been used to elicit chiral growth on Au nanoplates. In work by Ma et al., chiral ligands such as L-cysteine and L-glutathione were postsynthetically added to cetyltrimethylammonium chloride (CTAC)-coated Au nanoplates in the presence of ascorbic acid and $HAuCl_4$, to yield propeller like structures with well-defined chiral geometries, as evidenced by circular dichroism analysis. Moreover, the degree of chirality could be tuned via the proportion of chiral ligands added during synthesis.

Finally, it should be noted that all of the above-discussed processes: island growth, redox-mediated frame formation, and epitaxial growth, can be observed within a single system with only subtle changes in reaction conditions. For example, morphology evolution from Au nanoplates into Au tripods was observed by exploiting the different redox potentials of triangular nanoplate edges and tips.[131] Corner- and edge-selective growth modes of Au on Au nanoplates could be controlled by considering the chemical potential of Au atoms in solution and the accessibility of solutes to different sites (e.g., edge, corner, or face) (Figure 14).[132]

3. OTHER CRYSTAL LATTICES AND COMPOSITIONS

Apart from Au or Ag, nanoplates have also been made of various other metals, with the motivation of achieving different properties, as will be discussed below. We review in this section the mechanistic aspects discussed in the literature for the growth of different metal nanoplates, highlighting similarities and differences with the more familiar cases described before. As a general rule, metals of the same group present similar crystallographic structures, as an atom's electronic structure plays a determinant role in its packing. However, there are important exceptions, as can be appreciated in the periodic table reported in Figure 15. The elements of the periodic table can be grouped by their most stable crystallographic habit at standard temperature and pressure. The most represented crystal families are face-centered cubic (*fcc*, 29 elements), hexagonal close-packed (*hcp*, 28 elements), and body-centered cubic (*bcc*, 23 elements), grouping two-thirds of the known elements. The last third forms crystal structures with a lower degree of symmetry, which are recently attracting the interest of the community.[133] We decided to exclude from the discussion the family of metallenes, as the mechanistic aspects for the preparation of this class of materials have been rarely discussed, usually paying more attention to their applications in catalysis, energy conversion and storage, and batteries.[134−142] The different synthetic protocols for the synthesis of plate-like nanocolloids made of various metals are summarized in Table 2 below.

3.1. *fcc* Metals

Apart from the coinage triad (Au, Ag, and Cu), this crystallographic group contains important catalytic elements of the 9th (Rh, and Ir) and 10th (Ni, Pd, and Pt) groups, some interesting earth-abundant elements such as Al, Ca, and Sr, as well as heavy elements like Pb (Figure 15). Due to their high

https://doi.org/10.1021/acs.chemrev.3c00033
Chem. Rev. 2023, 123, 3493−3542

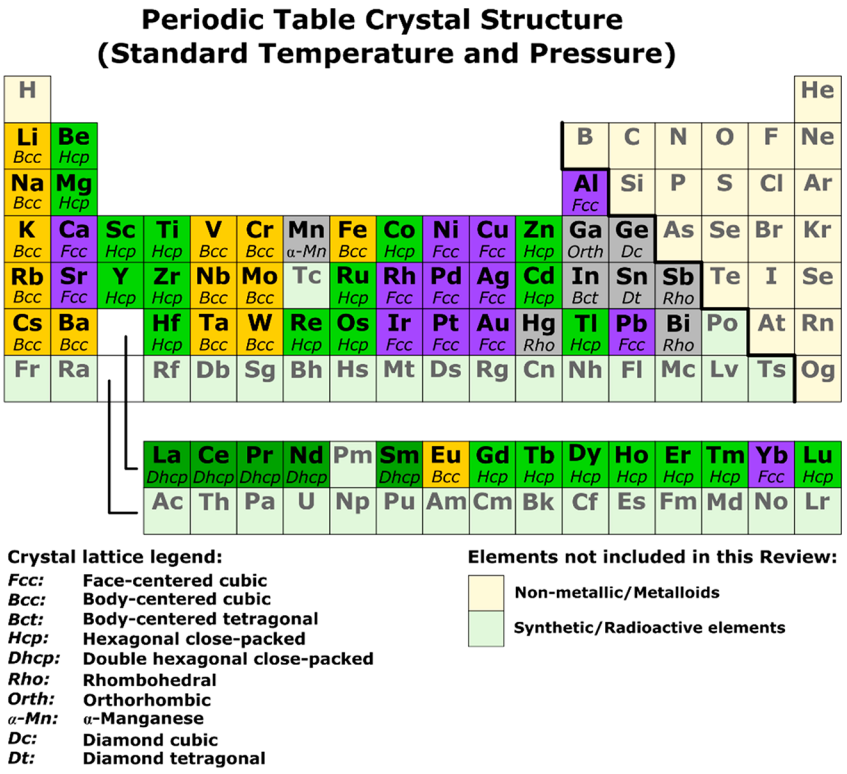

Figure 15. Periodic table indicating the most stable crystal structure at standard temperature and pressure for each element; nonmetal and synthetic/radioactive elements are not included in this review.

reactivity in their metallic state, there are no reports on metallic Ca and Sr nanoparticles. From a mechanistic standpoint, the growth of nanocrystals made of other *fcc* metals is expected to show many similarities with the well-known cases of Au and Ag. Consequently, platelets and truncated bipyramids should both present extended {111} facets, and their preparation would require the formation of stacking faults and single twin defects, respectively (see section 2).[34,35]

3.1.1. Copper. Cu has been considered the minor player of the coinage triad, due to its tendency to oxidize rapidly in the presence of oxygen and its lower plasmonic efficiency in the visible part of the electromagnetic spectrum.[143,144] For these reasons, the colloidal chemistry of Cu is often focused on the use of Cu oxides and sulfides for the preparation of semiconductor nanoparticles.[145] Cu sulfide can also serve as the starting material for cation-exchange processes in postsynthetic modification of colloids, exploiting solvation energies and Lewis acid−base interactions.[146] More recently, Cu metallic nanoparticles received a renewed interest as earth-abundant element for sustainable plasmon-driven catalysis,[147] as well as high quality plasmonic nanoparticles in the mid-infrared.[148−150] The synthesis of 2D metal Cu colloids was first reported by Pileni's group, using an excess of hydrazine to reduce Cu bis(2-ethylhexyl)sulfosuccinate in a reverse micellar system.[151,152] The prepared nanodisks presented an average diameter of 27 nm, and high resolution (HR) TEM and X-ray diffraction (XRD) analysis confirmed they were *fcc* crystals with extended parallel {111} facets, developed through the formation of stacking fault defects. The use of PVP and hydrazine in dimethylformamide (DMF) was proposed by Pastoriza-Santos et al. a few years later, successfully improving the overall shape yield (>95%) and increasing the aspect ratio of the synthesized platelets, which present an edge length of 50 nm and a thickness of 20 nm.[153] This geometrical modification results in a red-shift of the colloids' localized surface plasmon resonance (LSPR) away from Cu interband transitions, thereby reducing damping and enabling the formation of an intense and sharp extinction peak around 600 nm. Moreover, the use of DMF as solvent and PVP as stabilizing agent enabled the authors to perform the whole synthesis under ambient atmosphere without significant oxidation. The same polymer was used in other synthetic setups to increase the aspect ratio of Cu platelets even further (200 nm edge length, only 8 nm in thickness), improving their catalytic performance and their stability under the reaction conditions. For example, Sun et al. exploited potassium sodium tartrate to lower the reduction rate of the Cu precursor and kinetically induce the formation of large platelets.[154] Cu nanoplates were also synthesized in hydrothermal approaches using milder reducing agents and basic pH.[155−160] These methodologies yield Cu nanoplates with extremely high aspect ratios (up to 30 μm in edge length for a thickness of ∼100 nm);[159] however, this comes at the expense of overall quality and size dispersity in the colloid. Two recent publications demonstrate the possibility of synthesizing Cu 2D nanoparticles under similar conditions as those used for the other coinage metals. Luc et al. used Cu nitrate, ascorbic acid, and CTAB for the preparation of triangular Cu nanosheets showing high performance for the electrochemical production of acetate from carbon monoxide.[161] In 2022, Wu et al. proposed to establish a balance between oxidative oxygen gas and reductive glucose to control the formation of Cu nanodisks. The reaction takes up to 3 days to complete, offering a better control over size dispersity and shape-yield (an average of 80 nm in edge length and 7 nm in thickness, Figure 16A,B).[162] The obtained Cu nanodisks show promising catalytic activity for the electrochemical reduction of

https://doi.org/10.1021/acs.chemrev.3c00033
Chem. Rev. 2023, 123, 3493−3542

Table 2. Summary of the Synthetic Protocols for the Preparation of Plate-Like Nanocolloids Made of Different Metals, As Discussed in Section 3

element	crystal structure	target morphology	edge length	thickness	growth conditions	related refs
Cu	*fcc*	nanoplatelets	50	20	PVP/hydrazine/DMF	153
Cu	*fcc*	nanodisks	80	7	O_2 gas/glucose	162
Pd	*fcc*	hexgonal nanopltelets	30−60	20	PVP/formaldehyde; solvothermal	173
Pd	*fcc*	ultrathin nanosheets	6−60	1	$W(CO)_6$/citric acid/CTAB	182
Pd	*fcc*	nanodisks/nanorings	30	1.6	I-/O_2 gas	184
Pt	*fcc*	planar tripods	140	8	1,2-hexadecanediol/adamantanecarboxylic acid/hexadecylamine	209
Pt	*fcc*	planar pentapods	30−120	20	oleylamine/H_2 gas	212
Pt	*fcc*	tribranched nanoribbons	500	5	ammonium fluoride/H_2 gas	213
Ni	*fcc*	nanotriangles	<5	NA	tetra-*n*-octylammonium glycolate/H_2 gas	236
Ni	*fcc*	nanotriangles	15 (2)	6	oleic acid/oleylamine; thermal decomposition	239
Ni	*fcc*	nanoplatelets	15−70	6	$W(CO)_6$; hydrothermal	226
Rh	*fcc*	nanotriangles	9−11	NA	$RhCl_3$/triethylene glycol	256
Rh	*fcc*	ultrathin nanosheets	18	2−4	$Rh(ac)_3$/glucose/oleylamine	258
Rh	*fcc*	nanoplatelets	120−1300	0.9 (0.4)	PVP/CO	259
Rh	*fcc*	ultrathin nanosheets	500	<0.4	$Rh(acac)_3$/benzyl alcohol/formaldehyde/PVP; solvothermal	262
Al	*fcc*	nanosheets	NA	1.5	O_2 gas/N_2 gas/$LiAlH_4$	89
Ir	*fcc*	nanoflkes	800−1000	NA	CTAB/1,2-dihydroxynaphthalene/UV irradiation	289
Pb	*fcc*	nanoplatelets	50−100	NA	PVP/CTAB	298
Mg	*hcp*	nanoplatelets	100−500		Li naphthalide	330
Mg	*hcp*	nanoplatelets	100−300	30−60	Li naphthalide	331
Co	*hcp*	nanodisks	35	4	oleic acid/trioctylphosphine oxide; thermal decomposition	339
Co	*hcp*	nanoplatelets	150−220	10	NaH_2PO_2; hydrothermal	341
Zn	*hcp*	hexagonal nanoplatelets	30−200	NA	oleylamide/octadecene/$LiN(SiMe_3)_2$; thermal decomposition	348
Ru	*hcp*	irregular nanotriangles	24	4	formaldehyde; hydrothermal	354
Ru	*hcp*	flat capped-columns	∼60	NA	sodium oxalate/formaldehyde; hydrothermal	354
Ru	*hcp*	ultrathin nanoplatelets	NA	1−1.2	2-propanol/urea; solvothermal	358
Ru	*hcp*	3-fold nanostars	10	0.8	hexadecylmine/lauric acid/H_2 gas	359
Li	*bcc*	ultrathin hexagonal nanoplatelets	∼500	<10	electrochemical growth inside a TEM	369
Fe	*bcc*	nanoplates	300−1000	20−30	$NaBH_4$; external magnetic field	371
In	*bct*	nanotriangles	>1000	NA	$LiBH_4$/*N*-*N*-diethylaniline	384
In	*bct*	nanotriangles	60 (8)	NA	PVP/ethylene glycol/N_2 gas	385
Bi	*rho*	hexgonal nanoplatelets	50−100	NA	$Bi[N(SiMe_3)_2]_3$	398
Bi	*rho*	hexagonal nanodisks	100−260	17	1-dodecanethiol; solvent-free thermolysis	399
Bi	*rho*	nanotriangles	50	NA	ascorbic acid/Na_2EDTA/PVP; hydrothermal	402

nitrate to ammonia, a zero CO_2 emission process alternative to the standard Haber-Bosch process.[163−166]

3.1.2. Palladium. Pd is a key component for several catalytic processes, including CO_2 reduction,[167] hydrogen production (and storage),[168] as well as important carbon−carbon coupling reactions.[169] The activity and efficiency of these catalysts varies greatly, depending on the specific crystallographic facet that is involved in the reaction, and would therefore greatly benefit from the possibility to rationally design Pd surfaces. Control over the growth and geometry of Pd nanocrystals was first attempted by Xia and co-workers in the early 2000s, using a solvothermal/polyol method. In this approach, PVP was used as both capping and reducing agent. Despite the presence of extended low-energy {111} facets, the overall surface energy of nanoplates is higher compared to isotropic nanoparticles due to the presence of parallel stacking faults and high curvature areas at the tips, which are composed of partially uncoordinated metal atoms.[35] Consequently, a key aspect to favor nanoplate growth was identified in the use of kinetically controlled processes, deviating from thermodynamic control and inducing the formation of seeds with stacking faults that could grow into the nanoplate shape.[170] This was achieved by reducing the deposition rate of the metal precursor,[171] varying PVP molecular weight,[172] reaction temperature and pH, as well as through the use of oxidative etching to ensure a tighter control over the growth rate,[68,171] and mild reducing agents such as hydroxylamine.[80]

Trinh et al. were able to significantly improve the outcome of the solvothermal/PVP approach by adding formaldehyde to the growth mixture.[173] Formaldehyde was proposed to adsorb selectively onto Pd {111} facets, thereby suppressing the elimination of {111} side surfaces,[174] slow down the growth kinetics (improving control over size dispersity), and resulting in the preferential formation of Pd hexagonal nanoplates over triangular ones (Figure 16C). The higher level of control over the formation of nanoplates enabled the extensive characterization of their catalytic effect on Suzuki coupling reactions.[173] Despite these improvements, the resulting colloids still present a rather high size polydispersity (∼30%). Moreover, the presence of high concentrations of PVP, which can drastically passivate the surface, represents a major drawback for the use of the synthesized colloids as heterogeneous catalysts. These observa-

https://doi.org/10.1021/acs.chemrev.3c00033
Chem. Rev. 2023, 123, 3493−3542

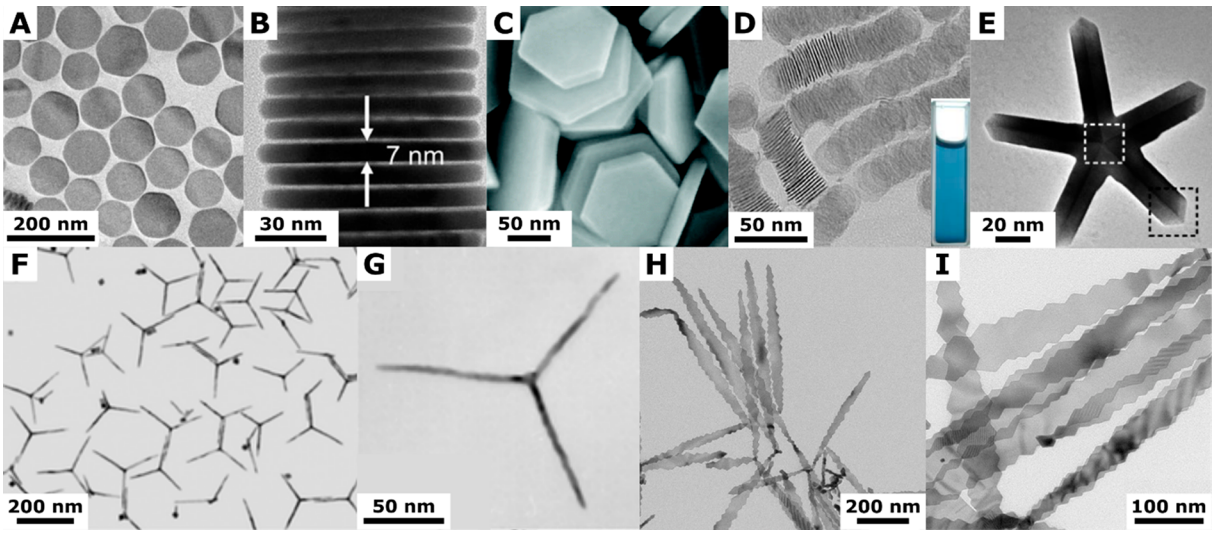

Figure 16. *fcc* nanoplates, part 1: (A,B) Cu nanodisks prepared in ultrapure water balancing oxidative O_2 gas and reductive glucose. Adapted with permission from ref 162. Copyright 2022 American Chemical Society. (C) Pd nanoplates synthesized via a solvothermal/PVP approach. Adapted with permission from ref 173. Copyright 2015 Royal Society of Chemistry. (D) Pd nanodisks prepared in aqueous environment controlling oxidative etching from I^-/O_2 pairs. Adapted with permission from ref 184. Copyright 2017 Royal Society of Chemistry). (E) Pt pentatwinned planar nanostars obtained combining oleylamine and hydrogen gas as solvent/stabilizer and reducing agent, respectively. Adapted with permission from ref 212. Copyright 2012 Wiley-VCH). (F,G) Pt planar tripod synthesized using adamantanecarboxylic acid and hexadecylamine as a double capping agent system. Adapted with permission from ref 209. Copyright 2006 Royal Society of Chemistry). (H,I) Pt tribranched nanoribbons produced by the addition of ammonium fluoride to the reaction mixture. Adapted with permission from ref 213. Copyright 2009 American Chemical Society.

tions, together with the progress achieved in the understanding of the role of halides in the synthesis of Au and Ag nanoparticles, shifted the focus of the community toward the use of small molecule adsorbates.[32]

The role of halides has been investigated by various groups, who found them to play a similar role to the one described for Au and Ag: bromide stabilizes {100} facets,[34,175,176] whereas iodide induces the formation of penta-twinned structures such as nanowires, decahedra, and nanorods, probably through selective binding onto {111} facets.[177,178] However, the higher energy difference for the facets in Pd (and Pt) compared to coinage metals, prevents iodide from inducing the formation of platelets or triangular structures.[179] Interestingly, the quest for stronger and more selective surface-blocking agents was supported by the vast scientific literature dedicated to the catalytic activity of Pd.[180] In this direction, N. Zheng and co-workers successfully used carbon monoxide (CO, known poisonous species for Pd-based catalysts)[181] to selectively promote the growth of structures with extended {111} planes, leading to the formation of ultrathin (1.8 nm thick) nanosheets.[88] In 2013, the same group was able to completely eliminate the use of PVP as a capping agent by implementing a carbonyl Pd complex ($[Pd_2(\mu\text{-}CO)_2Cl_4]^{2-}$) as the metal precursor in aqueous media, in the presence of CO.[181]

Li et al. were able to improve on this synthesis and gain control over the edge dimension of the nanosheets within a wider size range, from 6 to 60 nm, with standard deviation <20%.[182] These results were achieved using tungsten hexacarbonyl ($W(CO)_6$), citric acid, and CTAB. The role of $W(CO)_6$ is 2-fold: on one side it enables a tighter control over the concentration of CO, while on the other it introduces high-oxidation state tungsten species that can promote the formation of Pd nuclei. Citric acid helps the degradation of $W(CO)_6$, while regulating the extent of nucleation at the first stages of the growth; moreover, citrate was shown to selectively bind on {111} facets, further promoting the stabilization of the platelet shape.[34,183] By including oxidative etching from I^-/O_2 pairs, Huan et al. recently demonstrated the synthesis and self-assembly of ultrathin nanodisks and nanorings with an impressively narrow size dispersion (Figure 16D).[184]

Interestingly, even though seeded-growth protocols have been explored, they normally involve the use of already "shape-developed" seeds. In other words, despite some efforts in controlling the crystallography of the nucleated seeds, there has not been a consistent effort in the production of stable, rationally designed Pd seeds. This aspect certainly holds interesting potential to improve the yield and size dispersity of the prepared Pd colloids. It is worth mentioning that the exploration of Pd nanoparticle synthesis has also led to the preparation of exotic 2D shapes that have not been reported for Au. In a first example, Yin et al. demonstrated how, by taking advantage of the rich complexation chemistry of the d^8 group to modulate the redox potential of the Pd precursor, it is possible to induce twinning in the [211] direction, leading to Pd hexagonal nanosheets presenting a thicker frame around their edges.[185] In an opposite direction, Li et al. exploited the combination of overgrowth and oxidative etching mediated by the presence of bromide and oxygen, to induce the transformation of ultrathin Pd hexagonal nanosheets into nanorings with remarkable catalytic performance.[186] In a third example, Yin et al. reported the synthesis of Hanoi Tower-like nanostructures composed of multilayered 2D nanosheets. The synthesis of this interesting geometry was obtained by exploiting the competitive adsorption of CO and $Pd_4(CO)_4(OAc)_4$ on Pd low-index facets. Finally, propeller-like Pd nanostructures have been prepared by favoring oxidative etching conditions during the formation of ultrathin 2D nanosheets.[187,188]

3.1.3. Platinum. Similar to Pd, crystallographic control over Pt nanoparticle synthesis has radical implications toward their application as catalysts for several organic reactions, including hydrogenation and dehydrogenation, artificial photosynthesis, and fuel-cell reactions.[149,189−192] The synthesis of Pt nano-

https://doi.org/10.1021/acs.chemrev.3c00033
Chem. Rev. 2023, 123, 3493−3542

particles typically involves the reduction of Pt(II) or Pt(IV) precursors, which can take place both in aqueous and organic media, and can be performed using different reducing agents.[193−195] The exploration of shape control in Pt nanoparticle synthesis began in the late 1990s, together with the other *fcc* metals. Early work by El-Sayed and co-workers involving the use of hydrogen gas as reducing agent immediately identified reduction kinetics as a key aspect in controlling the final crystallography of the product.[196,197] Several years later, Xia and co-workers identified a similar trend in polyol-PVP solvothermal syntheses.[198] In one example, they took advantage of the slower reduction rate of nitroplatinate complexes, compared to chloroplatinate salts, to control the ratio of {111} and {110} facets, by adding sodium nitrate to the growth solution.[194] Moreover, the extension of thermolytic reduction to other high-boiling-point solvents (oleylamine, hexadecylamine, or oleyl alcohol) led to the preparation of branched structures including multipods and stars.[199] Finally, the use of halides as shape-directing agents was also explored in several studies for the preparation of cubic, octahedral, and flower-like Pt nanoparticles.[90,200−202] However, the controlled preparation of high quality Pt nanoplates remains elusive, with Pt epitaxial growth on preformed platelet structures and 2D template-confined growth as the only routes to access this type of structure.[203−206] The reason for this observation is likely found in the uniquely high internal strain energy associated with the formation of twin defects and stacking faults in Pt nanocrystals.[207,208]

Notwithstanding, twinned Pt crystals have been synthesized in the form of planar nanomultipods, where the formation of transient triangular monotwinned seeds was proposed as the first necessary stage of the growth mechanism.[209,210] The first report of this type of structure dates back to 2006, when Maksimuk et al. reported the synthesis of planar tripods using a combination of Pt acetylacetonate, 1,2-hexadecanediol (the reducing agent), adamantanecarboxylic acid and hexadecylamine (forming a double capping agent system), and diphenyl ether (the solvent). By reducing the temperature of the synthesis to around 160 °C, the formation of planar tripods was maximized above 25%, with the major byproducts consisting of monopods and bipods and only a small fraction of Pt nanocubes (Figure 16F,G).[209] The mechanism was proposed to involve the formation of crystal twinning in the {111} plane of Pt seeds (identified by the forbidden 1/3 {422} diffraction spot in the SAED pattern). This crystal defect leads to the formation of three re-entrant troughs along the same twin plane. Selective crystal growth along the three equivalent ⟨211⟩ directions induced the transformation of the troughs into ridges and then again into troughs. The alternation of these two features ultimately resulted in the formation of three coplanar branches in the $[2\bar{1}\bar{1}]$, $[\bar{1}2\bar{1}]$, and $[\bar{1}\bar{1}2]$ directions.[211] Interestingly, the aspect ratio of the prepared nanoparticles could be tuned between 7 and 20 by varying the reaction time.[209,211] The same growth mechanism was applied to penta-twinned structures by Lacroix et al., leading to the formation of 5-fold Pt nanostars using oleylamine and hydrogen gas as solvent/stabilizer and reducing agent, respectively. By carefully controlling the reduction rate, single and penta-twinned Pt seeds were stabilized and subsequently grown into branched structures (Figure 16E), with yields around 20%.[212]

In a recent communication, Gu and co-workers were able to combine ammonium fluoride and hydrogen gas to induce the formation of Pt tribranched nanoribbons (Figure 16H,I).[213] This seems to evolve from a similar Pt seed structure as for the planar tripod. However, the presence of both fluorine atoms and ammonium cations enables the formation of extended zig-zagged monocrystalline planar surfaces with 500 nm in length and a width of 40 nm. This morphology was prepared in a relatively high yield and certainly represents an important step toward the synthesis of thin planar Pt nanosurfaces, which hold high potential for several catalytic processes.

It is interesting to point out that the formation of planar multipods seems to be the preferential growth pattern for Pt crystals. This can be explained by looking at the reduction and growth driving forces for different noble metals, as suggested by Ravishankar and co-workers in their seminal work.[214−216] However, both shape yield and size polydispersity should be considerably improved to reach the state-of-the art quality of other metal colloids. Because all of these structures require the formation and stabilization of Pt twinned crystals, their preparation would significantly benefit from the controlled preparation of single-twinned, planar-twinned, or multiply twinned Pt seeds in high-yield. In this direction, Ruan et al. proposed the use of a specifically designed Pt binding peptide to induce the formation of monotwinned Pt seeds.[217,218] More recently, Chen et al. achieved similar results using a continuous flow reactor to control the nucleation step.[219] In both examples, the prepared monotwinned crystals were used for the high-yield preparation of Pt right bipyramids; however, under appropriate growth conditions, these could potentially lead to a more controlled preparation of Pt planar twinned structures such as nanotriangles.

3.1.4. Nickel. Ni nanoparticles display interesting catalytic and magnetic properties,[220−223] both as ferromagnetic and superparamagnetic nanocrystals.[224,225] Controlling Ni nanoparticle size and shape has important consequences on the material's magnetic anisotropy, coercivity, and blocking temperature.[226] When synthetizing Ni colloids, it is important to remember that Ni is not a noble metal. Consequently, reaction kinetics are generally harder to control, due to the need of a strong reducing agent to reach the Ni metallic state. Moreover, the formation of oxide species is another concern that needs to be addressed during synthesis, because it may have important consequences on the catalytic performance of the synthesized colloids.[227,228] For this reason, there are very few reports on aqueous syntheses of Ni particles. Nonetheless, the growth of highly homogeneous nanospheres, nanocubes and nanorods has been reported by means of thermal decomposition of organometallic precursors, as well as hydrothermal and polyol syntheses.[229−233] Interestingly, Ni nanoparticles can adopt both *fcc* and *hcp* crystal structures, depending on the synthetic conditions.[234,235] Despite this possibility, Ni nanoplates have only been reported as *fcc* crystals. The first report on triangular Ni nanoparticles dates back to the year 2000, when Bradley et al. reduced bis(cyclooctadiene)nickel (or $Ni(COD)_2$) in the presence of tetra-*n*-octylammonium glycolate, using hydrogen gas as reducing agent and THF as the solvent.[236] Electron microcopy showed the presence of both smaller spheres and nanotriangles, with a low yield of anisotropic structures, which made it impossible to characterize their magnetic properties.

In 2006, Leng et al. were able to control the formation of twins and thereby encourage the growth kinetics toward the formation of triangular and hexagonal nanoplates in high yield. Specifically, iron pentacarbonyl was used to induce Ni nanoparticle nucleation in a thermal decomposition setup, using Ni formate as precursor, 1-octadecene as solvent, and a combination of oleic acid and oleylamine as capping agents.[237,238] The edge length

https://doi.org/10.1021/acs.chemrev.3c00033
Chem. Rev. 2023, 123, 3493−3542

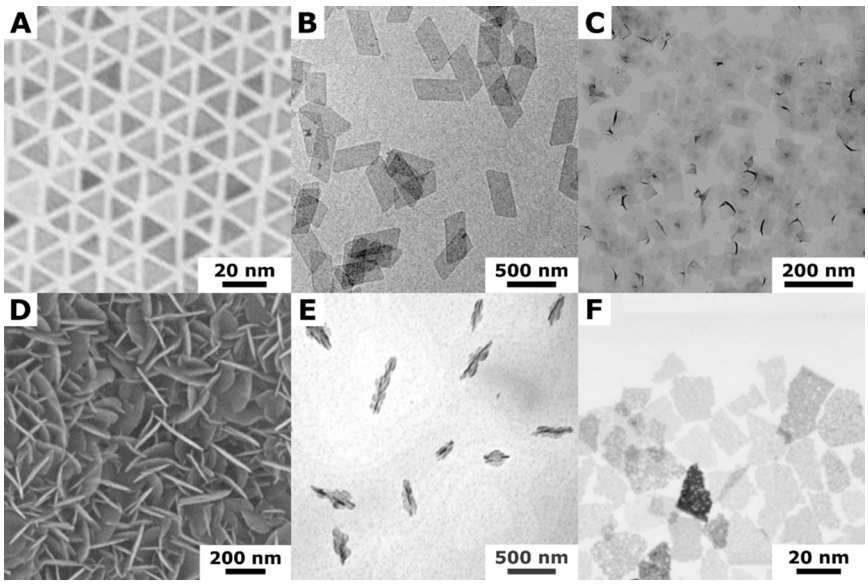

Figure 17. *fcc* nanoplates, part 2. (A) Ni nanotriangles synthesized in a mixture of oleic acid and oleylamine as capping agents and iron pentacarbonyl as shape-directing agent. Adapted with permission from ref 239. Copyright 2007 ACS. (B) Rh platelets prepared in *N*,*N*-dymethylformamide using PVP as capping agent and carbon monoxide as shape inducing agent. Adapted with permission from ref 259. Copyright 2015 Wiley-VCH under CC BY 4.0 http://creativecommons.org/licenses/by/4.0/). (C) Monoatomically thin Rh sheets obtained using formaldehyde and PVP as capping agent. Adapted with permission from ref 262. Copyright 2014 Springer. (D) Al platelets prepared exploiting a mixture of oxygen and nitrogen gas in the growth solution to regulate the concentration of oxygen during growth. Adapted with permission from ref 89. Copyright 2020 Cell Press. (E) Ir nanoflakes synthesized under UV light irradiation of a basic 1,2-dihydroxynaphthalene solution, in the presence of CTAB. Adapted with permission from ref 289. Copyright 2011 Elsevier. (F) Pb platelets prepared combining PVP and CTAB. Adapted with permission from ref 298. Copyright 2007 Wiley-VCH).

could be tuned, from 19 up to several hundreds of nanometers, by varying the nucleation density. In the same publications, Ni nanoplates showed improved and tunable magnetic properties compared to both bulk and isotropic colloids. The authors attributed the increased blocking coercive force to the magnetic shape anisotropy derived from the 2D structure.[237] Another important consequence of the magnetic anisotropy is the possibility to tune the magnetic properties of the particles by varying their alignment with respect to the applied external field.[224] Optical characterization confirmed the presence of a plasmon band in the UV−visible range.[238] In a follow-up study, the size polydispersity and shape yield were improved further, achieving Ni nanotriangles with an average edge length of 15 ± 2 nm and a thickness of 6 nm (Figure 17A). Interestingly, SAED analysis did not show any 1/3{422} diffraction spot, suggesting that the triangles were either single-crystals or monotwinned (with a twin parallel to the probing electron beam).[239] The first hydrothermal approach for the synthesis of Ni nanoplates was reported by Xu et al. in 2007.[229] In their synthesis, Ni chloride was used as the metal precursor, sodium dodecyl sulfate as surfactant, and sodium hypophosphite as reducing agent when operating in basic conditions. In order to push the reduction of Ni to its metallic state, an autoclave system was used to maintain a temperature of 110 °C for 14 h. Interestingly, the aqueous environment imposed a completely different growth mechanism, with the initial formation of Ni hydroxide nanoplates that were reduced into metallic Ni in a second stage of the hydrothermal process. Recently, Peng and co-workers successfully controlled the growth of Ni trigonal and hexagonal nanoplates, assisted by tungsten hexacarbonyl $W(CO)_6$.[226] The main advantage of this strategy is a reduced nucleation temperature (150 °C) and the possibility to perform the synthesis without the use of hydrogen gas. It should be noted that the mechanistic role of $W(CO)_6$ is different in the case of Ni, compared to analogous Pd and Pt syntheses, because W^{6+} cannot reduce Ni atoms into the metallic state. Interestingly, HRTEM and SAED indicate the presence of 1/3{422} forbidden diffraction spots, indicative of the presence of stacking faults for the highest aspect ratio particles, whereas triangular platelets seemed to be single crystalline. However, the presence of a single twin defect parallel to the {111} facets was not ruled out by either tilt SAED analysis or tomography reconstruction. Finally, it is worth mentioning the use of Ni in several alloy formulations. For example, NiCu nanoplates were reported in 2012, showing a similar growth mechanism and identical crystallography to both Ni and Cu nanoplates.[240] In another example, Ni@Ru and NiCo@Ru hexagonal nanosandwiches were obtained, with superior electrocatalytic activity for the oxygen evolution reaction.[241]

3.1.5. Rhodium. Rh is one of the rarest and most precious metals on Earth. It shows excellent catalytic activity for several important industrial processes, including hydrogenation, hydroformylation, hydrocarbonylation, and aryl halide coupling.[242−248] Commercially, it is one of the main components of catalytic converters.[249] Such a superior catalytic profile has been a strong motivation for the preparation of Rh nanoparticles with improved activity by optimization of their crystallographic structure. However, compared to other *fcc* metals, the development of synthetic protocols to control size and shapes of Rh nanoparticles has been more challenging because of the high surface free energy of this metal, which is three and two times higher than those of Au and Pt, respectively.[250] Notwithstanding, early studies quickly demonstrated the possibility to control both the efficiency and selectivity of Rh catalysts, by controlling the synthesis of nanospheres, nanocubes, and nanotetrahedra.[251,252] These works showed the

https://doi.org/10.1021/acs.chemrev.3c00033
Chem. Rev. 2023, 123, 3493−3542

tendency of Rh to yield polygonal and multipod structures.[253−255] The preparation of Rh nanotriangles was reported in 2011 by Biacchi and Schaak, applying a kinetic growth control using $RhCl_3$ as metal precursor and triethyleneglycol as the solvent and reducing agent, in a polyol synthetic scheme.[256] High resolution TEM analysis confirmed the {111} nature of the extended facets, but the lack of a complete 3D analysis prevent the identification of the presence of twin defects in the nanocrystals. The optimization of colloidal synthetic strategies in subsequent years focused mainly on the preparation of ultrathin nanosheets and high-index faceted nanocrystals, to maximize the catalytic performance. Son and co-workers reported the preparation of ultrathin Rh nanoplates, exploiting a weak Rh(I)−Rh(I) interaction that is enhanced by van der Waals interactions when the metal precursor is coordinated by oleylamine molecules.[257] The resulting Rh nanoplates present a thickness of only 1.3 ± 0.2 nm and a triangular or trapezoidal profile, with angles of 60 and 120°. Side-view HRTEM analysis confirmed the presence of stacking faults along the [111] direction.[257] More recently, Huang et al. re-evaluated this oleylamine-mediated synthetic route.[258] Specifically, $Rh(ac)_3$, glucose, and oleylamine were mixed in *N*,*N*-dimethylformamide to yield Rh tetrahedral, concave tetrahedral, and hexagonal nanoplates. Shape selectivity was achieved by reducing the reduction rate, thus inducing the formation of kinetic products. The obtained 2D particles showed improved performance for both hydrogen evolution and oxygen evolution reactions.[258] In a different approach, Zheng and co-workers adapted a Rh precursor to the synthetic methodology previously developed for the preparation of Pd ultrathin nanosheets.[180] Specifically, Rh platelets were obtained in *N*,*N*-dimethylformamide, using PVP as capping agent and carbon monoxide as shape inducing agent (Figure 17B).[259] The platelets had an average thickness of 0.9 ± 0.4 nm, corresponding to 3−5 atomic layers, whereas the edge length could be varied between 120 and 1300 nm.

Several solvothermal approaches have also been explored for the preparation of ultrathin Rh nanosheets.[260] In a recent publication, Zhang et al. reported the preparation of hyperbranched triangular Rh nanoplates by heating a mixture of $RhCl_3$ and 1-octadecylamine in a Teflon autoclave, achieving a final thickness of 4 nm and edge length around 200 nm.[261] In another example, Duan et al. reported the solvothermal preparation of monoatomically thin Rh sheets combining $Rh(acac)_3$, benzyl alcohol, formaldehyde, and PVP as capping agent.[262] The authors reported a thickness <4 Å and an edge length of 500 nm, with a structure composed of 100% surface atoms (Figure 17C). The possibility to stabilize such a configuration arises from the combination of a δ-bonding framework composed of the $d_{z^2} - s$ hybrid orbitals in Rh atoms and the stabilizing role of PVP molecules. Interestingly, HRTEM analysis showed a hexagonal atomic organization, but electron diffraction indicated an *hcp* structure instead of the expected *fcc* for Rh. This is likely a direct consequence of the monatomic thickness of these nanosheets.

3.1.6. Aluminum. Al is the most abundant metal composing the Earth's crust, thereby holding a great potential as a low-cost plasmonic material for optical applications.[263] However, similarly to other highly reductive materials, the wet-chemical synthesis of well-defined anisotropic structures has proven to be a difficult challenge. Several research groups have made significant progress, managing to tune the syntheses of spherical, cubic, bipyramidal, and even rod-shaped particles.[264−268] In all cases, the key and unique feature of Al nanocrystal growth is the formation of a 2−3 nm oxide layer surrounding the nanoparticles.[269−271] For example, the selective oxidation of different crystallographic facets in growing Al nanocrystals was exploited by Luo et al. for the preparation of sub-2 nm Al nanosheets, which remains the only report to date.[89] The authors injected a mixture of oxygen and nitrogen gas in the growth solution to regulate the concentration of oxygen during the reduction of $AlCl_3$ precursor by $LiAlH_4$ at 140 °C. When the oxygen content was increased from 15 to 50 vol%, the thickness of the obtained Al nanosheets decreased from 18 to 1.5 nm (Figure 17D). Interestingly, the thickness of the oxide layer was estimated to be <0.5 nm, significantly less than that reported in other studies. A similar approach could potentially be applied to other highly reductive metals such as Ni or Cu.

3.1.7. Iridium. Ir is one of the most promising catalysts within the platinum group. In its metallic state, Ir presents 7 electrons distributed in its 5d orbitals. This configuration enables the adsorption of small molecules (e.g., carbon monoxide, oxygen, hydrogen, ethylene, acetylene) to form reaction intermediates that ultimately enhance the catalytic performance of the material.[272] Ir nanoparticles outperform state-of-the-art catalysts in several organic reactions, including hydrogen and oxygen evolution, (de)hydrogenation, cyclization, and (cyclo)isomerization reactions.[273−277] On top of this outstanding catalytic performance toward organic reactions, Ir nanoparticles were reported to exhibit enzyme-like activity.[278−282] Moreover, Ir nanoparticles were also used for the surface-enhanced Raman scattering (SERS) detection of various analytes.[283−285] This capability is particularly interesting when combined with the superior catalytic activity of Ir nanocrystals, as it may open up the possibility to simultaneously perform and monitor specific chemical reactions within a single material. Finally, Ir colloids display interesting luminescence properties.[272,286,287] Despite the versatile nature of this element, little attention has been dedicated so far to the preparation of Ir nanoparticles, which have mainly focused on small spherical colloids.[278,288] The first characterization of anisotropic Ir nanostructures was reported by Kundu and Liang in 2011.[289] In this work, the photochemical reduction of $IrCl_3$ was performed under 4 h of continued UV light irradiation of a basic 1,2-dihydroxynaphthalene solution in the presence of CTAB. By reducing the surfactant concentration, the authors were able to direct the synthesis toward the formation of spherical nanoparticles, nanochains, nanoflakes (Figure 17E), and nanoneedles.[289] Most recently, the preparation of two-dimensional Ir nanostructures has acquired increased attention when Cheng et al. reported the preparation of ultrathin Ir nanosheets.[290] Carbon monoxide was identified as the shape directing agent that stabilizes {111} facets during growth, under similar conditions reported for other *fcc* metals of the platinum group. Additionally, some theoretical works have recently analyzed the adsorption of carbon monoxide on the different crystallographic facets of an Ir crystal, suggesting the possibility of achieving selective growth of both platonic shapes and anisotropic structures, such as rods or plates.[291−293] This certainly represents an exciting opportunity for future research endeavors toward the development of new catalysts.

3.1.8. Lead. Despite its toxicity, Pb nanostructures are attractive candidates for the study of quantum effects on superconductivity, with applications in electronics, spintronics, and batteries.[294−296] From a synthetic perspective, the low melting point of Pb represents a unique feature within the *fcc* metal family. This feature enables a new mechanism, called solution-liquid−solid mechanism, where, upon reduction of the

https://doi.org/10.1021/acs.chemrev.3c00033
Chem. Rev. 2023, 123, 3493−3542

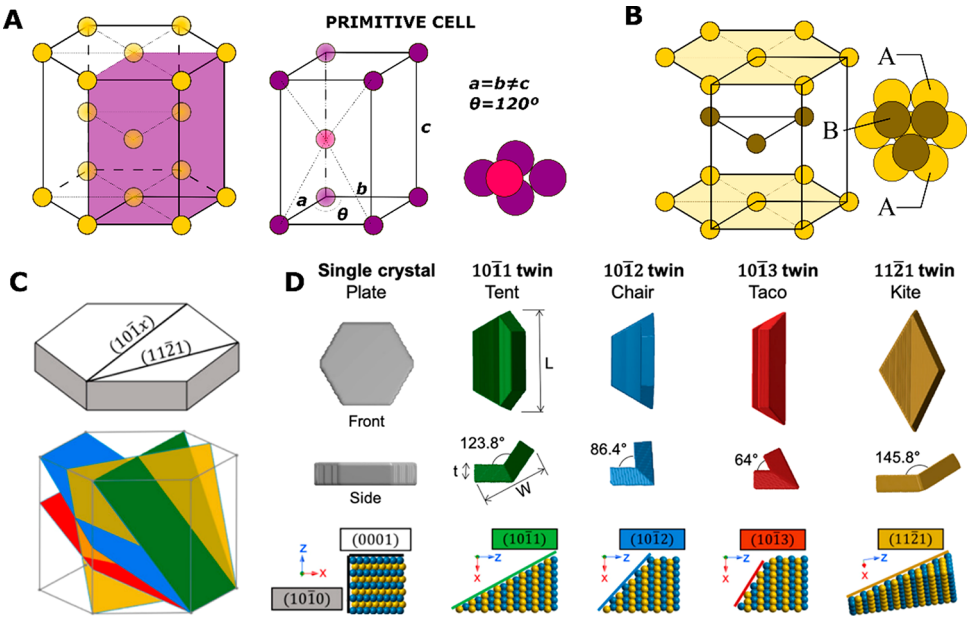

Figure 18. *hcp* crystallographic habit.[41] (A,B) 3-Dimensional spatial arrangement of the unit cell of an *hcp* crystal (A) and its primitive cell (B), in orthogonal view (left) and top view (right). (C) Representation of the unit cell crystallographic facets and multiple low-energy twin planes. Adapted with permission from ref 307. Copyright 2020 American Chemical Society under CC BY 4.0 http://creativecommons.org/licenses/by/4.0/). (D) Predicted Wulff shapes for single-crystalline and monotwinned structures with predominant (0001) facets. Adapted with permission from ref 307. Copyright 2020 American Chemical Society under CC BY 4.0 http://creativecommons.org/licenses/by/4.0/.

precursor, metallic Pb nanoparticles would exist either in solid or liquid state depending on their size, as the higher surface energy of the smaller colloids would reduce the melting point below the temperature used for growth.[297,298] Two-dimensional Pb nanoparticles where first documented in 2004 by Wang et al., as a byproduct of the synthesis of high aspect ratio single-crystal nanowires.[297] In this work, a polyol growth approach in the presence of PVP was applied for the reduction of Pb acetate. A few years later, a kinetically controlled polyol approach was optimized by Jaeger and co-workers, where PVP was substituted by trioctylphosphine and oleic acid. Optimizing the temperature and reaction time, Pb nanoplates with thicknesses ranging between 20 and 100 nm, and a lateral size of several micrometers were obtained as the main product.[299] Extensive SAED analysis confirmed the {111} nature of the two parallel facets, as well as the presence of the forbidden 1/3{422} diffraction signal. A different approach was proposed in the same year by Lu et al., in which the kinetic formation of platelets and hemispherical nanoparticles was achieved by combining PVP and CTAB in certain molar ratios inside the growth mixture (Figure 17F).[298] Magnetic measurements of isotropic, anisotropic, and 2D Pb nanostructures confirmed a superconducting behavior below a critical temperature of ∼7 K, with a Meissner effect 1 order of magnitude smaller compared to the bulk material.[295]

3.1.9. Ytterbium. As with other rare earth elements belonging to the lanthanide group, Yb finds application as a photon upconverting material for the preparation of contrast agents for *in vivo* imaging.[300−303] Some research groups have explored the preparation of ytterbium oxide nanodisks.[304] However, the preparation and characterization of Yb metal nanoplates/disk/sheets remain undiscovered territory.

3.2. *hcp* Metals

Hexagonal close-packed (*hcp*) is another common crystal structure due to its high coordination number (CN = 12), yielding a highly stable close-packed arrangement (atomic packing factor of 74%, same as for *fcc*). Here, atoms are arranged in a close-packed *AB*−*AB* stacking (Figure 18A,B), resulting in different low-energy planes, twinning planes, and crystal shapes, compared to *fcc*. In the case of the *hcp* structure, a four Miller−Bravais indices system is used (*hkil*), where a fourth *u*-axis is constructed with a 120° angle from both the *a* and *b* directions.[305] In this reference system, the {0001} plane family is basal to the unit cell, perpendicular to the *c* direction, and is close-packed, consequently presenting the lowest surface energy.[30] Importantly, unlike the *fcc* system, where the lowest energy {111} planes present 8 equiv directions, in the *hcp* system, only two directions exist within the {0001}. This implies that the Wulff construction for an *hcp* crystal results in the formation of plates with a hexagonal shape, which are single crystals, with the remaining 6 facets belonging to the {10$\bar{1}$0} family of planes (Figure 18C). The different stacking arrangement also implies different twin planes, which for *hcp* can readily occur along the (10$\bar{1}$x) plane, with $x = 1, 2$, and 3, and the (11$\bar{2}$y) plane, with $y = 1, 2, 3$, and 4.[306] The different twinning behavior creates new anisotropic morphologies, including tents, chairs, tacos, and kites (Figure 18D).[307] Apart from the standard *hcp* lattice, several lanthanide elements adopt a characteristic variation named double *hcp* (*dhcp* or *La-type*), adopting a 4-layer stacking pattern *ABACABAC*, combining the *AB*−*AB* stacking of *hcp* with the *ABCABC* of *fcc*. However, none of these elements (La, Ce, Pr, Nd, and Pm) have been synthesized as metallic platelets, and therefore will not be analyzed further.

Thanks to its high stability and packing density, the *hcp* crystallographic group contains a wide variety of metals at standard temperature and pressure conditions (Figure 15). This includes elements of the third (Sc, and Y) and fourth group (Ti, Zr, and Hf), the former being soft metals prone to oxidation, whereas the latter are ductile and corrosion-resistant. Other d-block *hcp* elements include catalytically relevant elements (Re, Ru, and Os), as well as important elements for the battery industry (Co, Cd, and Zn). We also find two s-block elements

https://doi.org/10.1021/acs.chemrev.3c00033
Chem. Rev. 2023, 123, 3493−3542

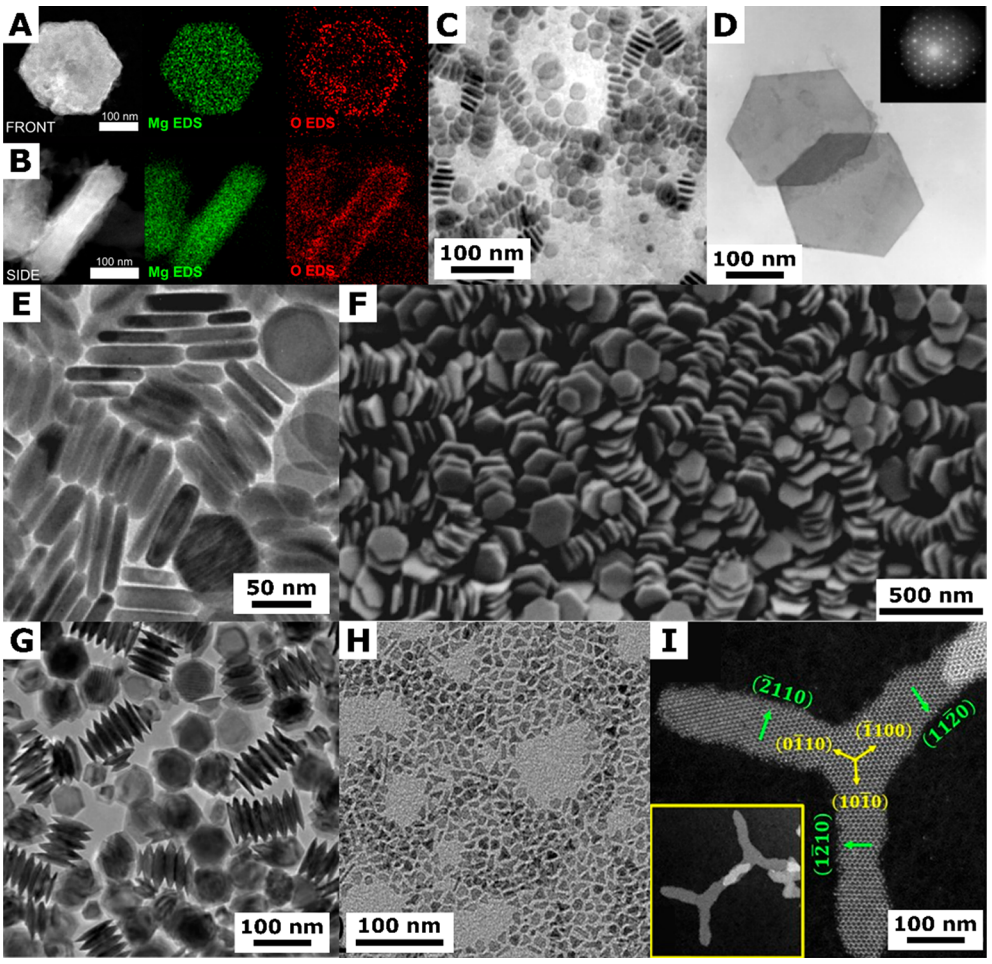

Figure 19. *hcp* nanoplates. (A,B) HAADF-STEM images and corresponding Mg and O STEM-EDS maps of a Mg nanoplate synthesized using Li naphthalide as reducing agent. The platelet is oriented (A) perpendicular and (B) parallel to the electron beam. Adapted with permission from ref 331. Copyright 2018 American Chemical Society. (C) Co nanodisks prepared by thermal decomposition of $Co_2(CO)_8$ in a mixture of oleic acid and trioctylphosphine oxide in dichlorobenzene. Adapted with permission from ref 339. Copyright 2002 American Chemical Society. (D) Co nanoplates synthesized through the reduction of $CoCl_2$ by NaH_2PO_2 in a basic aqueous solution. Inset: SAED pattern of the flat face of a single nanoplate. Adapted with permission from ref 341. Copyright 2009 Elsevier. (E,F) Zn hexagonal nanoplates synthesized via $LiN(SiMe_3)_2$ reduction, in the presence of a noncoordinating solvent such as octadecene. Adapted with permission from ref 348. Copyright 2015 American Chemical Society. (G) Ru capped nanocolumns prepared by hydrothermal decomposition of $RuCl_3$ in the presence of formaldehyde and sodium oxalate. Adapted with permission from ref 354. Copyright 2012 American Chemical Society. (H) Ultrathin Ru nanoplates obtained as the main product of the hydrogenation of [Ru(COD)(COT)] in the presence of both hexadecylamine, and lauric acid. Adapted with permission from ref 359. Copyright 2022 American Chemical Society. (I) High-resolution HAADF-STEM image of a Ru 3-fold star. Inset: image at lower magnification showing two 3-fold stars with overlapping branches, Adapted with permission from ref 359. Copyright 2022 American Chemical Society.

(Be and Mg) and several members of the rare-Earth f-block group (Gd, Tb, Dy, Ho, Er, Tm, Lu) in the *hcp* family, which is completed by the post-transition metal Tl. Despite such a variety of elements, only a few of them have been investigated for the preparation of 2D colloidal nanoparticles in their metallic form. Apart from the scarcity of the elements of the f-block, other reasons to explain this may include the difficulty of isolating the pure form of some of the metals (e.g., Hf or Zr), as well as the high oxophilicity of many members of the *hcp* family (e.g., Ti, Re, Gd).[308−318]

3.2.1. Magnesium. Mg holds great promise for several industrially relevant fields, including hydrogen storage and rechargeable batteries.[319−324] Its abundance and low cost are also important contributing factors that motivate deeper investigation on the fabrication of magnesium nanostructures. Top-down fabrication and gas-phase deposition were initially investigated,[322,325] showing sufficient size and shape control to yield the first preparation of Mg nanoplates.[326,327] On the other hand, the chemical synthesis of Mg colloids remained vastly unexplored until very recently, when Mg nanoparticles emerged as alternative plasmonic materials to the more expensive coinage metals.[328,329] In 2012, Viyannalage et al. reported the first wet-chemical synthesis of Mg nanoplates, using Li naphthalide as the reducing agent.[330] The synthesis was later optimized by Ringe's group (Figure 19A,B) in a series of seminal papers demonstrating the possibility of Mg plasmonics to target intense optical activity throughout the whole UV−vis−IR spectral range.[324,331] The particles ranged between 100 and 300 nm in size, with three main plasmon resonances, two of them in the UV range and one occupying the vis-NIR, respectively.[329,331,332] The *hcp* structure of metallic Mg was confirmed for the nanoplates, which are single crystalline and expose low index facets belonging to the {0001} (top and bottom) and {10$\bar{1}$0} (six sides) families of planes. The wet-chemical synthesis of Mg colloids is still in its infancy, and much is left to uncover prior to shape and size control.[333] Similar to Al, Mg nanoparticles also

https://doi.org/10.1021/acs.chemrev.3c00033
Chem. Rev. 2023, 123, 3493−3542

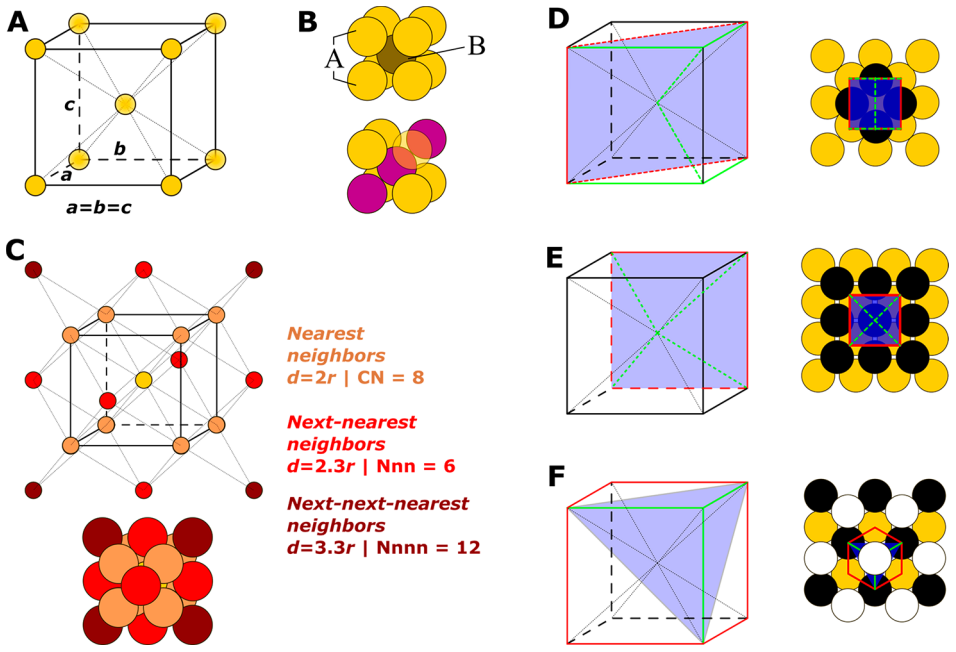

Figure 20. *bcc* crystallographic habit.[41] (A) Three-dimensional spatial arrangement of the unit cell in a *bcc* crystal. (B) Hard-sphere model of a bcc unit cell; the atoms are in contact along the body diagonal (bottom). (C) Representation of the distribution of nearest neighbors (giving a CN of 8) and next-nearest neighbors (Nnn) in a *bcc* crystal. The high number of Nnn and their close distance (only 15% higher compared to the nearest neighbors) contributes significantly to the overall stability. (D–F) Top view representation of the three main crystallographic directions in the order of stability, from the most to the less stable: {110} (D), {100} (E), and {111} (F); in F, the atom at the volumetric center of the cubic unit cell is not visible.[362,368]

form a thin self-protecting oxide layer which keeps them stable in low-oxidative environments such as air (few hours) or alcoholic suspensions (weeks).[331,334] This might be improved in the future through surface chemistry and other protective layers.[335]

3.2.2. Cobalt. The preparation of anisotropic Co nanoparticles can find potential applications as ferrofluids and high density magnetic memory devices.[336] The rational synthesis of Co colloids is particularly challenging due to its rich crystallography, presenting *fcc*, *hcp*, and *epsilon* (ε) crystal habits.[337] At the nanometer scale, the three crystal phases are readily interchangeable, with ε-Co becoming the most stable form above 200 °C.[338] The first preparation of Co nanodisks in pure *hcp* crystal phase was reported in 2002 by Puntes et al., exploiting the thermal decomposition of Co carbonyl organometallic compounds in the presence of linear amines and trioctylphosphine oxide (Figure 19C).[339] The obtained nanodisks showed a narrow size distribution and high tendency to assemble into chain like structures.[337,339,340] Several years later, multiple hydrothermal approaches were reported, achieving higher aspect-ratio Co nanoplates with improved magnetic properties (Figure 19D).[229,341,342] Interestingly, the formation of Co nanoplates has also been explored in the presence of external electromagnetic fields, which would be particularly interesting when nanostructures are grown directly on substrates.[343]

3.2.3. Zinc. By far the most abundant use of Zn in colloidal systems is the production of ZnO particles,[344] a wide-bandgap semiconductor with an energy gap of 3.37 eV that finds numerous applications in catalysis, sunscreen products, and food packaging.[345] However, the wet-chemical synthesis of metallic Zn nanoparticles was also investigated by several groups.[346,347] In 2014, the group of M. V. Kovalenko reported the only synthetic protocol for the preparation of hexagonal metallic Zn nanoplates to date.[348] Specifically, the synthesis is based on the use of $LiN(SiMe_3)_2$ for the transient formation of metallic amide complexes that are thermally decomposed *in situ*. The growth of hexagonal nanoplates is induced by combining oleylamide complexes and a noncoordinating solvent such as octadecene.[348] The prepared colloids present a single crystal *hcp* structure and a narrow size distribution between 40 and 200 nm (Figure 19E,F).

3.2.4. Ruthenium. Ru nanocrystals are effective catalysts for several heterogeneous and electrocatalytic reactions, including Fischer–Tropsch, hydrogenation, CO oxidation and methanation, and hydrogen production through amine borane dehydrogenation, or water-splitting reactions.[349,350] Similar to Co, Ru can also generate stable crystal structures with both *fcc* and *hcp* atom arrangements, which has significant implications for their catalytic activity.[351−353] The relatively low oxidation and reduction potentials represent the main challenge when controlling the growth of Ru nanoparticles. Nonetheless, the rational synthesis of metallic Ru nanocrystals has been optimized for the preparation of various unique morphologies, including capped columns and hourglasses.[354,355] For the specific case of 2D nanocrystals, the first report of a nanoplate synthesis was achieved by means of a polyol approach.[356] A few years later, the hydrothermal decomposition of $RuCl_3$ in the presence of formaldehyde led to the synthesis of triangular but irregular Ru nanoplates, with an average edge length of 24 nm and a thickness of less than 4 nm.[354] Interestingly, these triangular platelets presented a large number of stacking faults in their XRD analysis despite showing an *hcp* crystal habit. The formation of defects is probably related to the high reaction temperature and growth rate and is necessary to achieve a triangular shape instead of the hexagonal profile predicted by Wulff construction. In the same work, the authors also explored the use of sodium oxalate as shape directing agent for the preparation of Ru-capped columns. Specifically, oxalate species can selectively adsorb on Ru $(10\bar{1}0)$ during the initial growth stage, inducing the formation of the column trunk; over the

https://doi.org/10.1021/acs.chemrev.3c00033
Chem. Rev. 2023, 123, 3493−3542

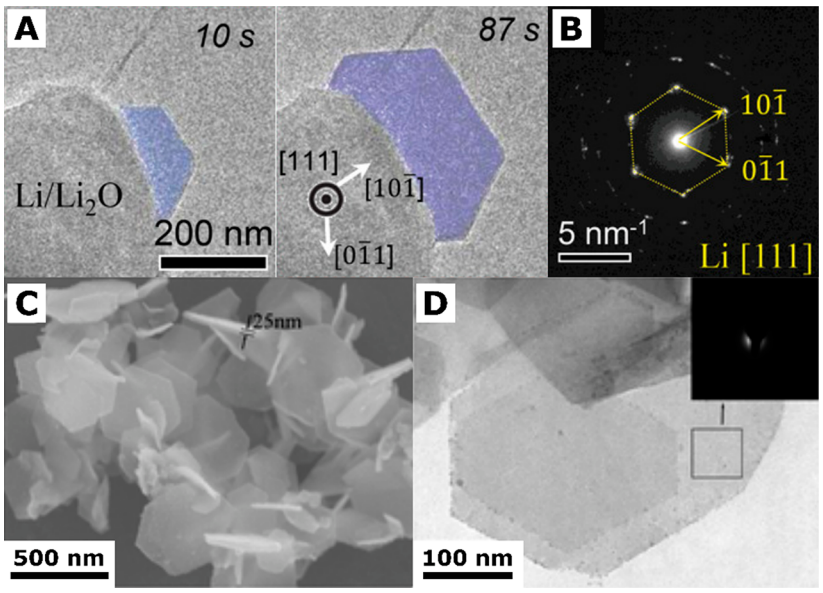

Figure 21. *bcc* nanoplates. (A) Electrochemical growth in a solid-state open-cell configuration of a hexagonal ultrathin Li nanoplate imaged by TEM at two different times. Adapted with permission from ref 369. Copyright 2021 Wiley. (B) SAED pattern of the extended face of the growing nanoplate, confirming the *bcc* crystal structure. Adapted with permission from ref 369. Copyright 2021 Wiley. (C,D) SEM (C) and TEM (D) imaging of amorphous Fe nanoplates obtained by chemical reduction of $FeSO_4$ by NBH_4 assisted by an external magnetic field. Inset: SAED pattern showing no diffraction points, thus confirming the amorphous nature of the Fe nanoparticles. Adapted with permission from ref 371. Copyright 2012 Royal Society of Chemistry.

course of the reaction, the same oxalate species undergo thermolysis, leading to the overexpression of Ru (0001) facets in their predicted hexagonal profile (Figure 19G).[354,357] The preparation of even thinner 2D Ru nanostructures was reported by Kong et al., who optimized the solvothermal decomposition of $Ru(acac)_3$ in the presence of 2-propanol (contributing to anisotropic growth), and urea (preventing aggregation). The prepared free-standing Ru platelets are several hundreds of nm in size, with a thickness around 1 nm. The huge surface-to-volume ratio of these nanostructures translated into a remarkable catalytic activity toward both hydrogen and oxygen evolution reactions.[358] In a recent report, Ramamoorthy et al. explored an organometallic route for growing Ru icosahedral, triangular, and 3-fold nanostars (Figure 19H, I).[359] The proposed approach revolves around the hydrogenation of a [Ru(COD)(COT)] complex in the presence of hexadecylamine and lauric acid. The authors identified the CO generated *in situ* from the catalyzed decomposition of lauric acid as the key shape directing agent, stabilizing the icosahedral crystals at high concentration, and the 2D growth of the *hcp* crystals at lower concentration. The prepared 3-fold Ru nanostars have a dimension around 10 nm and a thickness of only 0.8 nm (corresponding to 5 or 6 atomic layers) and a standard deviation around 15%.[359]

3.3. *bcc* Metals

In the *bcc* lattice system, atoms are placed at each corner of a cube, with an additional atom in the volumetric center of the cubic unit cell, so that in a hard sphere model the atoms are in contact along the body diagonal (Figure 20A,B). The *bcc* lattice is very common within metals and presents a CN of 8 and an atomic packing factor of 68%, with a different stability order for low-index facets, as compared to *fcc*: $\gamma_{\{110\}} < \gamma_{\{100\}} < \gamma_{\{111\}}$ (Figure 20D−F).[360] As such, *bcc* is not a close-packed system, making *bcc* metals generally less dense and less ductile compare to *fcc* metals. Nonetheless, *bcc* metals typically display a characteristic ductile-to-brittle transformation temperature, following the thermal activation of slip systems within the crystals.[361] Despite the lack of a close-packed arrangement, *bcc* metals can be relatively stable, due to the high number of next-nearest atomic neighbors (Figure 20C) and are gaining traction in the colloidal community for the preparation of new nanocrystal shapes through twinning, which are not available for more standard metals such as Au or Ag.[362] The *bcc* family is composed of several s-block elements (Li, Na, K, Rb, Cs, Fr, Ba, and Ra), and d-block transition metals of the fifth (V, Nb, and Ta) and the sixth group (Cr, Mo, and W), with the addition of Fe and the rare-earth element Eu (Figure 15). Some of these 16 elements have been investigated for the preparation of metallic nanoparticles,[363−367] but we could only find two reported cases of metallic nanoplates.

3.3.1. Lithium. Li is the lightest and simplest of all metals, as well as the element that can best approximate a quasi-free-electron model, representing a unique opportunity for the fundamental understanding of size-dependent physical properties.[369,370] In a recent publication, Sun et al. reported the electrochemical growth of hexagonal ultrathin Li nanoplates using a solid-state open-cell configuration inside a TEM.[369] The high-vacuum conditions enable the full characterization of such a highly reactive structure, showing an edge length of few hundreds of nm against a thickness <10 nm (Figure 21A,B). The authors were able to confirm the *bcc* nature of the nanoplates, with the top and bottom facets identified as (111) planes, and the 6 side facets assigned to the {110} family.[369] The proposed mechanism involves the preferential oxidation of the basal (111) facets to break the symmetry of the growing crystal, ultimately preventing any growth along the [111] direction. The presence of an extremely low concentration of oxygen within the TEM column did not prevent the oxidation of the Li nanoplates indefinitely, with a complete transformation into Li_2O within about 3 h. Nonetheless, the authors were able to confirm the plasmonic nature of the grown structures by cathodolumines-

https://doi.org/10.1021/acs.chemrev.3c00033
Chem. Rev. 2023, 123, 3493−3542

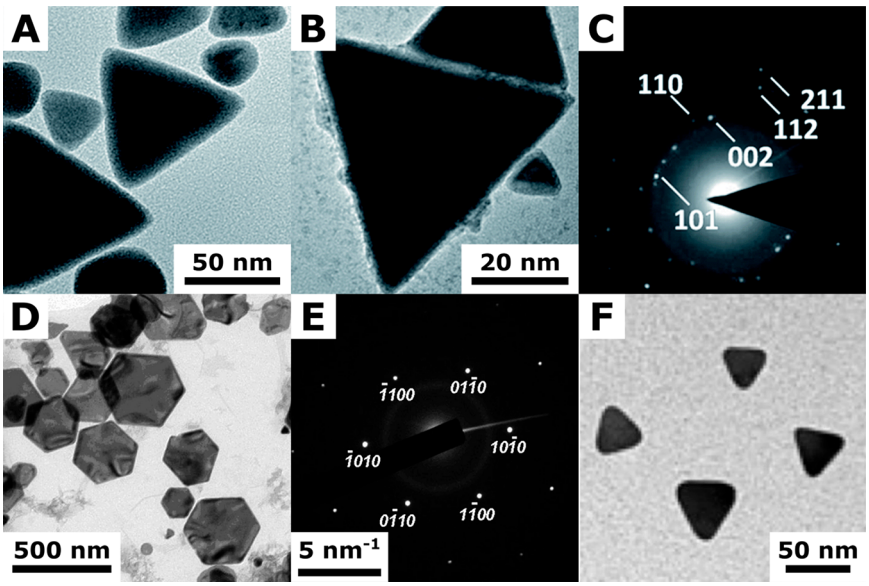

Figure 22. Nanoplates with noncubic crystallography. (A−C) In nanotriangles synthesized via $InCl_3$ reduction by $NaBH_4$ in the presence of PVP; SAED analysis (C) confirmed the expected tetragonal crystal structure. Adapted with permission from ref 385. Copyright 2017, Royal Society of Chemistry under CC BY-NC 3.0. (D,E) Bi hexagonal nanoplates obtained by solvent-free thermolysis of Bi thiolate precursors in the presence of excess 1-dodecanoethiol. SAED analysis (E) confirmed the expected rhombohedral crystal structure. Adapted with permission from ref 399. Copyright 2010 American Chemical Society). (F) Single-crystal Bi nanotriangles resulting from the hydrothermal reduction of $Bi(NO_3)_3$ in alkaline conditions by ascorbic acid, in the presence of Na_2EDTA, and carboxylic acid-terminated PVP. Adapted with permission from ref 402. Copyright 2022 Elsevier.

cence (CL) and electron energy loss spectroscopy (EELS). A similar setup was also applied for the growth of Na nanoplates, but the synthesis was found to be less reproducible.

3.3.2. Iron. Magnetic Fe nanoparticles have been extensively investigated in several oxidation states and crystallographic habits. In 2012, Guan et al. reported the external field-assisted preparation of 2D Fe nanoplates by $NaBH_4$ reduction of a concentrated $FeSO_4$ solution. Interestingly, the prepared 2D nanostructures featured an amorphous phase (Figure 21C,D), with significantly enhanced coercivity and decreased saturation magnetization.[371] The authors suggested that the obtained nanoplates are a kinetic product generated by the formation of a large number of Fe nuclei via reduction, which are subsequently assembled by the external magnetic field.

3.4. Metals with Other Crystallographic Habits

Metallic elements can present other crystallographic arrangements (Figure 15), such as orthorhombic (Ga), body-centered tetragonal (In), diamond cubic and tetragonal (Ge and Sn, respectively), and rhombohedral (Hg, Sb, and Bi).[372−381] Regarding the preparation of 2D metallic nanoparticles, two cases deserve a deeper discussion in the context of this review.

3.4.1. Indium. In is a low melting point metal (157 °C) that has found applications in electronics, catalysis, and as a component of several alloys. Moreover, metallic In nanoparticles are attractive for their plasmonic properties and superconductivity.[382,383] The first synthesis of In nanotriangles was achieved through a hydride reduction in alkylamine (used as solvent); specifically, Li borohydride was used to reduce In trichloride ($InCl_3$) in *N*,*N*-diethylaniline, resulting in the growth of polyhedral nanocrystals, with significant size and shape polydispersity.[384] A polyol method has been optimized for the room temperature growth of In nanotriangles and nanowires displaying a high level of control over morphology and size.[385] In this protocol, $NaBH_4$ tetraethylene glycol solution was added dropwise into an $InCl_3$ and PVP ethylene glycol solution after nitrogen purging. Interestingly, the formation of wires or triangular nanoplates was controlled by varying the rate of addition of the reducing agent, pointing toward a kinetic control of the growth. The In nanotriangles present an edge length of 60 ± 8 nm and a shape-yield >50%, with SAED analysis confirming the expected tetragonal crystal structure (Figure 22A−C). Although control over the growth kinetics can certainly be improved, the authors were able to study the plasmonic properties of the prepared colloids, and demonstrated their use for the SERS detection of tryptophan.[385] Finally, the study of In nanoparticle synthesis led to the preparation of one-dimensional hierarchical multilayered nanostructures.[386] This exotic shape originates from the initial incorporation of Zn atoms within In nanorods, which are later removed from the structure (following a chemical gradient), inducing a ripening process of the remaining architecture.

3.4.2. Bismuth. As a bulk material, Bi is a metalloid with a small band overlap, and the element presenting the smallest electron effective mass. The size reduction of Bi crystals into the nanometer scale yields an unusual metalloid-to-semiconductor transition, which finds application in optoelectronics and thermoelectronics applications, as well as in the study of spin−orbit interactions and topological insulators.[387−390] Moreover, Bi nanoparticles are one of the best catalysts for the solid−liquid−solid growth of semiconductor nanorods and nanowires.[391,392] These characteristics attract considerable attention toward the synthesis of Bi colloids under different conditions.[393−396] In one of the first reports, the preparation of Bi nanoplates was achieved using PVP as reducing agent and stabilizer in a polyol method: the ratio between PVP and $NaBiO_3$ could be tuned for the preparation of Bi nanocubes (PVP:Bi = 1.6) or Bi nanotriangles (PVP:Bi = 0.8), with a shape yield around 30%.[397] Moreover, trace amounts of Fe^{3+} induced the formation of thin Bi nanobelts of several micrometers in length and up to 600 nm in width. By changing the Bi precursor to $Bi[N(SiMe_3)_2]_3$, Wang et al. reported the preparation of Bi

https://doi.org/10.1021/acs.chemrev.3c00033
Chem. Rev. 2023, 123, 3493−3542

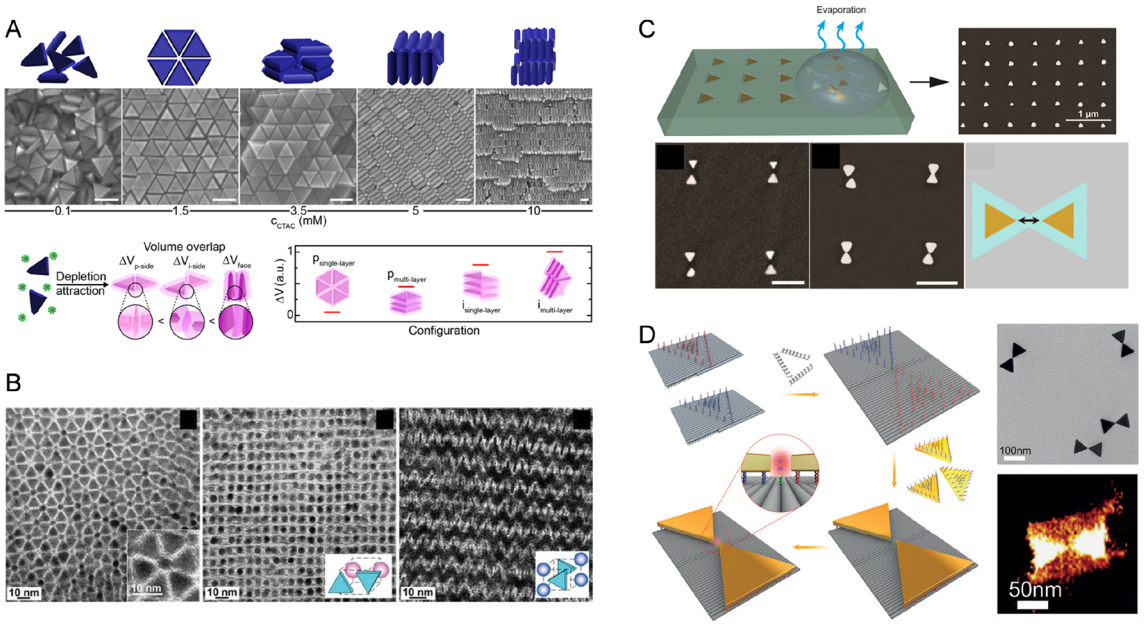

Figure 23. Self-assembly of nanoplates. (A) Depletion attraction-driven self-assembly of Au nanotriangles under different initial CTAC concentrations ranging from 0.1 to 10 mM. Schematics below show different configurations of self-assemblies. Scale bars: 100 nm. Reproduced with permission from ref 406. Copyright 2017 American Chemical Society. (B) TEM images of binary superlattices self-assembled from nanotriangles and nanospheres. The schematics at the corner illustrate the proposed unit cell. Reproduced with permission from ref 414. Copyright 2006 Nature Publishing Group. (C) Schematic process and resulting product of large-area template-assisted self-assembly of Au nanotriangles. Scale bars: 500 nm. Reproduced with permission from ref 411. Copyright 2014 American Chemical Society. (D) Schematic self-assembly procedure of Au bowties directed by DNA origami (left), and the TEM and AFM images of the resulting Au bowties (right). Reproduced with permission from ref 409. Copyright 2018 Wiley-VCH.

nanoplates with a hexagonal profile and significantly smaller dimensions (50−100 nm) at a shape-yield around 60%.[398] Taking advantage of the relatively low melting point of Bi (271.4 °C in the bulk), Wang et al. reported the preparation of Bi hexagonal nanodisks in a solvent-free thermolysis process.[399] The formation of disks was induced by the selective adsorption of 1-dodecanethiol on the different facets of rhombohedral Bi nanocrystals, while the same molecule was also responsible for initiating the growth through a radical process, leading to the reduction of Bi thiolate (Figure 22D). The authors were also able to roughly control the edge length of the grown disks by varying the reaction temperature, the reaction time, and the concentration of the capping agent. After optimization, Bi nanodisks showed an edge length of 100−260 nm and an average thickness of 17 nm, with a size polydispersity around 15%. The single-crystal rhombohedral structure was confirmed by SAED, with flat faces perpendicular to the *c*-axis (Figure 22E).

More recently, Bi emerged as an interesting material for biological applications, with Bi nanoparticles showing low toxicity levels and the ability to stimulate the generation of reactive oxygen species (ROS).[400,401] In this context, Song et al. synthesized Bi nanotriangles of around 50 nm edge length and functionalized them with Zn protoporphyrin IX and human serum albumin for the sonodynamic treatment of rheumatoid arthritis.[402] The Bi nanotriangles were synthesized through an optimized hydrothermal process in alkaline conditions using ascorbic acid as the reducing agent and Na_2EDTA to complex $Bi(NO_3)_3$ and regulate the release of Bi^{3+} during growth (Figure 22F), while a carboxylic acid-terminated PVP was used as surfactant.[402,403]

4. SELF-ASSEMBLY

Progress in various self-assembly techniques allows for organizing randomly distributed metal nanoplates from colloidal dispersions into monolayers on substrates,[404,405] close-packed assemblies,[406,407] colloidal dimers or clusters,[408−410] periodic arrays,[411−413] and 3D superlattices.[414] Self-assembly can be regarded as an effective approach to tailor the collective optical properties of metal nanoplates and to incorporate them into functional substrates.[17,412]

One of the first examples of the self-assembly of metal nanoplates was shown by Mirkin and co-workers, in which particles were functionalized with thousands of DNA strands, the sequence-specific hybridization of which provided the thermodynamic driving force for their attraction and self-organization.[16] The authors found that the large, atomically flat basal planes of the nanoplates resulted in strong face-to-face interactions, resulting in well-defined columnar stacks of repeating particles.[16,415] This approach was later used to engineer biperiodic one-dimensional superlattices with tunable plasmonic optical properties.[17] In another prominent example, Chen et al. demonstrated random, edge-to-edge and face-to-face assemblies of Au nanotriangles by varying the CTAC concentration in the initial solution before solvent evaporation (Figure 23A).[406] On one hand, the positively charged CTAC surface layers render the Au nanotriangles electrostatically repulsive. On the other hand, the interparticle depletion attraction forces, which favor the directional attachment of flat facets, are proportional to CTAC concentration.[416] The intensity of these attractive forces depends on the contact area of the interacting particles and have been used by several groups to achieve the selective precipitation of platelets in complex colloidal dispersions containing both isotropic and anisotropic byproducts, effectively purifying the 2D shape.[86,417] The

https://doi.org/10.1021/acs.chemrev.3c00033
Chem. Rev. 2023, 123, 3493−3542

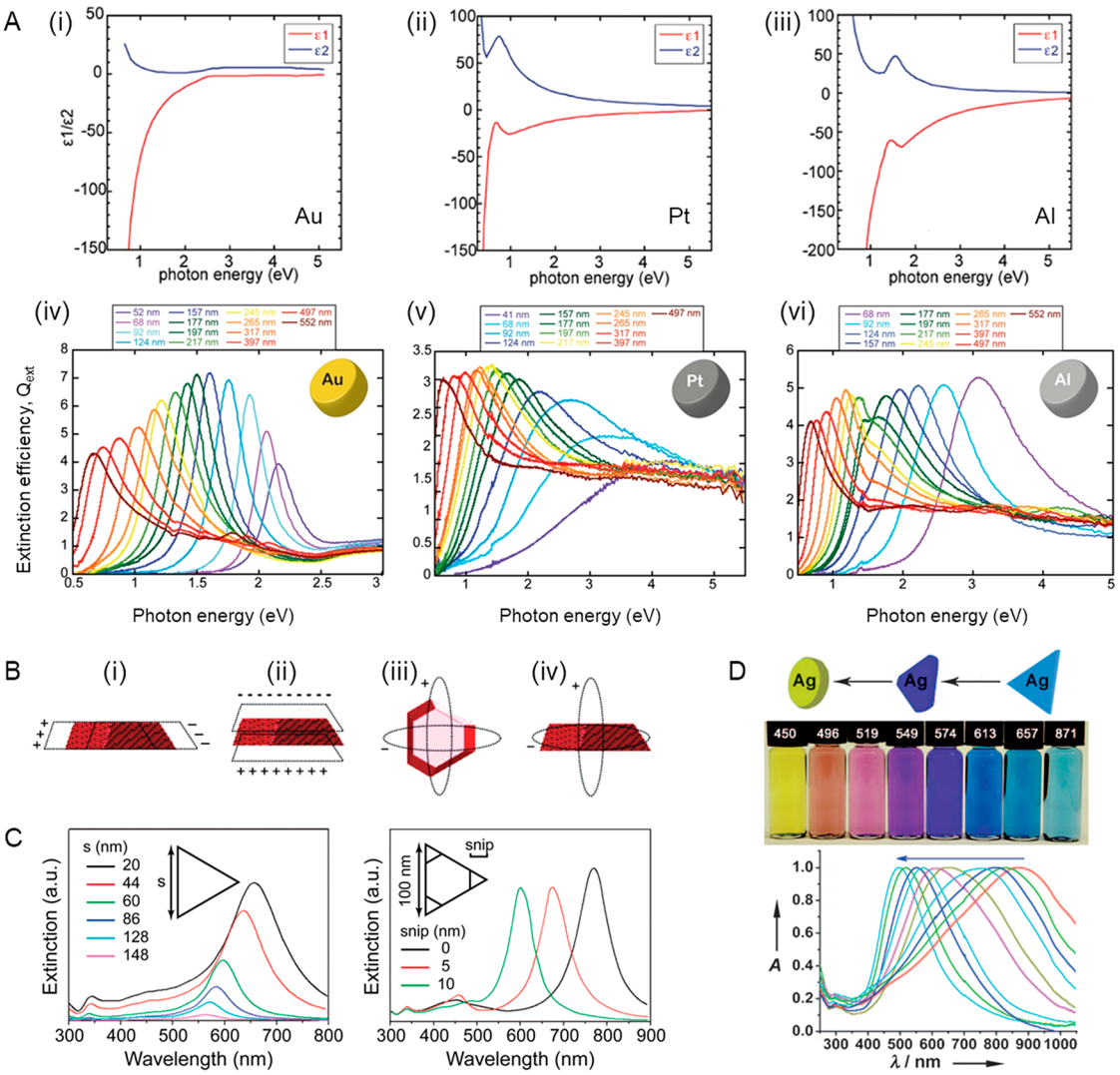

Figure 24. Factors that influence the LSPR mode of 2D plasmonic nanoparticles. (A) Dielectric functions of bulk Au (i), Pt (ii), and Al (iii), and experimentally measured extinction spectra of random arrays of Au (iv), Pt (v), and Al (vi) nanodisks. ε_1 and ε_2 are the real and imaginary parts of the dielectric function. Reproduced with permission from ref 418. Copyright 2011 American Chemical Society. (B) Schematic diagrams of the charge oscillation corresponding to in-plane dipolar mode (i), out-of-plane dipolar mode (ii), in-plane quadrupolar mode (iii), and out-of-plane quadrupolar mode (iv). Reproduced with permission from ref 436. Copyright 2005 American Chemical Society. (C) Simulated extinction spectra of Ag nanotriangles with different edge lengths (left) and snips (right). Reproduced with permission from ref 437. Copyright 2003 American Chemical Society. (D) Schematic diagram, digital photographs, and extinction spectra of Ag nanoplates reshaping from triangular to circular shape, while the thickness of the nanoplates increases. Reproduced with permission from ref 440. Copyright 2009 Wiley-VCH.

electrostatic repulsion and the depletion attraction can reach a complex balance during evaporation processes, leading to different assembly configurations.[406] Similar results can be obtained by varying the evaporation temperature, which affects the atom diffusion rate, solvent evaporation rate, and self-assembly rate.[407] Besides, in an evaporation process, the formation of large-area assemblies requires other optimal conditions, such as appropriate substrate/surface chemistry, nanoparticle concentration, ion concentration, and environmental humidity. Rational control over these factors, i.e., using relatively concentrated colloidal dispersions at ∼45 °C under reduced pressure, as reported by Murray et al., allow for ordered binary assemblies composed of nanoplates and nanospheres (Figure 23B).[414] In the work of van Blaaderen et al., dispersed Au nanotriangles self-assembled into millimeter-sized stacks in colloidal dispersions with varying salt concentrations. Even without the addition of salt, another type of self-assemblies was observed when a weak alternating electric field of high-frequency (E_{rms} = 0.025 V μm^{-1}, f = 200 kHz) was applied, in which the nanotriangles aligned with their major axis parallel to the external electric field.[408] Such close-packed assemblies exhibited improved performance in SERS detection, compared to randomly assembled structures and to individual nanoplates.[404,406]

Given that many interesting breakthroughs on plasmonic sensing have been made using lithographically fabricated bowtie nanostructures, the precise assembly of chemically prepared nanotriangles into tip-to-tip bowtie configurations in high yield has been challenging, even if highly desired. Mirkin and coworkers demonstrated the template-assisted assembly of Au nanotriangles into lithographically defined individual and bowtie-like patterns (Figure 23C), during which the combination of slow solvent evaporation and Brownian motion led the nanotriangles to assemble into the triangular trenches.[411]

https://doi.org/10.1021/acs.chemrev.3c00033
Chem. Rev. 2023, 123, 3493−3542

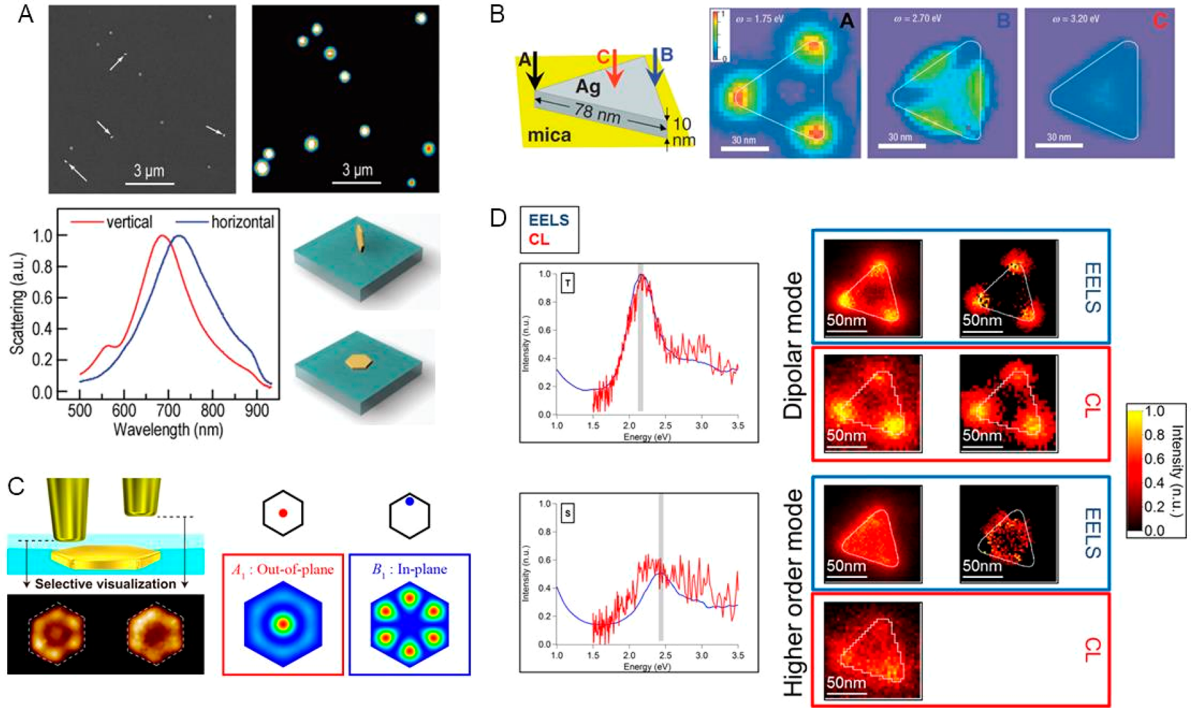

Figure 25. Characterization of characteristic LSPR modes. (A) Single-particle dark-field scattering measurement of vertically and horizontally oriented hexagonal Au nanoplates. (top) Comparison of the SEM and dark-field images of individual Au nanoplates deposited on an ITO substrate. (bottom) Dark-field scattering spectra and schematic diagrams of vertically and horizontally oriented hexagonal Au nanoplates. Reproduced with permission from ref 450. Copyright 2018 Royal Society of Chemistry. (B) Experimental EELS amplitude distributions of a triangular Ag nanoplate. The three maps centered at different energies were resolved from EEL spectra excited at the corner, the center, and the edge of the Ag nanoplate. Reproduced with permission from ref 454. Copyright 2007 Nature Publishing Group. (C) Schematic diagram of SNOM (left top), near-field transmission images measured from a hexagonal Au nanoplate at different near-field probe tip−sample distances (left bottom), and spatial distributions of out-of-plane and in-plane LSPR modes (right). Reproduced with permission from ref 451. Copyright 2019, American Chemical Society. (D) Comparison of EELS and CL spectra taken at the low left tip (T) and left side (S) of the exact same individual Au nanoplate (left), and the EELS and CL maps of the dipolar and higher-order LSPR modes (right). Reproduced with permission from ref 457. Copyright 2013 American Institute of Physics.

However, a drawback of this method is that the yield of bowtie nanostructures is relatively low, and the tip-to-tip distance cannot be precisely controlled. Ding et al. proposed another strategy to prepare Au bowties using DNA origami (Figure 23D), which allows for placement of two binding sites at designated locations on DNA templates.[409] The Au nanotriangles functionalized with thiolated single-stranded DNA assemble onto such origami templates through DNA hybridization. The resulting Au bowties displayed an average gap distance of 5 ± 1 nm, resulting in remarkably high local field enhancement for single-molecule SERS measurements.

5. PROPERTIES AND APPLICATIONS

2D metal nanoparticles derived from the various synthetic strategies described above have fostered the study of their specific optical, mechanical, thermal, electrical, magnetic, and catalytic properties as well as related applications.[206] The properties of nanoplates are significantly influenced by the different constituent materials (monometallic, core−shell bimetallic, or alloys),[418] the thickness ranging from a few atomic layers to a few nanometers,[26,419] and the basal planes in triangular, square, hexagonal, or circular cross-sectional shape.[25,127] Extensive studies about these fundamental properties have led to a broad range of promising applications, some of which include biosensors,[420−422] optoelectronic devices,[423−425] mechanical nanoresonators,[426−429] and catalysis.[430−432] In this section, we begin with a detailed discussion about the plasmonic properties and applications of 2D metallic nanoparticles, following with highlights on recent advances in other fields, such as catalysis, mechanics, and magnetism, with a focus on those closely related to the characteristic 2D anisotropic structural features.

5.1. Plasmonics/Optics

5.1.1. LSPR Modes and Characterization. Localized surface plasmon resonances bring about light scattering and absorption, electromagnetic field enhancement at the nanoscale, photothermal effects, production of hot electrons, and photocatalytic activity. Understanding the LSPR modes is therefore essential for the development of plasmon-based applications.

It is well-established that LSPR frequencies strongly depend on the nanoparticle material and geometry. Au and Ag are the most widely studied plasmonic materials due to their highly tunable LSPR wavelength in the visible (vis) and near-infrared (NIR) or even mid-infrared region (MIR), and well-developed wet-chemical synthesis.[26] To date, other 2D plasmonic nanoparticles have been reported to support LSPR in the vis-NIR region (see section 3 of this review).[88,153,182,331,418,433−435] Langhammer et al. compared the LSPR peak position and line width of Au, Pt, and Al nanodisks, as a function of nanodisk diameter, both experimentally and through theoretical simulations (Figure 24A).[418,435] The observed pronounced differences in LSPR peak position and line width can be attributed to the bulk dielectric functions of different metals and the damping produced by different mechanisms (intraband damping, interband damping, radiation damping, and radiation quench-

https://doi.org/10.1021/acs.chemrev.3c00033
Chem. Rev. 2023, 123, 3493−3542

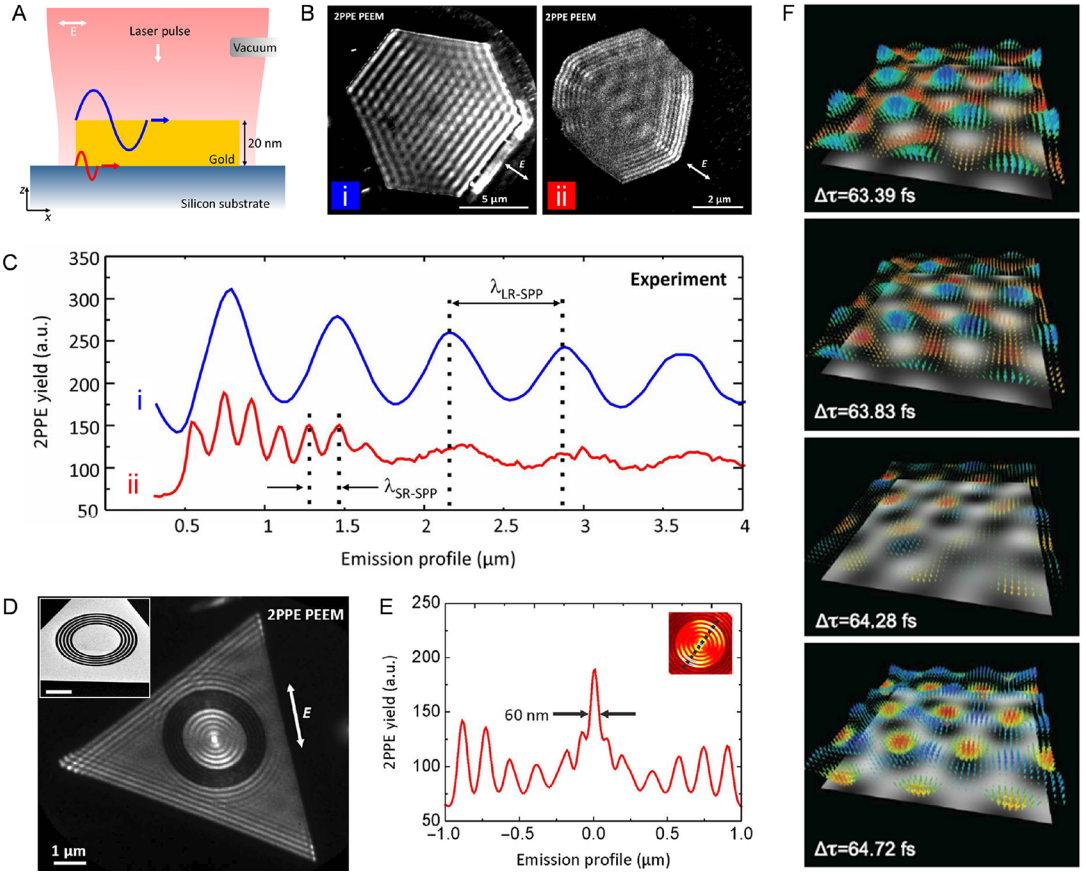

Figure 26. Surface plasmon polaritons supported by Au platelets. (A) Schematic diagram showing Au platelets deposited on silicon substrates. Long-range (LR) SPPs are indicated at the Au−vacuum interface (blue), and short-range (SR) SPPs are indicated at the Au−Si interface (red). (B) 2PPE PEEM images measured from a 120 nm thick Au platelet (i) and a 37 nm thick Au platelet (ii) at normal incidence. (C) PEEM emission profiles from the two platelets. Profile (i) shows LR- SPP pattern, whereas profile (ii) illustrates the superposition of LR-and SR-SPP. (D) 2PPE PEEM image of an Au platelet patterned with a circular grating of 150 nm period and a central disk with a diameter of 2 μm, under the excitation of 800 nm laser. Inset shows the SEM image. (E) Emission profile perpendicular to occurring wavefronts. (A−E) Reproduced with permission from ref 458. Copyright 2017 AAAS under CC BY 4.0 http://creativecommons.org/licenses/by/4.0/. (F) Time dependence of the SPP skyrmion lattice on an Au platelet with grooves for the excitation of SPPs. Reproduced with permission from ref 460. Copyright 2020 AAAS.

ing).[418] Notwithstanding, all three types of nanodisks exhibit a major LSPR peak that follows the well-known spectral red-shift with increasing nanodisk diameter (or aspect ratio), indicating that charge oscillations in different 2D metallic nanoparticles have a general commonality. Simulations have been performed to reveal the LSPR modes supported by 2D plasmonic nanoparticles and the impact of different geometrical parameters on the LSPR frequency, typically using Ag nanoplates as a model system.[436,437] Briefly, in-plane and out-of-plane LSPR modes are characteristic for 2D metallic nanoparticles due to their platelike morphology. The major LSPR peaks shown in Figure 24A(iv−vi) are associated with the in-plane dipolar mode, the corresponding charge oscillation being illustrated in Figure 24B(i).[436] The LSPR peak of the in-plane dipole mode is sensitive to several geometrical parameters, including edge length (or diameter), thickness, shape of the basal plane, and sharpness of the tips. Taking triangular Ag nanoplates as an example, the peak red-shifts with increasing edge length and blue-shifts with increasing truncation (Figure 24C).[437] Further experimental works, both on Au and Ag nanoplates, also reported a blue-shift of the dipole LSPR peak with increasing thickness[128,438] and rounded shape transformation (Figure 24D).[439,440] Notably, some spectra in Figure 24C,D display other LSPR resonances on the shorter-wavelength side, with weaker intensities than that of the in-plane dipolar mode. According to simulations, the peak at around 340 nm represents an out-of-plane quadrupolar mode (Figure 24B(iv)), whereas the out-of-plane dipolar mode (Figure 24B(ii)) and the in-plane quadrupolar mode (Figure 24B(iii)) both overlap, contributing to the broad shoulder at 400−500 nm.[436,437,441] Note that when nanoplates are sufficiently thin and high aspect ratio, out-of-plane modes exhibit extinction coefficients so low as to not be observed experimentally.[442,443]

Different techniques have been applied for the characterization of LSPR modes and understanding their near-field and far-field properties. Wang et al. carried out a series of experiments based on single-particle dark-field scattering to investigate the far-field scattering properties of individual Au nanoplates and oligomers,[439,441,444] as well as Fano resonances[445] and plasmon coupling based on nanoparticle-on-mirror (NPoM) systems.[446−449] In addition to the commonly seen horizontally oriented nanoplates, they successfully measured vertically oriented hexagonal Au nanoplates, where the quadrupolar LSPR mode could be excited and measured more efficiently than on the horizontally oriented ones (Figure 25A).[450] Because the higher-order LSPR modes are non-radiative (also known as "dark modes"), the accessibility of far-field excitation is very limited. On the contrary, near-field

https://doi.org/10.1021/acs.chemrev.3c00033
Chem. Rev. 2023, 123, 3493−3542

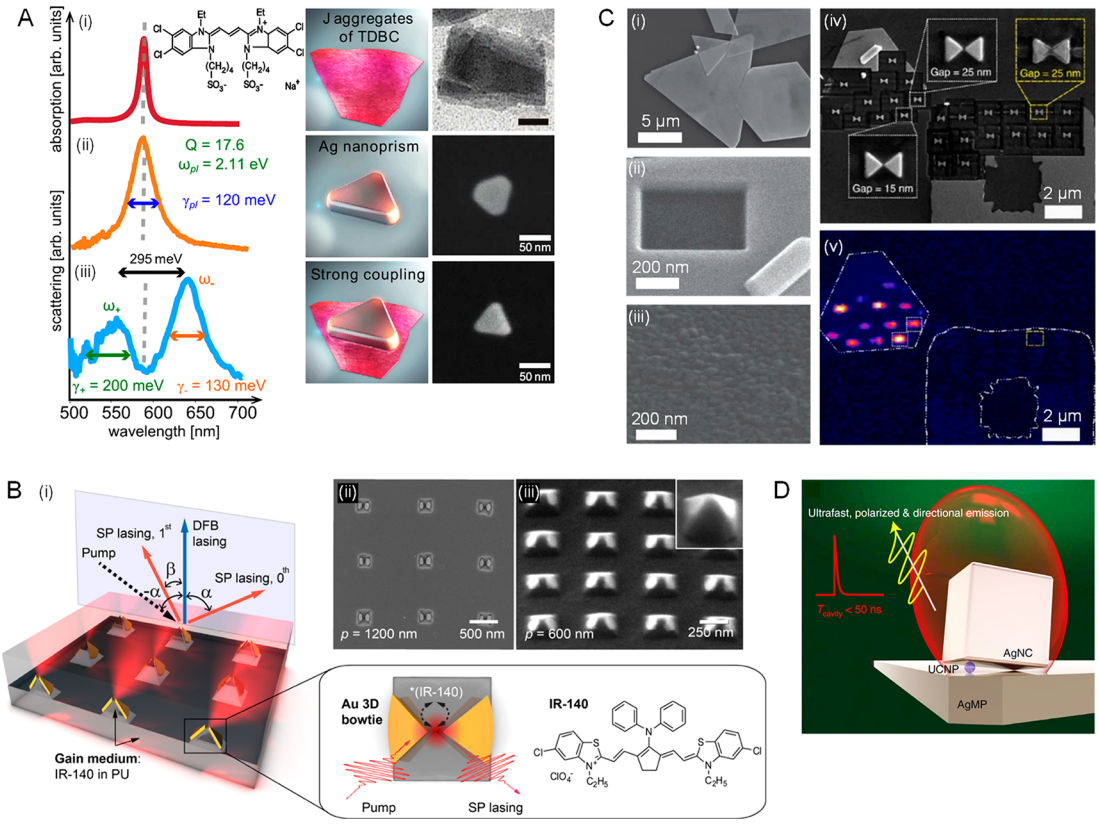

Figure 27. Light−matter interaction based on 2D plasmonic nanoparticles. (A) Strong coupling between single Ag nanoplate and molecular *J* aggregates at ambient conditions. (i) Extinction spectrum (in water), schematics, and cryo-TEM image of TDBC *J* aggregates. Inset shows the chemical structure of TDBC monomer. (ii) Scattering spectrum, schematics, and SEM image of the Ag nanoplate. (iii) Scattering spectrum, schematics, and SEM image of a single Ag nanoplate strongly coupled to *J* aggregates. Reproduced with permission from ref 462. Copyright 2015 American Institute of Physics. (B) Plasmonic nanolasers based on 3D-bowtie nanoarray. (i) Schematic diagram of the 3D-bowtie array with IR-140 dye as gain materials. (ii,iii) SEM images of 3D-bowtie array with period of 1200 nm (ii) and 600 nm (iii), respectively. Reproduced with permission from ref 423. Copyright 2012 American Chemical Society. (C) Comparison between chemically synthesized Au flakes and vapor-deposited Au film. (i−iii) SEM images of the chemically synthesized Au flakes (i), smooth surface of a crystalline Au flake with the rectangular area milled by FIB (ii), rough surface of a vapor-deposited Au film (iii). (iv) SEM image of bowtie antennas fabricated by FIB on a crystalline Au flake (left) and vapor deposition (right). (v) TPPL map of the same area shown in (iv). Reproduced with permission from ref 466. Copyright 2010 Springer Nature. (D) Tilted-nanocavity-coupled system comprising an upconverting nanoparticle embedded in the nanogap between an Ag nanocube (AgNC) and an Ag microplate (AgMP). Reproduced with permission from ref 483. Copyright 2022 Springer Nature.

microscopic techniques, such as scanning near-field optical microscopy (SNOM),[451−453] scanning transmission electron microscopy with EELS,[454,455] and CL spectroscopy, can excite the LSPR modes locally and therefore can be used to characterize higher-order LSPR modes. The pioneering work by Stéphan et al. opened the possibility of LSPR visualization at high spatial resolution by STEM-EELS measurements, where different LSPR modes of a triangular Ag nanoplate can be selectively excited by a subnanometer electron beam (Figure 25B).[454] Imura et al. demonstrated by 3D SNOM measurements that the in-plane and out-of-plane LSPR modes can be selectively visualized by varying the distance between the probe tip and the Au nanoplate, even though the two LSPR modes were spectrally and spatially overlapping (Figure 25C).[451,456] However, the near-field distributions of plasmonic nanoplates measured by different groups or with different techniques are always slightly different, especially in terms of the higher-order modes. It is therefore challenging to accurately compare the results among different literature reports due to the difficulty in estimating the effect of experimental details on the results. In this regard, Kociak et al. combined EELS and CL measurements to investigate the exact same individual Au nanoplates to provide a fair comparison of the two techniques.[457] They thereby demonstrated that both techniques can detect the dipolar mode with good agreement, but the higher-order modes are accessible only by EELS (Figure 25D). Likewise, rigorous comparison between other near-field and far-field techniques is highly desired for better interpretation of the experimental results obtained from different techniques.

Besides LSPR modes, micrometer-scale plasmonic platelets can support propagating surface plasmon polaritons (SPP), resembling those supported by plasmonic thin films. Imaging of SPPs on Au platelets was recently reported using time-resolved two-photon photoemission electron microscopy (TR-2PPE-PEEM), where electron emission can be triggered optically.[458−461] Meyer zu Heringdorf and Giessen et al. reported the detection of short-range and long-range SPPs (SR-SPP and LR-SPP) at the Si−Au interface and Au−vacuum interface for Au platelets deposited on Si substrates (Figure 26A,B).[458] SR-SPPs exhibit significantly shorter wavelength than LR-SPPs and decay quickly with propagation (Figure 26C). However, when the Au platelets are thin enough (∼22 nm) and patterned with a concentric grating (inset of Figure 26D), the SR-SPPs can couple into a central disk, leading to localized two-photon

https://doi.org/10.1021/acs.chemrev.3c00033
Chem. Rev. 2023, 123, 3493−3542

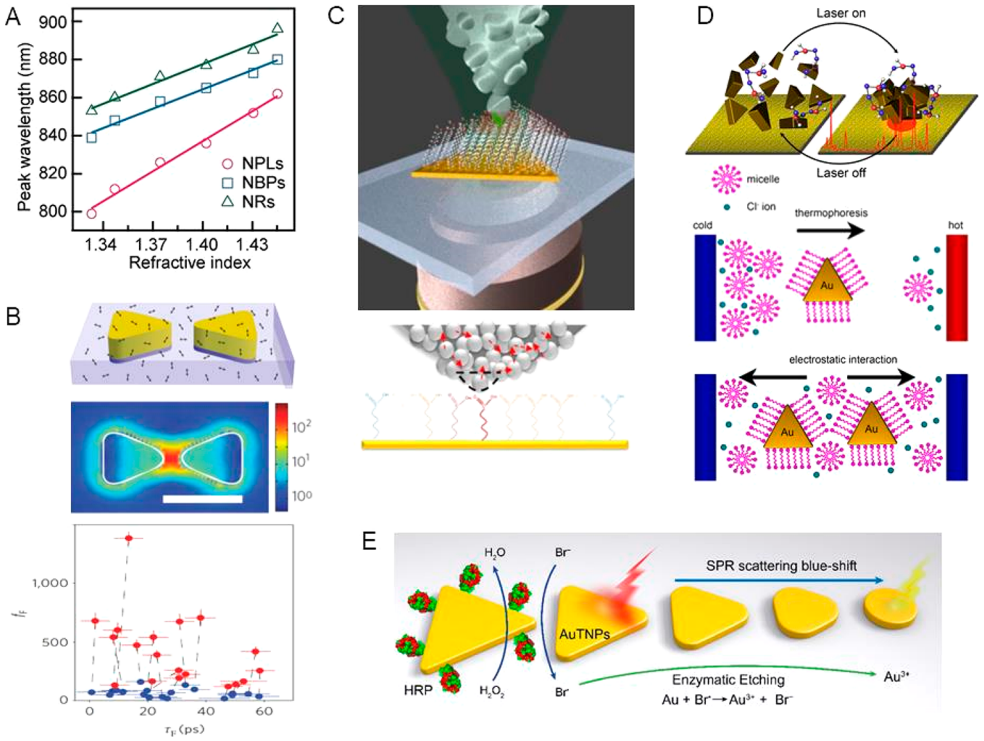

Figure 28. Sensing based on 2D plasmonic nanoparticles. (A) Dependence of the dipolar LSPR wavelengths on the refractive index for Au nanoplates, nanorods, and bipyramids. Reproduced with permission from ref 128. Copyright 2016 Wiley-VCH. (B) Schematic diagram, simulated electric field profile, and fluorescence enhancement factor of Au bowtie nanoantenna. The red and blue dots denote excitation light polarized parallel/perpendicular to the long axis of the bowtie. The black dashed lines connect results measured from the same molecule. Reproduced with permission from ref 420. Copyright 2009 Springer Nature. (C) Schematic diagram of a TERS setup. Light is focused at the apex of an Ag-coated TERS tip approaching the Au nanoplate surface, functionalized by a self-assembled molecular monolayer. Reproduced with permission from ref 489. Copyright 2020 Springer Nature under CC BY 4.0 http://creativecommons.org/licenses/by/4.0/. (D) Schematic illustration of light-directed reversible assembly of Au nanoplates, and their release or redispersion due to plasmon-enhanced thermophoresis and electrostatic repulsive interaction. Reproduced with permission from ref 490. Copyright 2016 American Chemical Society. (E) Schematic diagram of a plasmonic biosensor based on enzymatic etching on triangular Au nanoplates in the presence of H_2O_2. Reproduced with permission from ref 491. Copyright 2020 Springer.

ultrafast electron emission from a 60 nm spot (Figure 26E). They further applied this technique to image the plasmonic skyrmion lattice (Figure 26F), where the SPPs were detected by interference with a probe pulse.[460] These intriguing plasmonic properties will create new opportunities in nanophotonic applications.

5.1.2. Spectroscopies. The unique plasmonic features of 2D metallic nanoparticles have been exploited in various light–matter interactions including the use of plasmonic nanoplates as individual optical nanocavities,[462−465] atomically flat substrates,[447,466,467] or components of bowtie nanostructures in a tip-to-tip configuration.[423,468−471] Plasmon–exciton coupling has been demonstrated by several groups using Au or Ag nanoplates as the plasmonic platform and other 2D fluorescent materials, such as *J*-aggregate sheets and 2D transition metal dichalcogenides (TMDCs), as the exciton provider.[462−465] The flat surface allows the plasmonic nanoparticles to adhere to these 2D fluorescent materials over a large contact area and thereby interact with them efficiently. Under a relatively low coupling strength, the plasmon–exciton system exhibits Fano resonances, where the eigenenergies of the system are actually degenerate.[465] By varying the dimension and composition of the nanoplates, the lower plasmon damping and concomitant narrower plasmon line width can drive the system into the strong coupling regime, as evidenced by the splitting in the eigen energies known as Rabi splitting (Figure 27A).[462−464] In general, plasmonic nanoplates with small mode volumes are favorable for achieving strong coupling.

Bowtie nanostructures consisting of two tip-to-tip plasmonic nanotriangles with a gap size less than tens of nanometers, as first proposed by Moerner et al.,[471] are an ideal platform to concentrate large electric fields into an ultrasmall volume. Taking advantage of the ultrastrong plasmonic hot spots, this design has been widely applied to facilitate the development of sensors,[420] optical tweezers,[470,472] high-harmonic generation,[473,474] surface-enhanced Raman scattering,[475] and nanophotonic devices.[425,476] Odom et al. further proposed a 3D-bowtie nanostructure, in which the Au nanoplates were folded along the dimer axis, giving rise to a higher excitation efficiency of the quadrupolar LSPR mode, compared to that of the planar 2D-bowtie nanostructure. They successfully developed room-temperature directional nanolasers by fabricating these 3D-bowtie arrays on dye-doped polymer slabs (Figure 27B).[423,469] In the aforementioned works, the bowtie nanostructures were all made by top-down nanofabrication techniques, such as electron beam lithography (EBL), due to the need to precisely control the orientation and position of the plasmonic triangles, which seems less relevant to the chemically prepared nanoparticles discussed in this review. However, such bowtie nanostructures and arrays can also be fabricated by applying focused ion beam (FIB) milling on large chemically grown Au nanoplates, as proved by Hecht et al. (Figure 27C).[466] Compared to the EBL-fabricated Au bowtie nanostructures, those fabricated by FIB

https://doi.org/10.1021/acs.chemrev.3c00033
Chem. Rev. 2023, 123, 3493−3542

possess an ultrasmooth surface and well-defined crystalline structure, leading to superior optical performance as evidenced by the much brighter two-photon excited photoluminescence (TPPL) signals (Figure 27C(v)). This technique can be extended to other complex nanostructures with improved optical performance compared with the EBL-fabricated ones, suggesting great potential for chemically prepared 2D plasmonic nanoparticles to be used in plasmonic nanocircuits.

NPoM systems are another popular configuration for studying light−matter interactions, where the nanoplates can either serve as the "nanoparticle" or the "mirror", leading to a highly confined flat gap, i.e., an ideal optical nanocavity.[477−479] When serving as the "nanoparticle", the plasmonic nanoplates are usually deposited on an evaporated metal thin film with other optical species introduced in the flat nanogap, where plasmons can modify the spontaneous emission strength, fluorescence spectrum, decay rate, and radiation pattern of these optical species.[480] This configuration is specifically beneficial for achieving strong coupling between plasmonic nanoparticles and TMDCs, due to the ultrastrong field enhancement in the nanogap and the overall small mode volume. Qiu et al. demonstrated strong coupling by a sandwiched Au−WS_2−Au system composed by chemically prepared Au nanoprisms and WS_2 monolayers supported by Au thin films, giving rise to strong coupling approaching the single-exciton level with a large vacuum Rabi splitting of up to 163 meV.[481] Through precise control over the spacing between the two Au surfaces, different orders of Fabry−Pérot resonances can be supported within the optical cavity, offering more optical modes for modulating photoluminescence of the sandwiched WS_2.[482] Furthermore, the plasmonic nanoplates can also serve as an atomically flat "mirror" of NPoM systems. For example, Wang et al. used Au nanoplates as the basis of a NPoM system to demonstrate different charge tunneling behaviors of insulating and conductive molecular junctions, as evidenced through the single-particle scattering spectra of the plasmonic heterodimers.[467] In another recent example, Xu et al. embedded single up-conversion nanoparticles in the nanogap of a tilted-nanocavity-coupled system using Ag microplates as substrates (Figure 27D), which enabled sub-50 ns ultrafast upconversion luminescence with directionality and chirality.[483] Because these systems are extremely sensitive to the nanometer gaps, atomically flat plasmonic nano- and microplates are highly desired for eliminating the perturbative effects from the rough surfaces of conventional metal thin films. Similar systems can be further extended to study photoluminescence, photocatalysis, SERS, and coherent nonlinear processes.[484]

5.1.3. Sensing. Plasmonic nanoplates have been widely used for sensing through refractive index changes,[128,485−488] molecular sensing based on surface-enhanced spectroscopies,[420,489,490] and colorimetric sensing based on etching.[491,492] Plasmonic nanoplates may play the role of optical nanoantenna, substrate, or colorimetric reagent, depending on the detection strategy.

LSPR is strongly responsive to changes in the refractive index of the surrounding medium, including solvent and surface binding molecules. The refractive index sensitivity is dependent on the size, shape, composition, and specific LSPR mode of the plasmonic nanoparticles.[493] A few works from different groups have shown that the in-plane dipolar plasmon mode of Au and Ag nanoplates exhibits excellent refractive index sensitivities 400−1000 nm/RIU (refractive index unit), with figures of merit above 3 at different wavelengths in the vis-NIR region.[128,485−488] These values are on average higher than those for other plasmonic nanoparticles (Figure 28A).[128,494] The high refractive index sensitivity can be attributed to the 2D geometry with a high aspect ratio and therefore a high ratio of surface area to bulk atoms of nanoplates, resulting in a larger impact of the dielectric environment on the charge oscillation of LSPR.[487,493]

Although surface ligand detection is also possible through refractive index sensing,[486] plasmonic nanoplates are much more commonly used for ultrasensitive molecular detection through surface-enhanced spectroscopies, such as plasmon-enhanced fluorescence,[420] SERS,[409,475,490] tip-enhanced Raman spectroscopy (TERS),[489] and surface-enhanced infrared absorption (SEIRA).[495] In this sort of plasmonic sensor, triangular nanoplates are beneficial due to their sharp tips and intense local field enhancement.[493] In the pioneering work by Moerner et al., the authors utilized lithographically fabricated Au bowtie nanoantennas to achieve large single-molecule fluorescence enhancements (Figure 28B). Under excitation light polarized parallel to the long axis of the bowtie antenna, the electric field enhancement at the gap area could reach more than 100-fold and thereby the fluorescence brightness would be enhanced up to 1340-fold.[420] Similarly, lithographically fabricated bowtie nanostructures were demonstrated for SERS with enhancement factors exceeding 10^{11}, and for SEIRA with enhancement factors higher than 10^{7}.[475,495] Ding et al. constructed Au bowties by DNA-origami-directed assembly (see section 4) of chemically prepared triangular nanoplates and demonstrated single-molecule SERS of individual nanostructures.[409] Apart from the well-established bowtie nanostructures, hot spots can be generated in other configurations for molecular detection. Richard-Lacroix and Deckert covered atomically flat plasmonic nanoplates with a self-assembled monolayer of 16-mercaptohexadodecanoic acid and used them as a platform for TERS (Figure 28C). Taking advantage of the tightly confined light between the Ag-coated TERS tip and Au nanoplates, only the molecules located directly under the TERS tip can actually contribute to the anti-Stokes/Stokes Raman signals, allowing for an accurate evaluation of the local heating of the molecules.[489] In work by Zheng et al., hot spots were generated for the SERS detection of rhodamine 6G by light-directed reversible assembly of Au nanoplates based on plasmon-enhanced thermophoresis (Figure 28D).[490] Other self-assembly strategies, as mentioned in section 4, can be adopted for generating compact assemblies and improving the sensing performance of plasmonic nanoplates.

Colorimetric sensing based on etching is another popular sensing approach based on plasmonic nanoplates, especially for their application of biosensing.[491,492,496] It is well-known that Au and Ag nanoplates can be directly etched by highly oxidative analytes, such as H_2O_2, As^{5+}, Cr^{6+}, ClO^-, and NO^{2-},[497] giving rise to morphological changes and thereby color changes readable by the naked eye without any expensive or sophisticated instrumentation. However, using H_2O_2 as an example, it typically requires high concentration (~mM) and high reaction temperature (~60 °C) to rapidly etch Au nanoparticles, which limits the applicability for biosensing purposes. An alternative strategy is to introduce another species to control the etching process, which may allow for more sensitive detection. Figure 28E shows a typical reaction pathway for the detection of trace H_2O_2 in live cells using triangular Au nanoplates functionalized by horseradish peroxidase (HRP), which can etch the Au nanoplates under mild conditions by the strong coordination of Br^- generated by a biocatalytic enzymatic reaction.[491,498] On the contrary, it was found that a small

https://doi.org/10.1021/acs.chemrev.3c00033
Chem. Rev. 2023, 123, 3493−3542

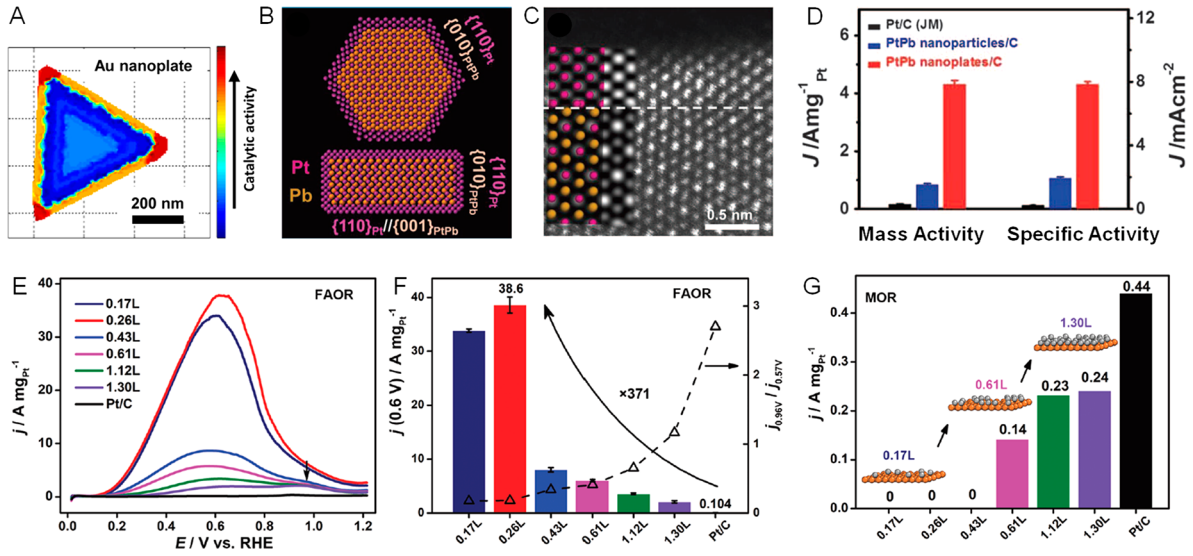

Figure 29. Catalysis. (A) Mapping of specific catalytic activity correlated with the SEM image of a single Au@SiO_2 nanoplate. Reproduced with permission from ref 503. Copyright 2013 American Chemical Society. (B) The schematic atom models of the PtPb@Pt core−shell nanoplate viewed from the top and the side interface. (C) High-resolution HAADF image at the edge of the PtPb@Pt core−shell nanoplates, together with the overlapped schematic atom model. (D) Mass and specific activities of PtPb nanoplates/C, PtPb nanoparticles/C, and commercial Pt/C catalysts. Reproduced with permission from ref 430. Copyright 2016 AAAS. (E) Catalytic FAOR activities of the Ag@Au@Pt nanoplates measured by cyclic voltammetry in 0.5 m H_2SO_4 + 0.25 m HCOOH. (F) Mass activities of the catalysts in the FAOR (left axis) and degree of CO poisoning in the FAOR (right axis). (G) Mass activities of Pt ensembles with 3−4 contiguous Pt atoms in the methanol oxidation reaction (MOR). Reproduced with permission from ref 432. Copyright 2022 Wiley-VCH

amount of uric acid binding to the Ag nanoplates can prevent them from etching, resulting in a high detection limit down to only 10 nM.[496] Thanks to their relatively low stability and outstanding colorimetric properties, Au and Ag nanoplates have been used in a variety of colorimetric sensing protocols.[497,499]

5.2. Catalysis

Nanoparticles composed of Au, Ag, Cu, and group VIII elements (such as Pt, Pd, Ru, Rh, Ni, and Co) have been extensively investigated for heterogeneous catalysis (see section 3). Because the interior bulk atoms usually play a negligible role in this process, a simple yet effective way to improve the performance of a catalyst is to decrease the nanoparticle size and therefore increase the surface-to-volume ratio.[500] Compared to other shapes that metal nanoparticles can adopt, nanoplates and platelets possess extremely high surface to volume ratios, abundant low-coordinated atoms at their perimeters, and relatively high surface energy, which are all known to be beneficial for boosting catalytic activity and selectivity in various applications, such fuel cells, metal−air batteries, water splitting, and CO_2 reduction.[206,501] Different reactions have been extensively explored with various 2D metallic catalysts, including monometallic nanoplates,[172,502,503] bimetallic/multimetallic core−shell nanoplates,[430,432,504,505] alloy nanoplates,[431,506,507] and sheet-like structures with thicknesses of single or few atomic layers,[501] as well as their deposition on oxides.[508,509] Because different catalysis mechanisms of metallic nanoparticles have been the subject of numerous reviews, we herein only focus on the findings directly correlated with their 2D features.[510−513]

In general, nanoplate catalytic activity can be effectively enhanced by reducing the thickness, which increases the surface to volume ratio and number of active sites. Yang et al. compared the catalytic activity among Au nanoplates with lateral dimensions varying from 15 to 50 nm and found decreasing catalytic activity with increasing thickness.[514] The high catalytic activity was also affected by the rougher surface so that more active sites were obtained on the thinner nanoplates with their synthetic method. Similarly, superior catalytic performance was found from atomically thin Au platelets containing 1−2 atomic layers and exposed catalytically active sites.[515,516] Chen et al. applied super-resolution single-molecule catalysis imaging to differentiate reactivity at the corner, edge, and facet regions on single Au@SiO_2 nanoplates, whose large top and bottom flat surfaces were identified as {111} facets and the edges as {111} or {110}.[503] They observed a trend of site-specific activity following corner regions > edge regions > flat surface facet regions (Figure 29A), as well as a shallower radial gradient from the center to the edges within the flat {111} facets, which was interpreted in terms of the coordinative undersaturation at corners, edges, and defect sites on the flat surfaces, respectively. In this study, they also observed that the specific catalytic activity of all three regions increased with increasing nanoplate size. In 2015, Xu et al. mapped the reactivity patterns on bare Au nanoplates without a SiO_2 shell using the same catalysis reduction reaction. On the contrary to the previous work, they observed greater catalytic activity from the flat surface facet regions than the edges and corners, whereas the gradient in flat surface was consistent with the previous work.[517]

Bimetallic and multimetallic catalysts allow for the regulation of catalytic properties, chemical stability, optical properties, and biocompatibility, through rational design of elemental composition and architecture. Much effort has been made on core−shell nanostructures and alloying of noble metals, especially Pt and Pd, in order to increase their activity, efficiency, and stability in catalysis and electrochemical applications.[518] Specifically, the 2D morphology allows for engineering surface strains, surface lattice, and entropy so as to enhance the activity of catalysts. Huang et al. reported PtPb@Pt core−shell hexagonal nanoplates with a PtPb core in a highly crystalline intermetallic phase and Pt shell in a cubic phase at the edge but a hexagonal phase in the interior (Figure 29B,C). According to density functional

https://doi.org/10.1021/acs.chemrev.3c00033
Chem. Rev. 2023, 123, 3493−3542

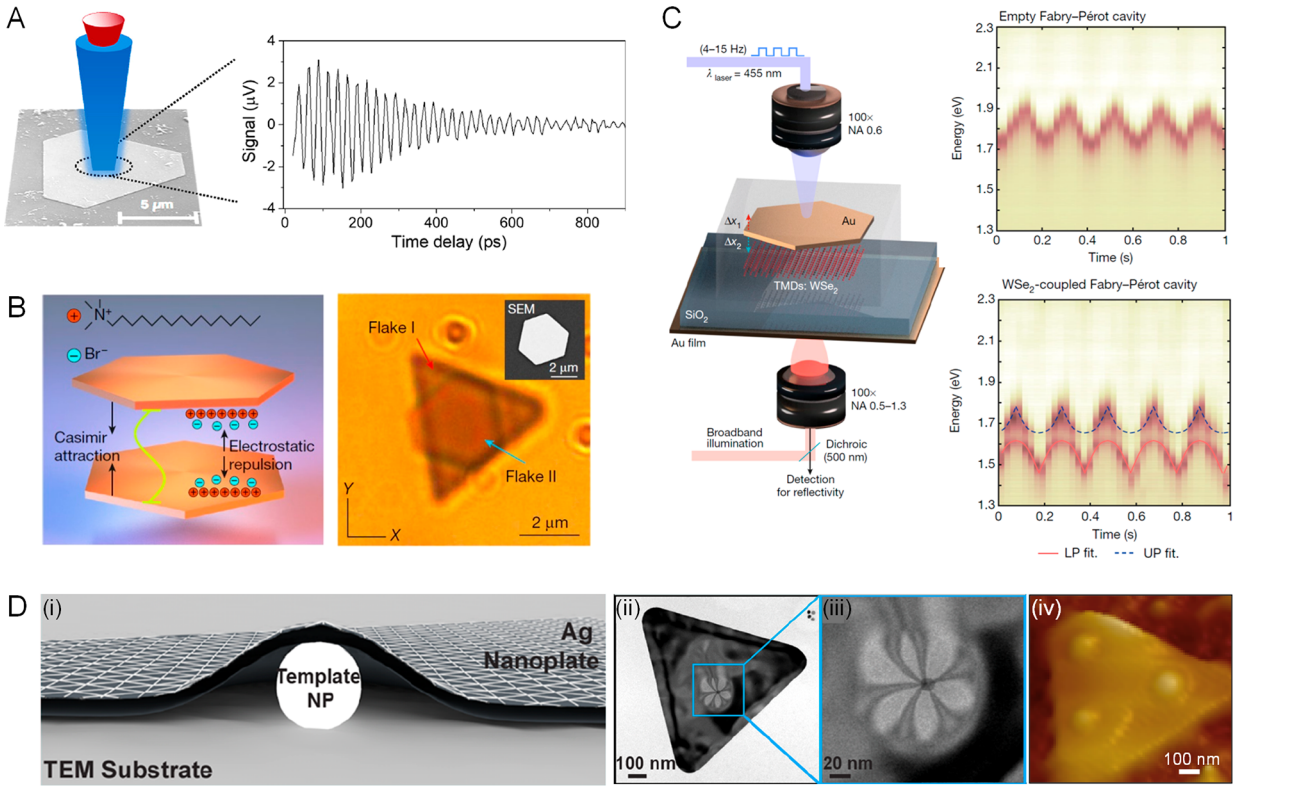

Figure 30. Mechanical properties of 2D plasmonic nanoparticles. (A) Single-particle pump−probe spectroscopy for the measurement of acoustic vibrations. Reproduced with permission from ref 426. Copyright 2017 American Chemical Society. (B) Illustration, optical image, and SEM image of the self-assembled optical cavity consisting of two Au nanoplates. (C) Schematic of the experimental setup (left) for active tuning of the empty cavity and plasmon−exciton coupling system, and the resulting time-resolved reflection spectra (right). Reproduced with permission from ref 428. Copyright 2021 Springer Nature. (D) Local deformation of nanoplates via van der Waals interactions. (i) Illustration showing the local deformation of Ag nanoplates over a spherical template nanoparticle. (ii,iii) Representative TEM images showing the bend contour patterns of deformed Ag nanoplates. (iv) AFM topographical map of a deformed Ag nanoplate. Reproduced with permission from ref 18. Copyright 2021 American Chemical Society.

theory (DFT) calculations, such a structure leads to large tensile strains at the edge and the top/bottom {110} facets of Pt, which help increase the Pt−O bond strength and thereby boost the efficiency of the oxygen reduction reaction (ORR) (Figure 29D).[430] More recently, Huang et al. successfully constructed a class of unique PtBiPbNiCo-alloyed hexagonal nanoplates with medium-entropy core and high-entropy atomic layer shell, giving rise to outstanding performance toward the formic acid oxidation reaction (FAOR).[506]

Recent advances in synthesis allow for modulating catalytic performance at the atomic level.[500] Atomically flat nanoplates are ideal substrates for the precise study of single-atom catalysis, owing to their well-defined crystalline facets that simplify the growth environment of the single-atom catalysts.[431,432,519] Gao et al. developed a ligand-mediated self-terminating strategy to realize a progressive growth of Pt single atoms, ensembles, and eventually a full monolayer of Pt on Ag@Au nanoplates, enabling the formation of isolated Pt single atoms up to 26% coverage.[432] The resulting Ag@Au@Pt nanoplates with rich Pt single atoms show record-high catalytic activities in the electrocatalytic FAOR without involving poisoning of CO intermediates (Figure 29E,F). The single-atom feature was further verified by the methanol oxidation reaction (MOR), which is another ensemble-size-sensitive reaction occurring mainly at clusters of 3−4 contiguous Pt atoms (Figure 29G). Quan et al. developed an atomic galvanic replacement strategy to generate isolated Rh atoms on PtBi nanoplates, and subsequent electrochemical transformation into a tensile-strained alloy consisting of atomic *fcc*-Pt layers and Rh single atoms, which remarkably boosts the ethanol oxidation reaction (EOR).[431] Very recently, Cui et al. introduced single-atomic Ir sites on the surface of *hcp*-PtPb/*fcc*-Pt core−shell nanoplates to tune the selectivity and activity of EOR, offering another strategy for tuning the activity and selectivity toward other electrocatalytic reactions.[519]

5.3. Magnetism

Nanoplates based on ferromagnetic materials, such as Fe, Co, Ni, and certain rare-earth metals, typically exhibit magnetic anisotropy derived from particle shape anisotropy.[239,240] Magnetic anisotropy can be estimated by the formula: $K = 25k_BT_BV^{-1}$, where k_B is the Boltzmann constant, T_B is the blocking temperature at which the coercivity completely vanishes, and V is the volume of a single particle. So far, there are only a few reports about metallic magnetic nanoplates, probably due to the lack of synthetic protocols. Takahashi et al. demonstrated the preparation of Ni nanoplates with typical ferromagnetic behaviors at room temperature and a magnetic anisotropy value of $\sim 12.6 \times 10^5$ erg cm^{-3}, which is over 10 times higher than that of bulk Ni $\sim 5 \times 10^4$ erg cm^{-3}.[239] Once exposed to an alternating magnetic field, Ni nanoparticles can serve as localized heat mediators for magnetic hyperthermia and magnetically induced catalysis. In the heating power measurements performed by Lacroix et al., the specific absorption rate of Ni nanoplates is among the highest compared with differently shaped Ni nanoparticles upon an alternating magnetic field.[520]

https://doi.org/10.1021/acs.chemrev.3c00033
Chem. Rev. 2023, 123, 3493−3542

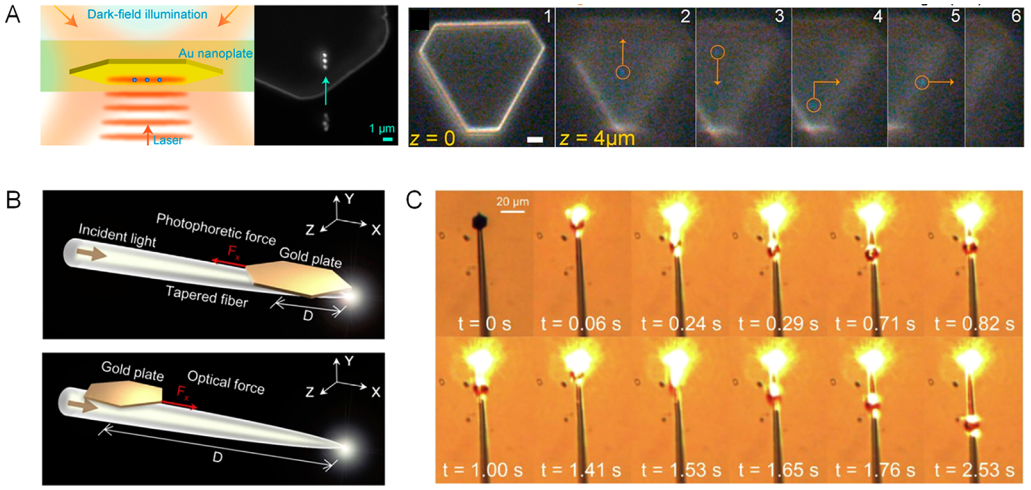

Figure 31. Optical trapping based on 2D plasmonic nanoparticles. (A) Schematic and experimental results of optical trapping of a 30 nm Ag nanoparticle with the interferometric optical tweezers. Reproduced with permission from ref 525. Copyright 2014 American Chemical Society. (B) Schematic of pulling and pushing a hexagonal Au plate on a tapered fiber. (C) Experimental optical images showing a back-and-forth movement of a single Au nanoplates on a tapered fiber. Reproduced with permission from ref 526. Copyright 2017 American Institute of Physics.

Peng et al. demonstrated tunable magnetic properties of Ni−Cu alloy nanoplates by adjusting the Ni content.[240] They further compared the hexagonal and triangular Ni−Cu nanoplates in terms of transition from the ferromagnetic to the superparamagnetic state with increasing temperature, and found that the former can undergo the transition more easily than the latter. NiCo alloyed nanoplates have been synthesized but used for catalysis rather than for their magnetic properties.[521]

5.4. Mechanics

The small thickness and large in-plane lateral dimensions endow nanoplates with fascinating mechanical properties, especially when they interact with light. Several groups have reported the observation of GHz frequency wave vibrations of metallic nanoplates along the thickness dimension, which are known as acoustic vibrations or the breathing phonon mode of the nanoplates, typically along the thickness dimension.[427,522−524] These vibrations can be triggered and measured by a two-color femtosecond pump−probe system, where the nanoplates are excited by the pump pulses to generate heat or hot electrons that trigger acoustic lattice vibrations, leading to small changes in the optical transmission or reflectivity on a time scale of picosecond that can be monitored by the probe pulse (Figure 30A). The vibration frequency, which can be identified by fast Fourier transform (FFT), depends on the probe wavelength,[426] size and shape of the nanoplates,[522] supporting substrates,[523] viscous and viscoelastic properties of the surrounding medium,[427] and mechanical coupling between nanoplates.[429] The mechanical coupling between nanoplates can involve more microscopic interactions. Shegai et al. recently reported the joint interaction of attractive Casimir and repulsive electrostatic forces of a Fabry−Pérot cavity self-assembled by two charged Au nanoplates in an aqueous solution (Figure 30B).[428] The optical response of the cavity is actively tunable by modulating the vertical position of the floating nanoplates with a periodically varied control laser (Figure 30C). They further applied this technique to control the plasmon−exciton coupling between the optical cavity and WSe_2 monolayer to move in and out of the strong coupling regime. Although most studies have described the mechanical properties of nanoplates in terms of rigid structures, recent work by Jones et al. has shown that the nanoplate morphology, with large basal planes and small thickness, can be extremely flexible, to the point that relatively weak forces cause it to deform plastically (permanently).[18] The authors show that high-aspect-ratio Ag nanoplates can be draped over spherical particles deposited on a surface because the substrate−nanoplate attractive vdW energy is comparable to the strain energy required to deform the particle. This particle-oversphere "mound" structure produces unusual bend contour patterns in TEM images (Figure 30D), the size of which can be used to extract the mechanical properties of the particle. This result highlights future capabilities for designing unique curvilinear nanoparticle morphologies that would be challenging to fabricate by either nanolithographic or colloidal synthetic approaches.

Another aspect of the mechanical properties of metallic nanoplates is their capability to trap or move target objects by optical forces. Scherer et al. utilized Au nanoplates as a micrometer-size mirror to achieve an optical tweezer through the interference between the incident laser beam and its reflection from the Au nanoplates. The enhanced optical trapping and binding force enabled excellent trapping stability for manipulating single Ag nanoparticles with small diameter of ∼30 nm (Figure 31A).[525] Moreover, Qiu et al. experimentally realized light-induced pulling and pushing of a micrometer-size Au nanoplate back and forth on a tapered fiber Figure 31B.[526] A photophoretic pulling force can be introduced by the large temperature difference when the Au nanoplate is close to the tapered fiber end. On the contrary, the optical forces coming from light scattering mainly acts as a pushing force along the tapered fiber. As a result, nanoplates can be optically driven back and forth with a speed up to 28 μm/s (Figure 31C).

6. SUMMARY AND PROSPECTS

Metal nanoplates offer various unique features that are not found in other nanosized objects. The planar morphology leads to the presence of two well-defined, extended facets, which are usually parallel to each other and share the same crystallographic indices. As a result, the crystallographic structure of the whole object imposes specific restrictions. For example, in the case of *fcc* metals, a nanoplate morphology requires the presence of stacking faults or twin planes (also parallel to the larger

https://doi.org/10.1021/acs.chemrev.3c00033
Chem. Rev. 2023, 123, 3493−3542

boundary facets). From a careful analysis of such crystallographic peculiarities, it has been possible to propose growth mechanisms that can be used to guide further design of synthesis methods, aiming at a tight control over geometry and dimensions. Although growth methods/mechanisms often rely on chemical parameters, such as selective binding of ligands/additives on certain facets, the presence of localized surface plasmon resonances in (noble) metallic nanoparticles offers an additional handle to direct anisotropic growth. The excitation of so-called in-plane LSPR modes has been used in some of the earliest examples of controlled metal nanoplate growth, leading to wavelength-directed selection of the achieved morphology and dimensions. More recently, the same concept has been applied to grow metal nanoplates with morphological and optical chirality, through illumination with circularly polarized light. Again, the well-defined planar morphology, in particular when including sharp tips, allows a simpler prediction of the expected outcome and the concept may readily be expanded to other morphologies.

On the other hand, metal nanoplates also offer a rich playground to serve as templates for postsynthesis transformations, either through overgrowth with the same or a different (metallic) material or through etching/galvanic replacement. Ultimately, the variety of structures and compositions that can be obtained through chemical modification of metal nanoplates is extremely broad and offers the possibility to further manipulate the chemical and physical properties of the resulting (nano)materials. Similarly, self-assembly of these largely anisotropic nano-objects can result in nanostructures with a high degree of order and tunable interparticle spacing, thereby encompassing extremely appealing properties.

However, research on metal nanoplates has not been restricted to the most characteristic noble metals (Au and Ag), but examples have been reported (and summarized in section 3 of this review) for a high proportion of the metals available in the periodic table. Working with different metals, commonly displaying a lower chemical stability than Au and Ag, poses additional synthetic challenges and thus requires the implementation of special strategies and the use of different capping ligands. It is important to stress that some of these metals grow in crystallographic lattices different to *fcc*, such as *hcp* or *bcc*, which involve different relative surface energies and thus different growth rates, which can be exploited to simplify the synthetic strategies.

The availability of a wide variety of metal nanoplates also leads to a wide range of properties and related applications. From optics/plasmonics through magnetism, catalysis, mechanical strength, sensing, and different therapeutic modalities, metal nanoplates have been reported to feature efficient responses. Particularly interesting is the possibility of using the nanoplate morphology as a model system for evaluation of novel physical effects or applications. An obvious example would be the detection of plasmon modes by electron energy loss spectroscopy, but it could also be the identification of particularly active facets for catalysis, anisotropic mechanical responses, or simply by offering atomically flat surfaces for scanning probe spectroscopies or deposition of self-assembled monolayers.

When reviewing the (extensive) existing literature on all these aspects of metal nanoplates, we found a distinct lack of cross-correlation among various synthetic efforts, meaning that the mechanisms, chemical reactions, binding ligands, and even environmental conditions are rarely compared to each other. Even though the quality and tunability of many such methods may be extremely high, we identify a missed opportunity to draw a set of general trends that can be jointly exploited to further improve the quality and reproducibility of the various methods as well as to further expand the library of metal nanoplates.

A closely related deficiency lies in the lack of modeling tools that can be reliably used to simulate and ultimately predict the outcome of a specific type of synthesis under a specified set of conditions. Methods such as density functional theory (DFT) can provide information on the surface energies and how they change upon adsorption of (facet selective) ligands. Molecular dynamics (MD) simulations can even predict the packing density and arrangement of such ligands on arbitrary crystalline facets and compositions. However, the size of the simulated systems is still relatively small, so it is hard to achieve simulations on entire particle−ligand systems in the usual size scale for nanoplates (tens or hundreds of nm). Additionally, such theoretical methods are still limited regarding the number of parameters that can be considered. A suitable simulation should include both thermodynamic and kinetic aspects of the chemical reactions, the crystallography and dimensions, as well as the diffusion dynamics of particles growing in solution. Recent developments in the application of artificial intelligence (AI) methods, machine learning (ML) in particular, to the prediction of materials synthesis, offer a great opportunity to resolve some of the above referred limitations of current computational methods. In fact, if the available literature data could be collected in a publicly accessible repository, they could already be used as inputs for training ML algorithms and save a huge amount of experimental work.

The recent progress in advanced electron microscopy tools, including atomic resolution electron tomography and the use of liquid cell sample holders, has already opened the way toward time-resolved monitoring of growth processes with atomic resolution. There is no doubt that the signal-to-noise ratio in such experiments will be rapidly improved, so that even the most obscure details such as the symmetry breaking events or the origin of twin defects will be reliably disclosed and may also serve as input for the generation of training data for ML algorithms.

In summary, we have seen remarkable progress within a relatively short period of time, which we tried to summarize in this review. But clearly, the excitement about metal nanoplates is far from declining and the upcoming progress in synthetic, modeling, and characterization of nanomaterials will surely result in the translation into practical applications related to those described above, or even some that we cannot imagine at this time.

AUTHOR INFORMATION

Corresponding Authors

Luis M. Liz-Marzán − *CIC biomaGUNE, Basque Research and Technology Alliance (BRTA), 20014 Donostia-San Sebastián, Spain; Ikerbasque, 43009 Bilbao, Spain; Networking Research Center on Bioengineering, Biomaterials and Nanomedicine (CIBER-BBN), 20014 Donostia-San Sebastián, Spain; Cinbio, Universidade de Vigo, 36310 Vigo, Spain;* orcid.org/0000-0002-6647-1353; Email: llizmarzan@cicbiomagune.es

Leonardo Scarabelli − *Institue of Materials Science of Barcelona, Bellaterra 08193, Spain;* orcid.org/0000-0002-6830-5893; Email: lscarabelli@icmab.es

https://doi.org/10.1021/acs.chemrev.3c00033
Chem. Rev. 2023, 123, 3493−3542

Jill E. Millstone − *Department of Chemistry, Department of Chemical and Petroleum Engineering, Department of Mechanical Engineering and Materials Science, University of Pittsburgh, Pittsburgh, Pennsylvania 15260, United States;* orcid.org/0000-0002-9499-5744; Email: jem210@pitt.edu

Matthew R. Jones − *Department of Chemistry, Rice University, Houston, Texas 77005, United States; Department of Materials Science & Nanoengineering, Rice University, Houston, Texas 77005, United States;* orcid.org/0000-0002-9289-291X; Email: mrj@rice.edu

Authors

Muhua Sun − *National Center for Electron Microscopy in Beijing, School of Materials Science and Engineering, Tsinghua University, Beijing 100084, People's Republic of China*

Xiaolu Zhuo − *Guangdong Provincial Key Lab of Optoelectronic Materials and Chips, School of Science and Engineering, The Chinese University of Hong Kong (Shenzhen), Shenzhen 518172, China;* orcid.org/0000-0002-5895-3336

Sungjae Yoo − *Research Institute for Nano Bio Convergence, Sungkyunkwan University, Suwon 16419, Republic of Korea; Department of Chemistry, Sungkyunkwan University, Suwon 16419, Republic of Korea; Department of Chemistry, University of Pittsburgh, Pittsburgh, Pennsylvania 15260, United States;* orcid.org/0000-0002-9517-9474

Complete contact information is available at: https://pubs.acs.org/10.1021/acs.chemrev.3c00033

Author Contributions

CRediT: **Leonardo Scarabelli** conceptualization, funding acquisition, investigation, writing-original draft, writing-review & editing; **Muhua Sun** data curation, writing-original draft; **Xiaolu Zhuo** data curation, writing-original draft; **Sungjae Yoo** data curation, writing-original draft; **Jill E. Millstone** conceptualization, data curation, funding acquisition, supervision, writing-original draft, writing-review & editing; **Matthew R. Jones** conceptualization, data curation, funding acquisition, supervision, writing-original draft, writing-review & editing; **Luis M. Liz-Marzán** conceptualization, funding acquisition, supervision, writing-original draft, writing-review & editing.

Notes

The authors declare no competing financial interest.

Biographies

Leonardo Scarabelli earned his B.Sc. and M.Sc. in Chemistry from the University of Pavia and received his Ph.D. from the University of Vigo in 2016, under the direction of Prof. L. M. Liz-Marzán. After training as a postdoctoral scholar at the University of California, Los Angeles, in the laboratory of Prof. P. S. Weiss, he began his independent academic career at the Institute of Materials Science of Barcelona (ICMAB) as a "*La Caixa*" Junior Leader. His current interests include the development of unconventional strategies for the direct surface synthesis of plasmonic arrays, and their implementation into weakly and strongly coupled hybrid plasmonic materials for the promotion of nonlinear optical phenomena and the development of new electrophotocatalysts.

Muhua Sun received her Bachelor's degree from Shandong University (Jinan, China) followed by her Ph.D. degree in Condensed Matter Physics in 2018 from Institute of Physics, Chinese Academy of Sciences (Beijing, China), under the supervision of Prof. Xuedong Bai. After one-year postdoctoral research work at University of Nebraska-Lincoln in Prof. Eli Sutter's group, she joined the group of Prof. Matthew Jones at Rice University as a postdoctoral fellow from 2019 to 2022, working on liquid cell TEM observation of nanocrystal growth on single particle level. She is currently a research scientist at the National Center for Electron Microscopy in Beijing of Tsinghua University. Her research interest focuses on monitoring nanocrystal growth by in situ TEM and unraveling possible microscopic mechanisms.

Xiaolu Zhuo earned her B.Sc. degree in Physics from Sun Yat-sen University and her Ph.D. degree in Physics from the Department of Physics at the Chinese University of Hong Kong under the supervision of Prof. Jianfang Wang. She conducted her postdoctoral research at CIC biomaGUNE (Spain) as a Juan de la Cierva fellow under the direction of Prof. L. M. Liz-Marzán. She is currently an assistant professor at School of Science and Engineering, the Chinese University of Hong Kong (Shenzhen). Her research interests include the synthesis of metallic/dielectric nanoparticles, their optical properties, and applications

Sungjae Yoo is a postdoctoral research associate at the University of Sungkyunkwan, South Korea, and a visiting research fellow at the University of Pittsburgh. He obtained his B.Sc. in Chemistry from University of Kunkuk, South Korea, and his M.Sc and Ph.D. were from the University of Sungkyunkwan. His research interests include synthesis of plasmonic nanostructures having intricate morphologies and multicomponent nanostructures and investigation of their localized surface plasmon resonance and catalytic properties.

Jill E. Millstone is a Professor and the Leo B. and Theresa Y. Wegemer Endowed Chair of Chemistry at the University of Pittsburgh with affiliated appointments in the Departments of Chemical Engineering and Mechanical Engineering and Materials Science. Since joining the faculty at Pitt in 2011, she has received honors, including the NSF CAREER Award, the ACS Unilever Award for Outstanding Young Investigator in Colloid and Surfactant Science, the Cottrell Research Scholar Award, the Chancellor's Distinguished Research Award, and the Kavli Emerging Leader in Chemistry Lectureship. She currently serves as an associate editor at *ACS Nano*, and on the editorial advisory board of several journals including *Journal of Physical Chemistry Letters* and *Chem*. She has served as the Chair of the Nanoscience Division within the Inorganic Chemistry Division of the American Chemical Society. Her group studies the chemical mechanisms underpinning metal and metal-like nanoparticle synthesis, surface chemistry, and optoelectronic behaviors.

Matthew R. Jones is an Assistant Professor of Chemistry and Materials Science & Nanoengineering at Rice University. The expertise of his research group covers the fields of inorganic nanoparticle synthesis, surface chemistry, liquid-phase transmission electron microscopy, and nanoscale self-assembly. Matt is known for discovering an atomically precise gold nanocluster as a precursor in the synthesis of anisotropic nanostructures and developing methods to assemble nanoparticles into chiral superlattice phases for the high-throughput fabrication of plasmonic metamaterials. He is the recipient of numerous awards and honors, including the Packard Fellowship for Science & Engineering, an NSF CAREER award, an Arnold O. Beckman Postdoctoral Fellowship, and an NSF Graduate Research Fellowship. He graduated from Carnegie Mellon University with B.S. degrees in both Materials Science and Biomedical Engineering, he received his Ph.D. from Northwestern University, and completed a postdoctoral fellowship at UC Berkeley before starting his independent career at Rice.

Luis M. Liz-Marzán is an Ikerbasque Professor at CIC biomaGUNE (BRTA), in San Sebastián (Spain), where he also served as Scientific Director from 2012 to 2020. Luis graduated in Chemistry from the

https://doi.org/10.1021/acs.chemrev.3c00033
Chem. Rev. 2023, 123, 3493−3542

University of Santiago de Compostela, was a postdoc at Utrecht University and Professor at the University of Vigo (1995−2012), where he currently holds a part-time Professor position. Luis has been visiting professor at various research institutions worldwide and received numerous scientific awards and honors, including the *ACS Nano* and *Langmuir* Lectureship Awards, European Colloid and Interface Society Rhodia Prize, Jaime I Prize on Basic Sciences, Spanish National Award on Chemical Science and Technology, and Lilly Foundation Award on Preclinical Biomedical Research, among others. He is also a member of the Spanish Royal Academy of Sciences, European Academy of Sciences, and Academia Europaea, and International Member of the National Academy of Engineering (USA). He currently serves as an executive editor at *ACS Nano* and on the editorial advisory board of several other journals. Liz-Marzán is considered as one of the pioneers in the colloidal synthesis and self-assembly of metal nanocrystals as well as the characterization and application of their plasmonic properties. More recently, his research has broadened into the biomedical applications of plasmonic nanostructures.

ACKNOWLEDGMENTS

M.R.J. thanks the Robert A. Welch Foundation (grant C-1954), the David and Lucile Packard Foundation (grant 2018-68049), the National Science Foundation for a CAREER award (grant 2145500), and Rice University for financial support. L.S. receives support from the 2020 "la Caixa"Foundation Postdoctoral Junior Leader-Incoming Fellowship (ID 100010434, fellow-ship code LCF/BQ/PI20/11760028), and from a 2022 Leonardo Grant for Researchers and Cultural Creators, BBVA Foundation. L.M.L.-M. acknowledges funding from the European Research Council (ERC Advanced grant 787510, 4DbioSERS) and the Spanish Ministerio de Ciencia e Innovación, MCIN/AEI/10.13039/501100011033 (grant PID2020-117779RB-I00). X.Z. acknowledges financial support from the Juan de la Cierva fellowship (FJC2018-036104-I) and CUHK-Shenzhen (UDF01002665). M.S. thanks the Natural Science Foundation of China for their support (grant no. 22202133). J.E.M. thanks Leo and Theresa Wegemer for their generous support.

ABBREVIATIONS

2D = two-dimensional
3D = three-dimensional
AI = artificial intelligence
bcc = body-centered cubic
CL = cathodoluminescence
CTAB = cetyltrimethylammonium bromide
CTAC = cetyltrimethylammonium chloride
DFT = density functional theory
DMF = *N*,*N*-dimethylformamide
fcc = face-centered cubic
EBL = electron beam lithography
EDX = energy-dispersive X-ray spectroscopy
EELS = electron energy loss spectroscopy
EOR = ethanol oxidation reaction
FAOR = formic acid oxidation reaction
FFT = fast Fourier transform
FIB = focused ion beam
FM = Frank-van der Merwe
GRR = galvanic replacement reactions
HAADF-STEM = high-angle annular dark field scanning transmission electron microscopy
hcp = hexagonal close packed
HR = high resolution
LR = long range
LSPR = localized surface plasmon resonance
MD = molecular dynamics
MIR = mid-infrared
ML = machine learning
MOR = methanol oxidation reaction
NIR = near-infrared
NPoM = nanoparticle-on-mirror
ORR = oxygen reduction reaction
PIAF = particles in a frame nanostructure
PVP = polyvinylpyrrolidone
RIU = refractive index unit
SAED = selected area electron diffraction
SEIRA = surface-enhanced infrared absorption
SEM = scanning electron microscopy
SERS = surface-enhanced Raman scattering
SK = Stranski-Krastanov
SNOM = scanning near-field optical microscopy
SPP = surface plasmon polariton
SR = short range
TEM = transmission electron microscopy
TERS = tip-enhanced Raman scattering
TIPPL = two-photon excited photoluminescence
TMDC = transition metal dichalcogenides
TR-2PPE-PEEM = time-resolved two-photon photoemission electron microscopy
UPD = underpotential deposition
vis = visible
UV = ultraviolet
vdW = van der Waals
VW = Volmer−Weber
XRD = X-ray diffraction

REFERENCES

(1) Turkevich, J.; Stevenson, P. C.; Hillier, J. A Study of the Nucleation and Growth Processes in the Synthesis of Colloidal Gold. *Discuss. Faraday Soc.* **1951**, *11*, 55−75.
(2) Frens, G. Controlled Nucleation for the Regulation of the Particle Size in Monodisperse Gold Suspensions. *Nat. Phys. Sci.* **1973**, *241*, 20−22.
(3) Sun, Y.; Xia, Y. Shape-Controlled Synthesis of Gold and Silver Nanoparticles. *Science* **2002**, *298*, 2176−2179.
(4) Jana, N. R.; Gearheart, L.; Murphy, C. J. Wet Chemical Synthesis of High Aspect Ratio Cylindrical Gold Nanorods. *J. Phys. Chem. B* **2001**, *105*, 4065−4067.
(5) Nikoobakht, B.; El-Sayed, M. A. Preparation and Growth Mechanism of Gold Nanorods (NRs) Using Seed-Mediated Growth Method. *Chem. Mater.* **2003**, *15*, 1957−1962.
(6) Jin, R.; Cao, Y.; Mirkin, C. A.; Kelly, K. L.; Schatz, G. C.; Zheng, J. G. Photoinduced Conversion of Silver Nanospheres to Nanoprisms. *Science* **2001**, *294*, 1901−1903.
(7) Xia, Y.; Xiong, Y.; Lim, B.; Skrabalak, S. E. Shape-Controlled Synthesis of Metal Nanocrystals: Simple Chemistry Meets Complex Physics? *Angew. Chem., Int. Ed.* **2009**, *48*, 60−103.
(8) Nguyen, Q. N.; Wang, C.; Shang, Y.; Janssen, A.; Xia, Y. Colloidal Synthesis of Metal Nanocrystals: From Asymmetrical Growth to Symmetry Breaking. *Chem. Rev.* **2022**, DOI: 10.1021/acs.chemrev.2c00468.
(9) Liz-Marzán, L. *Colloidal Synthesis of Plasmonic Nanometals*; CRC Press, 2020.
(10) Ma, Y.; Cao, Z.; Hao, J.; Zhou, J.; Yang, Z.; Yang, Y.; Wei, J. Controlled Synthesis of Au Chiral Propellers from Seeded Growth of Au Nanoplates for Chiral Differentiation of Biomolecules. *J. Phys. Chem. C* **2020**, *124*, 24306−24314.

(11) Besteiro, L. V.; Movsesyan, A.; Ávalos-Ovando, O.; Lee, S.; Cortés, E.; Correa-Duarte, M. A.; Wang, Z. M.; Govorov, A. O. Local Growth Mediated by Plasmonic Hot Carriers: Chirality from Achiral Nanocrystals Using Circularly Polarized Light. *Nano Lett.* **2021**, *21*, 10315−10324.
(12) Scarabelli, L. Recent Advances in the Rational Synthesis and Self-Assembly of Anisotropic Plasmonic Nanoparticles. *Pure Appl. Chem.* **2018**, *90*, 1393−1407.
(13) Mayer, M.; Scarabelli, L.; March, K.; Altantzis, T.; Tebbe, M.; Kociak, M.; Bals, S.; García de Abajo, F. J.; Fery, A.; Liz-Marzán, L. M. Controlled Living Nanowire Growth: Precise Control over the Morphology and Optical Properties of AgAuAg Bimetallic Nanowires. *Nano Lett.* **2015**, *15*, 5427−5437.
(14) Gole, A.; Murphy, C. J. Seed-Mediated Synthesis of Gold Nanorods: Role of the Size and Nature of the Seed. *Chem. Mater.* **2004**, *16*, 3633−3640.
(15) Lohse, S. E.; Murphy, C. J. The Quest for Shape Control: A History of Gold Nanorod Synthesis. *Chem. Mater.* **2013**, *25*, 1250−1261.
(16) Jones, M. R.; Macfarlane, R. J.; Lee, B.; Zhang, J.; Young, K. L.; Senesi, A. J.; Mirkin, C. A. DNA-Nanoparticle Superlattices Formed from Anisotropic Building Blocks. *Nat. Mater.* **2010**, *9*, 913−917.
(17) Jones, M. R.; Kohlstedt, K. L.; O'Brien, M. N.; Wu, J.; Schatz, G. C.; Mirkin, C. A. Deterministic Symmetry Breaking of Plasmonic Nanostructures Enabled by DNA-Programmable Assembly. *Nano Lett.* **2017**, *17*, 5830−5835.
(18) Rehn, S. M.; Gerrard-Anderson, T. M.; Qiao, L.; Zhu, Q.; Wehmeyer, G.; Jones, M. R. Mechanical Reshaping of Inorganic Nanostructures with Weak Nanoscale Forces. *Nano Lett.* **2021**, *21*, 130−135.
(19) Chhowalla, M.; Shin, H. S.; Eda, G.; Li, L.-J.; Loh, K. P.; Zhang, H. The Chemistry of Two-Dimensional Layered Transition Metal Dichalcogenide Nanosheets. *Nat. Chem.* **2013**, *5*, 263−275.
(20) Novoselov, K. S.; Mishchenko, A.; Carvalho, A.; Castro Neto, A. H. 2D Materials and van Der Waals Heterostructures. *Science* **2016**, *353*, aac9439.
(21) Xu, M.; Liang, T.; Shi, M.; Chen, H. Graphene-Like Two-Dimensional Materials. *Chem. Rev.* **2013**, *113*, 3766−3798.
(22) Tan, C.; Cao, X.; Wu, X.-J.; He, Q.; Yang, J.; Zhang, X.; Chen, J.; Zhao, W.; Han, S.; Nam, G.-H.; et al. Recent Advances in Ultrathin Two-Dimensional Nanomaterials. *Chem. Rev.* **2017**, *117*, 6225−6331.
(23) Cai, Z.; Liu, B.; Zou, X.; Cheng, H.-M. Chemical Vapor Deposition Growth and Applications of Two-Dimensional Materials and Their Heterostructures. *Chem. Rev.* **2018**, *118*, 6091−6133.
(24) Jin, H.; Guo, C.; Liu, X.; Liu, J.; Vasileff, A.; Jiao, Y.; Zheng, Y.; Qiao, S.-Z. Emerging Two-Dimensional Nanomaterials for Electrocatalysis. *Chem. Rev.* **2018**, *118*, 6337−6408.
(25) Pastoriza-Santos, I.; Liz-Marzán, L. M. Colloidal Silver Nanoplates. State of the Art and Future Challenges. *J. Mater. Chem.* **2008**, *18*, 1724−1737.
(26) Millstone, J. E.; Hurst, S. J.; Métraux, G. S.; Cutler, J. I.; Mirkin, C. A. Colloidal Gold and Silver Triangular Nanoprisms. *Small* **2009**, *5*, 646−664.
(27) Zhang, Q.; Li, N.; Goebl, J.; Lu, Z.; Yin, Y. A Systematic Study of the Synthesis of Silver Nanoplates: Is Citrate a "Magic" Reagent? *J. Am. Chem. Soc.* **2011**, *133*, 18931−18939.
(28) Zhang, Q.; Hu, Y.; Guo, S.; Goebl, J.; Yin, Y. Seeded Growth of Uniform Ag Nanoplates with High Aspect Ratio and Widely Tunable Surface Plasmon Bands. *Nano Lett.* **2010**, *10*, 5037−5042.
(29) Tao, A. R.; Habas, S.; Yang, P. Shape Control of Colloidal Metal Nanocrystals. *Small* **2008**, *4*, 310−325.
(30) Ringe, E. Shapes, Plasmonic Properties, and Reactivity of Magnesium Nanoparticles. *J. Phys. Chem. C* **2020**, *124*, 15665−15679.
(31) Wang, Z. L. Transmission Electron Microscopy of Shape-Controlled Nanocrystals and Their Assemblies. *J. Phys. Chem. B* **2000**, *104*, 1153−1175.
(32) Chen, M.; Wu, B.; Yang, J.; Zheng, N. Small Adsorbate-Assisted Shape Control of Pd and Pt Nanocrystals. *Adv. Mater.* **2012**, *24*, 862−879.
(33) González-Rubio, G.; Scarabelli, L.; Guerrero-Martínez, A.; Liz-Marzán, L. M. Surfactant-Assisted Symmetry Breaking in Colloidal Gold Nanocrystal Growth. *ChemNanoMat* **2020**, *6*, 698−707.
(34) Lim, B.; Jiang, M.; Tao, J.; Camargo, P. H. C.; Zhu, Y.; Xia, Y. Shape-Controlled Synthesis of Pd Nanocrystals in Aqueous Solutions. *Adv. Funct. Mater.* **2009**, *19*, 189−200.
(35) Xiong, Y.; Xia, Y. Shape-Controlled Synthesis of Metal Nanostructures: The Case of Palladium. *Adv. Mater.* **2007**, *19*, 3385−3391.
(36) Tan, T.; Zhang, S.; Wang, J.; Zheng, Y.; Lai, H.; Liu, J.; Qin, F.; Wang, C. Resolving the Stacking Fault Structure of Silver Nanoplates. *Nanoscale* **2021**, *13*, 195−205.
(37) Carbó-Argibay, E.; Rodríguez-González, B. Controlled Growth of Colloidal Gold Nanoparticles: Single-Crystalline versus Multiply-Twinned Particles. *Isr. J. Chem.* **2016**, *56*, 214−226.
(38) Sánchez-Iglesias, A.; Pastoriza-Santos, I.; Pérez-Juste, J.; Rodríguez-González, B.; García de Abajo, F. J.; Liz-Marzán, L. M. Synthesis and Optical Properties of Gold Nanodecahedra with Size Control. *Adv. Mater.* **2006**, *18*, 2529−2534.
(39) Lofton, C.; Sigmund, W. Mechanisms Controlling Crystal Habits of Gold and Silver Colloids. *Adv. Funct. Mater.* **2005**, *15*, 1197−1208.
(40) Germain, V.; Li, J.; Ingert, D.; Wang, Z. L.; Pileni, M. P. Stacking Faults in Formation of Silver Nanodisks. *J. Phys. Chem. B* **2003**, *107*, 8717−8720.
(41) *Materials Science & Engineering−Taking You from Student to Professional in the Field of Materials Science*; Materials Science & Engineering Student, 2022; https://msestudent.com/ (accessed 2022-11-22).
(42) Skrabalak, S. E. Symmetry in Seeded Metal Nanocrystal Growth. *Acc. Mater. Res.* **2021**, *2*, 621−629.
(43) O'Brien, M. N.; Jones, M. R.; Brown, K. A.; Mirkin, C. A. Universal Noble Metal Nanoparticle Seeds Realized Through Iterative Reductive Growth and Oxidative Dissolution Reactions. *J. Am. Chem. Soc.* **2014**, *136*, 7603−7606.
(44) Sun, M.; Cheng, Z.; Chen, W.; Jones, M. Understanding Symmetry Breaking at the Single-Particle Level via the Growth of Tetrahedron-Shaped Nanocrystals from Higher-Symmetry Precursors. *ACS Nano* **2021**, *15*, 15953−15961.
(45) González-Rubio, G.; Kumar, V.; Llombart, P.; Díaz-Núñez, P.; Bladt, E.; Altantzis, T.; Bals, S.; Peña-Rodríguez, O.; Noya, E. G.; MacDowell, L. G.; et al. Disconnecting Symmetry Breaking from Seeded Growth for the Reproducible Synthesis of High Quality Gold Nanorods. *ACS Nano* **2019**, *13*, 4424−4435.
(46) González-Rubio, G.; de Oliveira, T. M.; Altantzis, T.; La Porta, A.; Guerrero-Martínez, A.; Bals, S.; Scarabelli, L.; Liz-Marzán, L. M. Disentangling the Effect of Seed Size and Crystal Habit on Gold Nanoparticle Seeded Growth. *Chem. Commun.* **2017**, *53*, 11360−11363.
(47) Sánchez-Iglesias, A.; Winckelmans, N.; Altantzis, T.; Bals, S.; Grzelczak, M.; Liz-Marzán, L. M. High-Yield Seeded Growth of Monodisperse Pentatwinned Gold Nanoparticles through Thermally Induced Seed Twinning. *J. Am. Chem. Soc.* **2017**, *139*, 107−110.
(48) Marks, L. D.; Peng, L. Nanoparticle Shape, Thermodynamics and Kinetics. *J. Phys. Cond. Matt.* **2016**, *28*, 053001.
(49) Personick, M. L.; Langille, M. R.; Wu, J.; Mirkin, C. A. Synthesis of Gold Hexagonal Bipyramids Directed by Planar-Twinned Silver Triangular Nanoprisms. *J. Am. Chem. Soc.* **2013**, *135*, 3800−3803.
(50) Laramy, C. R.; Fong, L.-K.; Jones, M. R.; O'Brien, M. N.; Schatz, G. C.; Mirkin, C. A. Understanding Nanoparticle-Mediated Nucleation Pathways of Anisotropic Nanoparticles. *Chem. Phys. Lett.* **2017**, *683*, 389−392.
(51) Ajayan, P. M.; Marks, L. D. Quasimelting and Phases of Small Particles. *Phys. Rev. Lett.* **1988**, *60*, 585−587.
(52) Wang, Y.; Peng, H.-C.; Liu, J.; Huang, C. Z.; Xia, Y. Use of Reduction Rate as a Quantitative Knob for Controlling the Twin Structure and Shape of Palladium Nanocrystals. *Nano Lett.* **2015**, *15*, 1445−1450.

(53) Yan, J.; Teo, B. K.; Zheng, N. Surface Chemistry of Atomically Precise Coinage−Metal Nanoclusters: From Structural Control to Surface Reactivity and Catalysis. *Acc. Chem. Res.* **2018**, *51*, 3084−3093.
(54) Lei, Z.; Wan, X.-K.; Yuan, S.-F.; Guan, Z.-J.; Wang, Q.-M. Alkynyl Approach toward the Protection of Metal Nanoclusters. *Acc. Chem. Res.* **2018**, *51*, 2465−2474.
(55) Kang, X.; Li, Y.; Zhu, M.; Jin, R. Atomically Precise Alloy Nanoclusters: Syntheses, Structures, and Properties. *Chem. Soc. Rev.* **2020**, *49*, 6443−6514.
(56) Jin, R.; Zeng, C.; Zhou, M.; Chen, Y. Atomically Precise Colloidal Metal Nanoclusters and Nanoparticles: Fundamentals and Opportunities. *Chem. Rev.* **2016**, *116*, 10346−10413.
(57) Song, Y.; Li, Y.; Zhou, M.; Li, H.; Xu, T.; Zhou, C.; Ke, F.; Huo, D.; Wan, Y.; Jie, J.; et al. Atomic Structure of a Seed-Sized Gold Nanoprism. *Nat. Commun.* **2022**, *13*, 1235.
(58) Qiao, L.; Pollard, N.; Senanayake, R.; Yang, Z.; Kim, M.; Ali, A.; Hoang, M. T.; Yao, N.; Han, Y.; Hernandez, R.; Clayborne, A.; Jones, M. Particle or Cluster: On the Atomic Structure of the Seeds Used in Gold Nanoparticle Synthesis. *ChemRxiv* 2022, 2022-r18wr
(59) Loh, N. D.; Sen, S.; Bosman, M.; Tan, S. F.; Zhong, J.; Nijhuis, C. A.; Král, P.; Matsudaira, P.; Mirsaidov, U. Multistep Nucleation of Nanocrystals in Aqueous Solution. *Nat. Chem.* **2017**, *9*, 77−82.
(60) Zheng, H.; Smith, R. K.; Jun, Y.; Kisielowski, C.; Dahmen, U.; Alivisatos, A. P. Observation of Single Colloidal Platinum Nanocrystal Growth Trajectories. *Science* **2009**, *324*, 1309−1312.
(61) Yuk, J. M.; Park, J.; Ercius, P.; Kim, K.; Hellebusch, D. J.; Crommie, M. F.; Lee, J. Y.; Zettl, A.; Alivisatos, A. P. High-Resolution EM of Colloidal Nanocrystal Growth Using Graphene Liquid Cells. *Science* **2012**, *336*, 61−64.
(62) Reboul, C. F.; Heo, J.; Machello, C.; Kiesewetter, S.; Kim, B. H.; Kim, S.; Elmlund, D.; Ercius, P.; Park, J.; Elmlund, H.; et al. SINGLE: Atomic-Resolution Structure Identification of Nanocrystals by Graphene Liquid Cell EM. *Sci. Adv.* **2021**, *7*, No. eabe6679.
(63) Xia, Y.; Xia, X.; Peng, H.-C. Shape-Controlled Synthesis of Colloidal Metal Nanocrystals: Thermodynamic versus Kinetic Products. *J. Am. Chem. Soc.* **2015**, *137*, 7947−7966.
(64) Wiley, B.; Herricks, T.; Sun, Y.; Xia, Y. Polyol Synthesis of Silver Nanoparticles: Use of Chloride and Oxygen to Promote the Formation of Single-Crystal, Truncated Cubes and Tetrahedrons. *Nano Lett.* **2004**, *4*, 1733−1739.
(65) Chen, L.; Ji, F.; Xu, Y.; He, L.; Mi, Y.; Bao, F.; Sun, B.; Zhang, X.; Zhang, Q. High-Yield Seedless Synthesis of Triangular Gold Nanoplates through Oxidative Etching. *Nano Lett.* **2014**, *14*, 7201−7206.
(66) Xiong, Y.; Chen, J.; Wiley, B.; Xia, Y.; Aloni, S.; Yin, Y. Understanding the Role of Oxidative Etching in the Polyol Synthesis of Pd Nanoparticles with Uniform Shape and Size. *J. Am. Chem. Soc.* **2005**, *127*, 7332−7333.
(67) Chateau, D.; Liotta, A.; Vadcard, F.; Navarro, J. R. G.; Chaput, F.; Lermé, J.; Lerouge, F.; Parola, S. From Gold Nanobipyramids to Nanojavelins for a Precise Tuning of the Plasmon Resonance to the Infrared Wavelengths: Experimental and Theoretical Aspects. *Nanoscale* **2015**, *7*, 1934−1943.
(68) Xiong, Y.; McLellan, J. M.; Yin, Y.; Xia, Y. Synthesis of Palladium Icosahedra with Twinned Structure by Blocking Oxidative Etching with Citric Acid or Citrate Ions. *Angew. Chem., Int. Ed.* **2007**, *46*, 790−794.
(69) Berriman, R. W.; Herz, R. H. Twinning and the Tabular Growth of Silver Bromide Crystals. *Nature* **1957**, *180*, 293−294.
(70) Cahn, R. W. Twinned Crystals. *Adv. Phys.* **1954**, *3*, 363−445.
(71) Hamilton, D. R.; Seidensticker, R. G. Propagation Mechanism of Germanium Dendrites. *J. Appl. Phys.* **1960**, *31*, 1165−1168.
(72) Park, J. H.; Schneider, N. M.; Grogan, J. M.; Reuter, M. C.; Bau, H. H.; Kodambaka, S.; Ross, F. M. Control of Electron Beam-Induced Au Nanocrystal Growth Kinetics through Solution Chemistry. *Nano Lett.* **2015**, *15*, 5314−5320.
(73) Alloyeau, D.; Dachraoui, W.; Javed, Y.; Belkahla, H.; Wang, G.; Lecoq, H.; Ammar, S.; Ersen, O.; Wisnet, A.; Gazeau, F.; et al. Unravelling Kinetic and Thermodynamic Effects on the Growth of Gold Nanoplates by Liquid Transmission Electron Microscopy. *Nano Lett.* **2015**, *15*, 2574−2581.
(74) Nasilowski, M.; Mahler, B.; Lhuillier, E.; Ithurria, S.; Dubertret, B. Two-Dimensional Colloidal Nanocrystals. *Chem. Rev.* **2016**, *116*, 10934−10982.
(75) Evans, J. S.; Beier, C. N.; Smalyukh, I. I. Alignment of High-Aspect Ratio Colloidal Gold Nanoplatelets in Nematic Liquid Crystals. *J. Appl. Phys.* **2011**, *110*, 033535.
(76) Liu, P.; Qin, R.; Fu, G.; Zheng, N. Surface Coordination Chemistry of Metal Nanomaterials. *J. Am. Chem. Soc.* **2017**, *139*, 2122−2131.
(77) Métraux, G. S.; Mirkin, C. A. Rapid Thermal Synthesis of Silver Nanoprisms with Chemically Tailorable Thickness. *Adv. Mater.* **2005**, *17*, 412−415.
(78) Yang, T.-H.; Shi, Y.; Janssen, A.; Xia, Y. Surface Capping Agents and Their Roles in Shape-Controlled Synthesis of Colloidal Metal Nanocrystals. *Angew. Chem., Int. Ed.* **2020**, *59*, 15378−15401.
(79) Kilin, D. S.; Prezhdo, O. V.; Xia, Y. Shape-Controlled Synthesis of Silver Nanoparticles: Ab Initio Study of Preferential Surface Coordination with Citric Acid. *Chem. Phys. Lett.* **2008**, *458*, 113−116.
(80) Figueroa-Cosme, L.; Hood, Z. D.; Gilroy, K. D.; Xia, Y. A Facile, Robust and Scalable Method for the Synthesis of Pd Nanoplates with Hydroxylamine as a Reducing Agent and Mechanistic Insights from Kinetic Analysis. *J. Mater. Chem. C* **2018**, *6*, 4677−4682.
(81) Lim, B.; Xiong, Y.; Xia, Y. A Water-Based Synthesis of Octahedral, Decahedral, and Icosahedral Pd Nanocrystals. *Angew. Chem., Int. Ed.* **2007**, *46*, 9279−9282.
(82) Xu, H.; Wiley, B. J. The Roles of Citrate and Defects in the Anisotropic Growth of Ag Nanostructures. *Chem. Mater.* **2021**, *33*, 8301−8311.
(83) Millstone, J. E.; Wei, W.; Jones, M. R.; Yoo, H.; Mirkin, C. A. Iodide Ions Control Seed-Mediated Growth of Anisotropic Gold Nanoparticles. *Nano Lett.* **2008**, *8*, 2526−2529.
(84) DuChene, J. S.; Niu, W.; Abendroth, J. M.; Sun, Q.; Zhao, W.; Huo, F.; Wei, W. D. Halide Anions as Shape-Directing Agents for Obtaining High-Quality Anisotropic Gold Nanostructures. *Chem. Mater.* **2013**, *25*, 1392−1399.
(85) Langille, M. R.; Personick, M. L.; Zhang, J.; Mirkin, C. A. Defining Rules for the Shape Evolution of Gold Nanoparticles. *J. Am. Chem. Soc.* **2012**, *134*, 14542−14554.
(86) Scarabelli, L.; Coronado-Puchau, M.; Giner-Casares, J. J.; Langer, J.; Liz-Marzán, L. M. Monodisperse Gold Nanotriangles: Size Control, Large-Scale Self-Assembly, and Performance in Surface-Enhanced Raman Scattering. *ACS Nano* **2014**, *8*, 5833−5842.
(87) Scarabelli, L.; Liz-Marzán, L. M. An Extended Protocol for the Synthesis of Monodisperse Gold Nanotriangles. *ACS Nano* **2021**, *15*, 18600−18607.
(88) Huang, X.; Tang, S.; Mu, X.; Dai, Y.; Chen, G.; Zhou, Z.; Ruan, F.; Yang, Z.; Zheng, N. Freestanding Palladium Nanosheets with Plasmonic and Catalytic Properties. *Nat. Nanotechnol.* **2011**, *6*, 28−32.
(89) Luo, L.; Li, Y.; Sun, X.; Li, J.; Hu, E.; Liu, Y.; Tian, Y.; Yang, X.-Q.; Li, Y.; Lin, W.-F.; et al. Synthesis and Properties of Stable Sub-2-nm-Thick Aluminum Nanosheets: Oxygen Passivation and Two-Photon Luminescence. *Chem.* **2020**, *6*, 448−459.
(90) Ghosh, S.; Manna, L. The Many "Facets" of Halide Ions in the Chemistry of Colloidal Inorganic Nanocrystals. *Chem. Rev.* **2018**, *118*, 7804−7864.
(91) Wu, X.; Redmond, P. L.; Liu, H.; Chen, Y.; Steigerwald, M.; Brus, L. Photovoltage Mechanism for Room Light Conversion of Citrate Stabilized Silver Nanocrystal Seeds to Large Nanoprisms. *J. Am. Chem. Soc.* **2008**, *130*, 9500−9506.
(92) Maillard, M.; Huang, P.; Brus, L. Silver Nanodisk Growth by Surface Plasmon Enhanced Photoreduction of Adsorbed [Ag^+]. *Nano Lett.* **2003**, *3*, 1611−1615.
(93) Sun, M.; Li, Y.; Zhang, B.; Argyropoulos, C.; Sutter, P.; Sutter, E. Plasmonic Effects on the Growth of Ag Nanocrystals in Solution. *Langmuir* **2020**, *36*, 2044−2051.
(94) Huang, B.; Miao, L.; Li, J.; Xie, Z.; Wang, Y.; Chai, J.; Zhai, Y. Identification of Plasmon-Driven Nanoparticle-Coalescence-Dominated Growth of Gold Nanoplates through Nanopore Sensing. *Nat. Commun.* **2022**, *13*, 1402.

https://doi.org/10.1021/acs.chemrev.3c00033
Chem. Rev. 2023, 123, 3493−3542

(95) Zhai, Y.; DuChene, J. S.; Wang, Y.-C.; Qiu, J.; Johnston-Peck, A. C.; You, B.; Guo, W.; DiCiaccio, B.; Qian, K.; Zhao, E. W.; et al. Polyvinylpyrrolidone-Induced Anisotropic Growth of Gold Nanoprisms in Plasmon-Driven Synthesis. *Nat. Mater.* **2016**, *15*, 889−895.
(96) Goris, B.; Polavarapu, L.; Bals, S.; Van Tendeloo, G.; Liz-Marzán, L. M. Monitoring Galvanic Replacement Through Three-Dimensional Morphological and Chemical Mapping. *Nano Lett.* **2014**, *14*, 3220−3226.
(97) Sun, Y.; Mayers, B.; Xia, Y. Metal Nanostructures with Hollow Interiors. *Adv. Mater.* **2003**, *15*, 641−646.
(98) Seo, D.; Song, H. Asymmetric Hollow Nanorod Formation through a Partial Galvanic Replacement Reaction. *J. Am. Chem. Soc.* **2009**, *131*, 18210−18211.
(99) Sun, Y.; Xia, Y. Alloying and Dealloying Processes Involved in the Preparation of Metal Nanoshells through a Galvanic Replacement Reaction. *Nano Lett.* **2003**, *3*, 1569−1572.
(100) da Silva, A. G. M.; Rodrigues, T. S.; Haigh, S. J.; Camargo, P. H. C. Galvanic Replacement Reaction: Recent Developments for Engineering Metal Nanostructures towards Catalytic Applications. *Chem. Commun.* **2017**, *53*, 7135−7148.
(101) González, E.; Arbiol, J.; Puntes, V. F. Carving at the Nanoscale: Sequential Galvanic Exchange and Kirkendall Growth at Room Temperature. *Science* **2011**, *334*, 1377−1380.
(102) Herrero, E.; Buller, L. J.; Abruña, H. D. Underpotential Deposition at Single Crystal Surfaces of Au, Pt, Ag and Other Materials. *Chem. Rev.* **2001**, *101*, 1897−1930.
(103) Oviedo, O. A.; Vélez, P.; Macagno, V. A.; Leiva, E. P. M. Underpotential Deposition: From Planar Surfaces to Nanoparticles. *Surf. Sci.* **2015**, *631*, 23−34.
(104) Personick, M. L.; Langille, M. R.; Zhang, J.; Mirkin, C. A. Shape Control of Gold Nanoparticles by Silver Underpotential Deposition. *Nano Lett.* **2011**, *11*, 3394−3398.
(105) Michely, T.; Krug, J. *Islands, Mounds and Atoms*; Springer Science & Business Media, 2012.
(106) Venables, J. A.; Spiller, G. D. T.; Hanbucken, M. Nucleation and Growth of Thin Films. *Rep. Prog. Phys.* **1984**, *47*, 399−459.
(107) Frank, F. C.; van der Merwe, J. H.; Mott, N. F. One-Dimensional Dislocations. I. Static Theory. *Proc. R. Soc. London Ser. Math. Phys. Sci.* **1949**, *198*, 205−216.
(108) Baskaran, A.; Smereka, P. Mechanisms of Stranski-Krastanov Growth. *J. Appl. Phys.* **2012**, *111*, 044321.
(109) Gao, Z.; Ye, H.; Tang, D.; Tao, J.; Habibi, S.; Minerick, A.; Tang, D.; Xia, X. Platinum-Decorated Gold Nanoparticles with Dual Functionalities for Ultrasensitive Colorimetric In Vitro Diagnostics. *Nano Lett.* **2017**, *17*, 5572−5579.
(110) Straney, P. J.; Marbella, L. E.; Andolina, C. M.; Nuhfer, N. T.; Millstone, J. E. Decoupling Mechanisms of Platinum Deposition on Colloidal Gold Nanoparticle Substrates. *J. Am. Chem. Soc.* **2014**, *136*, 7873−7876.
(111) Leary, R. K.; Kumar, A.; Straney, P. J.; Collins, S. M.; Yazdi, S.; Dunin-Borkowski, R. E.; Midgley, P. A.; Millstone, J. E.; Ringe, E. Structural and Optical Properties of Discrete Dendritic Pt Nanoparticles on Colloidal Au Nanoprisms. *J. Phys. Chem. C* **2016**, *120*, 20843−20851.
(112) Waibel, H.-F.; Kleinert, M.; Kibler, L. A.; Kolb, D. M. Initial Stages of Pt Deposition on Au(111) and Au(100). *Electrochim. Acta* **2002**, *47*, 1461−1467.
(113) Griffin, S.; Montoni, N. P.; Li, G.; Straney, P. J.; Millstone, J. E.; Masiello, D. J.; Camden, J. P. Imaging Energy Transfer in Pt-Decorated Au Nanoprisms via Electron Energy-Loss Spectroscopy. *J. Phys. Chem. Lett.* **2016**, *7*, 3825−3832.
(114) Kim, Y.; Hong, J. W.; Lee, Y. W.; Kim, M.; Kim, D.; Yun, W. S.; Han, S. W. Synthesis of AuPt Heteronanostructures with Enhanced Electrocatalytic Activity toward Oxygen Reduction. *Angew. Chem., Int. Ed.* **2010**, *49*, 10197−10201.
(115) Straney, P. J.; Diemler, N. A.; Smith, A. M.; Eddinger, Z. E.; Gilliam, M. S.; Millstone, J. E. Ligand-Mediated Deposition of Noble Metals at Nanoparticle Plasmonic Hotspots. *Langmuir* **2018**, *34*, 1084−1091.
(116) Jang, H.-J.; Hong, S.; Park, S. Shape-Controlled Synthesis of Pt Nanoframes. *J. Mater. Chem.* **2012**, *22*, 19792−19797.
(117) Jang, H.-J.; Hong, S.; Ham, S.; Shuford, K. L.; Park, S. Site-Specific Growth of a Pt Shell on Au Nanoplates: Tailoring Their Surface Plasmonic Behavior. *Nanoscale* **2014**, *6*, 7339−7345.
(118) Métraux, G. S.; Cao, Y. C.; Jin, R.; Mirkin, C. A. Triangular Nanoframes Made of Gold and Silver. *Nano Lett.* **2003**, *3*, 519−522.
(119) Sun, Y.; Xia, Y. Triangular Nanoplates of Silver: Synthesis, Characterization, and Use as Sacrificial Templates For Generating Triangular Nanorings of Gold. *Adv. Mater.* **2003**, *15*, 695−699.
(120) Lee, S.; Kim, J.; Yang, H.; Cortés, E.; Kang, S.; Han, S. W. Particle-in-a-Frame Nanostructures with Interior Nanogaps. *Angew. Chem., Int. Ed.* **2019**, *58*, 15890−15894.
(121) Shahjamali, M. M.; Bosman, M.; Cao, S.; Huang, X.; Cao, X.; Zhang, H.; Pramana, S. S.; Xue, C. Surfactant-Free Sub-2 Nm Ultrathin Triangular Gold Nanoframes. *Small* **2013**, *9*, 2880−2886.
(122) Wang, W.; Yan, Y.; Zhou, N.; Zhang, H.; Li, D.; Yang, D. Seed-Mediated Growth of Au Nanorings with Size Control on Pd Ultrathin Nanosheets and Their Tunable Surface Plasmonic Properties. *Nanoscale* **2016**, *8*, 3704−3710.
(123) Jang, H.-J.; Ham, S.; Acapulco, J. A. I., Jr.; Song, Y.; Hong, S.; Shuford, K. L.; Park, S. Fabrication of 2D Au Nanorings with Pt Framework. *J. Am. Chem. Soc.* **2014**, *136*, 17674−17680.
(124) Fan, F.-R.; Liu, D.-Y.; Wu, Y.-F.; Duan, S.; Xie, Z.-X.; Jiang, Z.-Y.; Tian, Z.-Q. Epitaxial Growth of Heterogeneous Metal Nanocrystals: From Gold Nano-Octahedra to Palladium and Silver Nanocubes. *J. Am. Chem. Soc.* **2008**, *130*, 6949−6951.
(125) Millstone, J. E.; Métraux, G. S.; Mirkin, C. A. Controlling the Edge Length of Gold Nanoprisms via a Seed-Mediated Approach. *Adv. Funct. Mater.* **2006**, *16*, 1209−1214.
(126) Kuttner, C.; Mayer, M.; Dulle, M.; Moscoso, A.; López-Romero, J. M.; Förster, S.; Fery, A.; Pérez-Juste, J.; Contreras-Cáceres, R. Seeded Growth Synthesis of Gold Nanotriangles: Size Control, SAXS Analysis, and SERS Performance. *ACS Appl. Mater. Interfaces* **2018**, *10*, 11152−11163.
(127) Hong, S.; Shuford, K. L.; Park, S. Shape Transformation of Gold Nanoplates and Their Surface Plasmon Characterization: Triangular to Hexagonal Nanoplates. *Chem. Mater.* **2011**, *23*, 2011−2013.
(128) Qin, F.; Zhao, T.; Jiang, R.; Jiang, N.; Ruan, Q.; Wang, J.; Sun, L.-D.; Yan, C.-H.; Lin, H.-Q. Thickness Control Produces Gold Nanoplates with Their Plasmon in the Visible and Near-Infrared Regions. *Adv. Optical Mater.* **2016**, *4*, 76−85.
(129) Zeng, J.; Xia, X.; Rycenga, M.; Henneghan, P.; Li, Q.; Xia, Y. Successive Deposition of Silver on Silver Nanoplates: Lateral versus Vertical Growth. *Angew. Chem., Int. Ed.* **2011**, *50*, 244−249.
(130) Hong, S.; Choi, Y.; Park, S. Shape Control of Ag Shell Growth on Au Nanodisks. *Chem. Mater.* **2011**, *23*, 5375−5378.
(131) Kim, J.; Yoo, S.; Kim, J.-M.; Choi, S.; Kim, J.; Park, S.-J.; Park, D.; Nam, J.-M.; Park, S. Synthesis and Single-Particle Surface-Enhanced Raman Scattering Study of Plasmonic Tripod Nanoframes with Y-Shaped Hot-Zones. *Nano Lett.* **2020**, *20*, 4362−4369.
(132) Li, Y.; Lin, H.; Zhou, W.; Sun, L.; Samanta, D.; Mirkin, C. A. Corner-, Edge-, and Facet-Controlled Growth of Nanocrystals. *Sci. Adv.* **2021**, *7*, No. eabf1410.
(133) Boukouvala, C.; Hopper, E. R.; Kelly, D. M.; Knight, P. J.; Biggins, J. S.; Ringe, E. Beyond Simple Crystal Systems: Identifying Twinning in Body-Centered Tetragonal Nanoparticles. *Cryst. Growth Des.* **2022**, *22*, 653−660.
(134) Sang, P.; Wang, Q.; Wei, W.; Wang, F.; Li, Y.; Chen, J. Semiconducting Silicene: A Two-Dimensional Silicon Allotrope with Hybrid Honeycomb-Kagome Lattice. *ACS Mater. Lett.* **2021**, *3*, 1181−1188.
(135) Prabhu, P.; Lee, J.-M. Metallenes as Functional Materials in Electrocatalysis. *Chem. Soc. Rev.* **2021**, *50*, 6700−6719.
(136) Liu, Y.; Dinh, K. N.; Dai, Z.; Yan, Q. Metallenes: Recent Advances and Opportunities in Energy Storage and Conversion Applications. *ACS Mater. Lett.* **2020**, *2*, 1148−1172.

https://doi.org/10.1021/acs.chemrev.3c00033
Chem. Rev. 2023, 123, 3493−3542

(137) Cao, C.; Xu, Q.; Zhu, Q.-L. Ultrathin Two-Dimensional Metallenes for Heterogeneous Catalysis. *Chem. Catal* **2022**, *2*, 693−723.
(138) Liu, N.; Xu, K.; Lei, Y.; Xi, Y.; Liu, Y.; Wang, N.; Wang, Y.-X.; Xu, X.; Hao, W.; Dou, S. X.; et al. Germanene Nanosheets: Achieving Superior Sodium-Ion Storage via Pseudointercalation Reactions. *Small Struct* **2021**, *2*, 2100041.
(139) Liu, N.; Bo, G.; Liu, Y.; Xu, X.; Du, Y.; Dou, S. X. Recent Progress on Germanene and Functionalized Germanene: Preparation, Characterizations, Applications, and Challenges. *Small* **2019**, *15*, 1805147.
(140) Acun, A.; Zhang, L.; Bampoulis, P.; Farmanbar, M.; van Houselt, A.; Rudenko, A. N.; Lingenfelder, M.; Brocks, G.; Poelsema, B.; Katsnelson, M. I.; Zandvliet, H. J. W. Germanene: The Germanium Analogue of Graphene. *J. Phys. Cond. Matter* **2015**, *27*, 443002.
(141) Bechstedt, F.; Gori, P.; Pulci, O. Beyond Graphene: Clean, Hydrogenated and Halogenated Silicene, Germanene, Stanene, and Plumbene. *Prog. Surf. Sci.* **2021**, *96*, 100615.
(142) Terada, T.; Uematsu, Y.; Ishibe, T.; Naruse, N.; Sato, K.; Nguyen, T. Q.; Kobayashi, E.; Nakano, H.; Nakamura, Y. Giant Enhancement of Seebeck Coefficient by Deformation of Silicene Buckled Structure in Calcium-Intercalated Layered Silicene Film. *Adv. Mater. Interfaces* **2022**, *9*, 2101752.
(143) Creighton, J. A.; Eadon, D. G. Ultraviolet−Visible Absorption Spectra of the Colloidal Metallic Elements. *J. Chem. Soc. Faraday Trans.* **1991**, *87*, 3881−3891.
(144) Maier, S. A. *Plasmonics: Fundamentals and Applications*; Springer, 2007; Vol. *1*.
(145) Kapuria, N.; Patil, N. N.; Ryan, K. M.; Singh, S. Two-Dimensional Copper Based Colloidal Nanocrystals: Synthesis and Applications. *Nanoscale* **2022**, *14*, 2885−2914.
(146) Steimle, B. C.; Fenton, J. L.; Schaak, R. E. Rational Construction of a Scalable Heterostructured Nanorod Megalibrary. *Science* **2020**, *367*, 418−424.
(147) Li, Z.; Zhai, L.; Ge, Y.; Huang, Z.; Shi, Z.; Liu, J.; Zhai, W.; Liang, J.; Zhang, H. Wet-Chemical Synthesis of Two-Dimensional Metal Nanomaterials for Electrocatalysis. *Natl. Sci. Rev.* **2022**, *9*, nwab142.
(148) Mkhitaryan, V.; March, K.; Tseng, E. N.; Li, X.; Scarabelli, L.; Liz-Marzán, L. M.; Chen, S.-Y.; Tizei, L. H. G.; Stéphan, O.; Song, J.-M.; et al. Can Copper Nanostructures Sustain High-Quality Plasmons? *Nano Lett.* **2021**, *21*, 2444−2452.
(149) Ezendam, S.; Herran, M.; Nan, L.; Gruber, C.; Kang, Y.; Gröbmeyer, F.; Lin, R.; Gargiulo, J.; Sousa-Castillo, A.; Cortés, E. Hybrid Plasmonic Nanomaterials for Hydrogen Generation and Carbon Dioxide Reduction. *ACS Energy Lett.* **2022**, *7*, 778−815.
(150) Zhang, P.; Sui, Y.; Xiao, G.; Wang, Y.; Wang, C.; Liu, B.; Zou, G.; Zou, B. Facile Fabrication of Faceted Copper Nanocrystals with High Catalytic Activity for p -Nitrophenol Reduction. *J. Mater. Chem. A* **2013**, *1*, 1632−1638.
(151) Salzemann, C.; Urban, J.; Lisiecki, I.; Pileni, M.-P. Characterization and Growth Process of Copper Nanodisks. *Adv. Funct. Mater.* **2005**, *15*, 1277−1284.
(152) Salzemann, C.; Brioude, A.; Pileni, M.-P. Tuning of Copper Nanocrystals Optical Properties with Their Shapes. *J. Phys. Chem. B* **2006**, *110*, 7208−7212.
(153) Pastoriza-Santos, I.; Sánchez-Iglesias, A.; Rodríguez-González, B.; Liz-Marzán, L. M. Aerobic Synthesis of Cu Nanoplates with Intense Plasmon Resonances. *Small* **2009**, *5*, 440−443.
(154) Park, Y. S.; Chae, H. K. Geometric Control and Intense Plasmon Resonances of Colloidal Truncated Triangular Copper Nanoplates in Nonionic Microemulsions Containing Tetrabutylammonium Hydroxide. *Chem. Mater.* **2010**, *22*, 6280−6290.
(155) Xu, S.; Sun, X.; Ye, H.; You, T.; Song, X.; Sun, S. Selective Synthesis of Copper Nanoplates and Nanowires via a Surfactant-Assisted Hydrothermal Process. *Mater. Chem. Phys.* **2010**, *120*, 1−5.
(156) Fan, N.; Xu, L.; Li, J.; Ma, X.; Qian, Y. Selective Synthesis of Plate-like and Shrub-like Micro-Scale Copper Crystallites. *J. Cryst. Growth* **2007**, *299*, 212−217.
(157) Wang, J.; Guo, X.; He, Y.; Jiang, M.; Sun, R. The Synthesis and Tribological Characteristics of Triangular Copper Nanoplates as a Grease Additive. *RSC Adv.* **2017**, *7*, 40249−40254.
(158) Shaik, A. H.; Chakraborty, J. A Simple Room Temperature Fast Reduction Technique for Preparation of a Copper Nanosheet Powder. *RSC Adv.* **2016**, *6*, 14952−14957.
(159) Lee, J.-W.; Han, J.; Lee, D. S.; Bae, S.; Lee, S. H.; Lee, S.-K.; Moon, B. J.; Choi, C.-J.; Wang, G.; Kim, T.-W. 2D Single-Crystalline Copper Nanoplates as a Conductive Filler for Electronic Ink Applications. *Small* **2018**, *14*, 1703312.
(160) Jin, M.; He, G.; Zhang, H.; Zeng, J.; Xie, Z.; Xia, Y. Shape-Controlled Synthesis of Copper Nanocrystals in an Aqueous Solution with Glucose as a Reducing Agent and Hexadecylamine as a Capping Agent. *Angew. Chem., Int. Ed.* **2011**, *50*, 10560−10564.
(161) Luc, W.; Fu, X.; Shi, J.; Lv, J.-J.; Jouny, M.; Ko, B. H.; Xu, Y.; Tu, Q.; Hu, X.; Wu, J.; et al. Two-Dimensional Copper Nanosheets for Electrochemical Reduction of Carbon Monoxide to Acetate. *Nat. Catal.* **2019**, *2*, 423−430.
(162) Wu, K.; Sun, C.; Wang, Z.; Song, Q.; Bai, X.; Yu, X.; Li, Q.; Wang, Z.; Zhang, H.; Zhang, J.; et al. Surface Reconstruction on Uniform Cu Nanodisks Boosted Electrochemical Nitrate Reduction to Ammonia. *ACS Mater. Lett.* **2022**, *4*, 650−656.
(163) Wang, Y.; Zhou, W.; Jia, R.; Yu, Y.; Zhang, B. Unveiling the Activity Origin of a Copper-Based Electrocatalyst for Selective Nitrate Reduction to Ammonia. *Angew. Chem., Int. Ed.* **2020**, *59*, 5350−5354.
(164) Chen, G.-F.; Yuan, Y.; Jiang, H.; Ren, S.-Y.; Ding, L.-X.; Ma, L.; Wu, T.; Lu, J.; Wang, H. Electrochemical Reduction of Nitrate to Ammonia via Direct Eight-Electron Transfer Using a Copper−Molecular Solid Catalyst. *Nat. Energy* **2020**, *5*, 605−613.
(165) van Langevelde, P. H.; Katsounaros, I.; Koper, M. T. M. Electrocatalytic Nitrate Reduction for Sustainable Ammonia Production. *Joule* **2021**, *5*, 290−294.
(166) Wu, Z.-Y.; Karamad, M.; Yong, X.; Huang, Q.; Cullen, D. A.; Zhu, P.; Xia, C.; Xiao, Q.; Shakouri, M.; Chen, F.-Y.; et al. Electrochemical Ammonia Synthesis via Nitrate Reduction on Fe Single Atom Catalyst. *Nat. Commun.* **2021**, *12*, 2870.
(167) Bianchini, C.; Shen, P. K. Palladium-Based Electrocatalysts for Alcohol Oxidation in Half Cells and in Direct Alcohol Fuel Cells. *Chem. Rev.* **2009**, *109*, 4183−4206.
(168) Konda, S. K.; Chen, A. Palladium Based Nanomaterials for Enhanced Hydrogen Spillover and Storage. *Mater. Today* **2016**, *19*, 100−108.
(169) Yin; Liebscher, J. Carbon−Carbon Coupling Reactions Catalyzed by Heterogeneous Palladium Catalysts. *Chem. Rev.* **2007**, *107*, 133−173.
(170) Nguyen, Q. N.; Chen, R.; Lyu, Z.; Xia, Y. Using Reduction Kinetics to Control and Predict the Outcome of a Colloidal Synthesis of Noble-Metal Nanocrystals. *Inorg. Chem.* **2021**, *60*, 4182−4197.
(171) Xiong, Y.; McLellan, J. M.; Chen, J.; Yin, Y.; Li, Z.-Y.; Xia, Y. Kinetically Controlled Synthesis of Triangular and Hexagonal Nanoplates of Palladium and Their SPR/SERS Properties. *J. Am. Chem. Soc.* **2005**, *127*, 17118−17127.
(172) Xiong, Y.; Washio, I.; Chen, J.; Cai, H.; Li, Z.-Y.; Xia, Y. Poly(Vinyl Pyrrolidone): A Dual Functional Reductant and Stabilizer for the Facile Synthesis of Noble Metal Nanoplates in Aqueous Solutions. *Langmuir* **2006**, *22*, 8563−8570.
(173) Trinh, T. T.; Sato, R.; Sakamoto, M.; Fujiyoshi, Y.; Haruta, M.; Kurata, H.; Teranishi, T. Visible to Near-Infrared Plasmon-Enhanced Catalytic Activity of Pd Hexagonal Nanoplates for the Suzuki Coupling Reaction. *Nanoscale* **2015**, *7*, 12435−12444.
(174) Jin, M.; Zhang, H.; Xie, Z.; Xia, Y. Palladium Nanocrystals Enclosed by {100} and {111} Facets in Controlled Proportions and Their Catalytic Activities for Formic Acid Oxidation. *Energy Environ. Sci.* **2012**, *5*, 6352−6357.
(175) Peng, H.-C.; Xie, S.; Park, J.; Xia, X.; Xia, Y. Quantitative Analysis of the Coverage Density of Br− Ions on Pd{100} Facets and Its Role in Controlling the Shape of Pd Nanocrystals. *J. Am. Chem. Soc.* **2013**, *135*, 3780−3783.

https://doi.org/10.1021/acs.chemrev.3c00033
Chem. Rev. 2023, 123, 3493−3542

(176) Zhang, H.-X.; Wang, H.; Re, Y.-S.; Cai, W.-B. Palladium Nanocrystals Bound by {110} or {100} Facets: From One Pot Synthesis to Electrochemistry. *Chem. Commun.* **2012**, *48*, 8362−8364.
(177) Huang, X.; Zheng, N. One-Pot, High-Yield Synthesis of 5-Fold Twinned Pd Nanowires and Nanorods. *J. Am. Chem. Soc.* **2009**, *131*, 4602−4603.
(178) Wang, C.; Wang, L.; Long, R.; Ma, L.; Wang, L.; Li, Z.; Xiong, Y. Anisotropic Growth of Palladium Twinned Nanostructures Controlled by Kinetics and Their Unusual Activities in Galvanic Replacement. *J. Mater. Chem.* **2012**, *22*, 8195−8198.
(179) Vitos, L.; Ruban, A. V.; Skriver, H. L.; Kollár, J. The Surface Energy of Metals. *Surf. Sci.* **1998**, *411*, 186−202.
(180) Kuhn, W. K.; Szanyi, J.; Goodman, D. W. CO Adsorption on Pd(111): The Effects of Temperature and Pressure. *Surf. Sci.* **1992**, *274*, L611−L618.
(181) Li, H.; Chen, G.; Yang, H.; Wang, X.; Liang, J.; Liu, P.; Chen, M.; Zheng, N. Shape-Controlled Synthesis of Surface-Clean Ultrathin Palladium Nanosheets by Simply Mixing a Dinuclear PdI Carbonyl Chloride Complex with H_2O. *Angew. Chem., Int. Ed.* **2013**, *52*, 8368−8372.
(182) Li, Y.; Yan, Y.; Li, Y.; Zhang, H.; Li, D.; Yang, D. Size-Controlled Synthesis of Pd Nanosheets for Tunable Plasmonic Properties. *CrystEngComm* **2015**, *17*, 1833−1838.
(183) Zhang, H.; Jin, M.; Xiong, Y.; Lim, B.; Xia, Y. Shape-Controlled Synthesis of Pd Nanocrystals and Their Catalytic Applications. *Acc. Chem. Res.* **2013**, *46*, 1783−1794.
(184) Wang, H.; He, X.; Zhao, Y.; Li, J.; Huang, T.; Liu, H. Facile Synthesis of Self-Assemblies of Ultrathin Round Pd Nanosheets or Nanorings and Their Enhanced Electrocatalytic Activities. *CrystEngComm* **2017**, *19*, 4304−4311.
(185) Yin, X.; Shi, M.; Kwok, K. S.; Zhao, H.; Gray, D. L.; Bertke, J. A.; Yang, H. Dish-like Higher-Ordered Palladium Nanostructures through Metal Ion-Ligand Complexation. *Nano Res.* **2018**, *11*, 3442−3452.
(186) Li, Y.; Wang, W.; Xia, K.; Zhang, W.; Jiang, Y.; Zeng, Y.; Zhang, H.; Jin, C.; Zhang, Z.; Yang, D. Ultrathin Two-Dimensional Pd-Based Nanorings as Catalysts for Hydrogenation with High Activity and Stability. *Small* **2015**, *11*, 4745−4752.
(187) Huang, X.; Tang, S.; Yang, J.; Tan, Y.; Zheng, N. Etching Growth under Surface Confinement: An Effective Strategy To Prepare Mesocrystalline Pd Nanocorolla. *J. Am. Chem. Soc.* **2011**, *133*, 15946−15949.
(188) Zhang, Y.; Wang, M.; Zhu, E.; Zheng, Y.; Huang, Y.; Huang, X. Seedless Growth of Palladium Nanocrystals with Tunable Structures: From Tetrahedra to Nanosheets. *Nano Lett.* **2015**, *15*, 7519−7525.
(189) Bratlie, K. M.; Lee, H.; Komvopoulos, K.; Yang, P.; Somorjai, G. A. Platinum Nanoparticle Shape Effects on Benzene Hydrogenation Selectivity. *Nano Lett.* **2007**, *7*, 3097−3101.
(190) Bratlie, K. M.; Montano, M. O.; Flores, L. D.; Paajanen, M.; Somorjai, G. A. Sum Frequency Generation Vibrational Spectroscopic and High-Pressure Scanning Tunneling Microscopic Studies of Benzene Hydrogenation on Pt(111). *J. Am. Chem. Soc.* **2006**, *128*, 12810−12816.
(191) Shi, Y.; Lyu, Z.; Zhao, M.; Chen, R.; Nguyen, Q. N.; Xia, Y. Noble-Metal Nanocrystals with Controlled Shapes for Catalytic and Electrocatalytic Applications. *Chem. Rev.* **2021**, *121*, 649−735.
(192) Wang, C.; Daimon, H.; Onodera, T.; Koda, T.; Sun, S. A General Approach to the Size- and Shape-Controlled Synthesis of Platinum Nanoparticles and Their Catalytic Reduction of Oxygen. *Angew. Chem.* **2008**, *120*, 3644−3647.
(193) Ahmadi, T. S.; Wang, Z. L.; Green, T. C.; Henglein, A.; El-Sayed, M. A. Shape-Controlled Synthesis of Colloidal Platinum Nanoparticles. *Science* **1996**, *272*, 1924−1925.
(194) Herricks, T.; Chen, J.; Xia, Y. Polyol Synthesis of Platinum Nanoparticles: Control of Morphology with Sodium Nitrate. *Nano Lett.* **2004**, *4*, 2367−2371.
(195) Zhao, S.-Y.; Chen, S.-H.; Wang, S.-Y.; Li, D.-G.; Ma, H.-Y. Preparation, Phase Transfer, and Self-Assembled Monolayers of Cubic Pt Nanoparticles. *Langmuir* **2002**, *18*, 3315−3318.
(196) Petroski, J. M.; Wang, Z. L.; Green, T. C.; El-Sayed, M. A. Kinetically Controlled Growth and Shape Formation Mechanism of Platinum Nanoparticles. *J. Phys. Chem. B* **1998**, *102*, 3316−3320.
(197) Cheong, S.; Watt, J.; Ingham, B.; Toney, M. F.; Tilley, R. D. In Situ and Ex Situ Studies of Platinum Nanocrystals: Growth and Evolution in Solution. *J. Am. Chem. Soc.* **2009**, *131*, 14590−14595.
(198) Chen, J.; Herricks, T.; Xia, Y. Polyol Synthesis of Platinum Nanostructures: Control of Morphology through the Manipulation of Reduction Kinetics. *Angew. Chem., Int. Ed.* **2005**, *44*, 2589−2592.
(199) Zhong, X.; Feng, Y.; Lieberwirth, I.; Knoll, W. Facile Synthesis of Morphology-Controlled Platinum Nanocrystals. *Chem. Mater.* **2006**, *18*, 2468−2471.
(200) Michel, J. A.; Morris, W. H., III; Lukehart, C. M. Synthesis of Shaped Pt Nanoparticles Using Common Anions or Small Molecules as Shape-Directing Agents: Observation of a Strong Halide or Pseudo-Halide Effect. *J. Mater. Chem. A* **2015**, *3*, 2012−2018.
(201) Yin, J.; Wang, J.; Li, M.; Jin, C.; Zhang, T. Iodine Ions Mediated Formation of Monomorphic Single-Crystalline Platinum Nanoflowers. *Chem. Mater.* **2012**, *24*, 2645−2654.
(202) Yamada, M.; Kon, S.; Miyake, M. Synthesis and Size Control of Pt Nanocubes with High Selectivity Using the Additive Effect of NaI. *Chem. Lett.* **2005**, *34*, 1050−1051.
(203) Lim, B.; Wang, J.; Camargo, P. H. C.; Jiang, M.; Kim, M. J.; Xia, Y. Facile Synthesis of Bimetallic Nanoplates Consisting of Pd Cores and Pt Shells through Seeded Epitaxial Growth. *Nano Lett.* **2008**, *8*, 2535−2540.
(204) Shirai, M.; Igeta, K.; Arai, M. Formation of Platinum Nanosheets between Graphite Layers. *Chem. Commun.* **2000**, 623−624.
(205) Kijima, T.; Nagatomo, Y.; Takemoto, H.; Uota, M.; Fujikawa, D.; Sekiya, Y.; Kishishita, T.; Shimoda, M.; Yoshimura, T.; Kawasaki, H.; et al. Synthesis of Nanohole-Structured Single-Crystalline Platinum Nanosheets Using Surfactant-Liquid-Crystals and Their Electrochemical Characterization. *Adv. Funct. Mater.* **2009**, *19*, 545−553.
(206) Chen, Y.; Fan, Z.; Zhang, Z.; Niu, W.; Li, C.; Yang, N.; Chen, B.; Zhang, H. Two-Dimensional Metal Nanomaterials: Synthesis, Properties, and Applications. *Chem. Rev.* **2018**, *118*, 6409−6455.
(207) Chen, S.; Kimura, K. Synthesis of Thiolate-Stabilized Platinum Nanoparticles in Protolytic Solvents as Isolable Colloids. *J. Phys. Chem. B* **2001**, *105*, 5397−5403.
(208) Xia, Y.; Xiong, Y.; Lim, B.; Skrabalak, S. E. Shape-Controlled Synthesis of Metal Nanocrystals: Simple Chemistry Meets Complex Physics? *Angew. Chem., Int. Ed.* **2009**, *48*, 60−103.
(209) Maksimuk, S.; Teng, X.; Yang, H. Planar Tripods of Platinum: Formation and Self-Assembly. *Phys. Chem. Chem. Phys.* **2006**, *8*, 4660−4663.
(210) Ren, J.; Tilley, R. D. Shape-Controlled Growth of Platinum Nanoparticles. *Small* **2007**, *3*, 1508−1512.
(211) Maksimuk, S.; Teng, X.; Yang, H. Roles of Twin Defects in the Formation of Platinum Multipod Nanocrystals. *J. Phys. Chem. C* **2007**, *111*, 14312−14319.
(212) Lacroix, L.-M.; Gatel, C.; Arenal, R.; Garcia, C.; Lachaize, S.; Blon, T.; Warot-Fonrose, B.; Snoeck, E.; Chaudret, B.; Viau, G. Tuning Complex Shapes in Platinum Nanoparticles: From Cubic Dendrites to Fivefold Stars. *Angew. Chem., Int. Ed.* **2012**, *51*, 4690−4694.
(213) Cao, B.; Zeng, L.; Liu, H.; Shang, J.; Wang, L.; Lang, J.; Cao, X.; Gu, H. Synthesis of the Platinum Nanoribbons Regulated by Fluorine and Applications in Electrocatalysis. *Inorg. Chem.* **2021**, *60*, 4366−4370.
(214) Viswanath, B.; Kundu, P.; Halder, A.; Ravishankar, N. Mechanistic Aspects of Shape Selection and Symmetry Breaking during Nanostructure Growth by Wet Chemical Methods. *J. Phys. Chem. C* **2009**, *113*, 16866−16883.
(215) Viswanath, B.; Kundu, P.; Mukherjee, B.; Ravishankar, N. Predicting the Growth of Two-Dimensional Nanostructures. *Nanotechnology* **2008**, *19*, 195603.
(216) Viswanath, B.; Kundu, P.; Ravishankar, N. Formation of Two-Dimensional Structures by Tuning the Driving Force of Chemical

https://doi.org/10.1021/acs.chemrev.3c00033
Chem. Rev. 2023, 123, 3493−3542

Reactions: An Interpretation of Kinetic Control. *J. Colloid Interface Sci.* **2009**, *330*, 211−219.
(217) Ruan, L.; Chiu, C.-Y.; Li, Y.; Huang, Y. Synthesis of Platinum Single-Twinned Right Bipyramid and {111}-Bipyramid through Targeted Control over Both Nucleation and Growth Using Specific Peptides. *Nano Lett.* **2011**, *11*, 3040−3046.
(218) Briggs, B. D.; Knecht, M. R. Nanotechnology Meets Biology: Peptide-Based Methods for the Fabrication of Functional Materials. *J. Phys. Chem. Lett.* **2012**, *3*, 405−418.
(219) Chen, R.; Shi, Y.; Xie, M.; Xia, Y. Facile Synthesis of Platinum Right Bipyramids by Separating and Controlling the Nucleation Step in a Continuous Flow System. *Chem.−Eur. J.* **2021**, *27*, 13855−13863.
(220) Mahata, N.; Cunha, A. F.; Órfão, J. J. M.; Figueiredo, J. L. Hydrogenation of Chloronitrobenzenes over Filamentous Carbon Stabilized Nickel Nanoparticles. *Catal. Commun.* **2009**, *10*, 1203−1206.
(221) Metin, Ö.; Özkar, S. Hydrogen Generation from the Hydrolysis of Sodium Borohydride by Using Water Dispersible, Hydrogenphosphate-Stabilized Nickel(0) Nanoclusters as Catalyst. *Int. J. Hydrog. Energy* **2007**, *32*, 1707−1715.
(222) Sehested, J. Four Challenges for Nickel Steam-Reforming Catalysts. *Catal. Today* **2006**, *111*, 103−110.
(223) Gong, M.; Wang, D.-Y.; Chen, C.-C.; Hwang, B.-J.; Dai, H. A Mini Review on Nickel-Based Electrocatalysts for Alkaline Hydrogen Evolution Reaction. *Nano Res.* **2016**, *9*, 28−46.
(224) Leng, Y.; Zheng, J.; Qu, J.; Li, X. Thermal Stability and Magnetic Anisotropy of Nickel Nanoplates. *J. Mater. Sci.* **2009**, *44*, 4599−4603.
(225) Leng, Y.; Wang, Y.; Li, X.; Liu, T.; Takahashhi, S. Controlled Synthesis of Triangular and Hexagonal Ni Nanosheets and Their Size-Dependent Properties. *Nanotechnology* **2006**, *17*, 4834−4839.
(226) Wang, Z.; Chen, Y.; Zeng, D.; Zhang, Q.; Peng, D.-L. Solution Synthesis of Triangular and Hexagonal Nickel Nanosheets with the Aid of Tungsten Hexacarbonyl. *CrystEngComm* **2016**, *18*, 1295−1301.
(227) Lagrow, A. P.; Alyami, N. M.; Lloyd, D. C.; Bakr, O. M.; Boyes, E. D.; Gai, P. L. In Situ Oxidation and Reduction of Triangular Nickel Nanoplates via Environmental Transmission Electron Microscopy. *J. Microsc.* **2018**, *269*, 161−167.
(228) LaGrow, A. P.; Ingham, B.; Cheong, S.; Williams, G. V. M.; Dotzler, C.; Toney, M. F.; Jefferson, D. A.; Corbos, E. C.; Bishop, P. T.; Cookson, J.; et al. Synthesis, Alignment, and Magnetic Properties of Monodisperse Nickel Nanocubes. *J. Am. Chem. Soc.* **2012**, *134*, 855−858.
(229) Xu, R.; Xie, T.; Zhao, Y.; Li, Y. Single-Crystal Metal Nanoplatelets: Cobalt, Nickel, Copper, and Silver. *Cryst. Growth Des.* **2007**, *7*, 1904−1911.
(230) Xiao, L.; Zhou, T.; Chen, Y.; Wang, Z.; Zheng, H.; Xu, W.; Zeng, D.; Peng, D.-L. Tungsten Hexacarbonyl-Induced Growth of Nickel Nanorods and Nanocubes. *Mater. Lett.* **2018**, *229*, 340−343.
(231) Shviro, M.; Zitoun, D. Nickel Nanocrystals: Fast Synthesis of Cubes, Pyramids and Tetrapods. *RSC Adv.* **2013**, *3*, 1380−1387.
(232) Cordente, N.; Respaud, M.; Senocq, F.; Casanove, M.-J.; Amiens, C.; Chaudret, B. Synthesis and Magnetic Properties of Nickel Nanorods. *Nano Lett.* **2001**, *1*, 565−568.
(233) Mourdikoudis, S.; Collière, V.; Amiens, C.; Fau, P.; Kahn, M. L. Metal−Organic Pathways for Anisotropic Growth of a Highly Symmetrical Crystal Structure: Example of the Fcc Ni. *Langmuir* **2013**, *29*, 13491−13501.
(234) Chen, Y.; Peng, D.-L.; Lin, D.; Luo, X. Preparation and Magnetic Properties of Nickel Nanoparticles via the Thermal Decomposition of Nickel Organometallic Precursor in Alkylamines. *Nanotechnology* **2007**, *18*, 505703.
(235) Luo, X.; Chen, Y.; Yue, G.-H.; Peng, D.-L.; Luo, X. Preparation of Hexagonal Close-Packed Nickel Nanoparticles via a Thermal Decomposition Approach Using Nickel Acetate Tetrahydrate as a Precursor. *J. Alloys Compd.* **2009**, *476*, 864−868.
(236) Bradley, J. S.; Tesche, B.; Busser, W.; Maase, M.; Reetz, M. T. Surface Spectroscopic Study of the Stabilization Mechanism for Shape-Selectively Synthesized Nanostructured Transition Metal Colloids. *J. Am. Chem. Soc.* **2000**, *122*, 4631−4636.
(237) Leng, Y.; Zhang, Y.; Liu, T.; Suzuki, M.; Li, X. Synthesis of Single Crystalline Triangular and Hexagonal Ni Nanosheets with Enhanced Magnetic Properties. *Nanotechnology* **2006**, *17*, 1797−1800.
(238) Leng, Y.; Wang, Y.; Li, X.; Liu, T.; Takahashhi, S. Controlled Synthesis of Triangular and Hexagonal Ni Nanosheets and Their Size-Dependent Properties. *Nanotechnology* **2006**, *17*, 4834−4839.
(239) Leng, Y.; Li, Y.; Li, X.; Takahashi, S. Improved Magnetic Anisotropy of Monodispersed Triangular Nickel Nanoplates. *J. Phys. Chem. C* **2007**, *111*, 6630−6633.
(240) Guo, H.; Chen, Y.; Ping, H.; Wang, L.; Peng, D.-L. One-Pot Synthesis of Hexagonal and Triangular Nickel−Copper Alloy Nanoplates and Their Magnetic and Catalytic Properties. *J. Mater. Chem.* **2012**, *22*, 8336−8344.
(241) Hwang, H.; Kwon, T.; Kim, H. Y.; Park, J.; Oh, A.; Kim, B.; Baik, H.; Joo, S. H.; Lee, K. Ni@Ru and NiCo@Ru Core−Shell Hexagonal Nanosandwiches with a Compositionally Tunable Core and a Regioselectively Grown Shell. *Small* **2018**, *14*, 1702353.
(242) Akao, A.; Sato, K.; Nonoyama, N.; Mase, T.; Yasuda, N. Highly Chemoselective Reduction Using a Rh/C−$Fe(OAc)_2$ System: Practical Synthesis of Functionalized Indoles. *Tetrahedron Lett.* **2006**, *47*, 969−972.
(243) Pellegatta, J.-L.; Blandy, C.; Collière, V.; Choukroun, R.; Chaudret, B.; Cheng, P.; Philippot, K. Catalytic Investigation of Rhodium Nanoparticles in Hydrogenation of Benzene and Phenylacetylene. *J. Mol. Catal. Chem.* **2002**, *178*, 55−61.
(244) Zhou, Z.-Y.; Tian, N.; Li, J.-T.; Broadwell, I.; Sun, S.-G. Nanomaterials of High Surface Energy with Exceptional Properties in Catalysis and Energy Storage. *Chem. Soc. Rev.* **2011**, *40*, 4167−4185.
(245) Grass, M. E.; Zhang, Y.; Butcher, D. R.; Park, J. Y.; Li, Y.; Bluhm, H.; Bratlie, K. M.; Zhang, T.; Somorjai, G. A. A Reactive Oxide Overlayer on Rhodium Nanoparticles during CO Oxidation and Its Size Dependence Studied by In Situ Ambient-Pressure X-Ray Photoelectron Spectroscopy. *Angew. Chem., Int. Ed.* **2008**, *47*, 8893−8896.
(246) Cimpeanu, V.; Kočevar, M.; Parvulescu, V. I.; Leitner, W. Preparation of Rhodium Nanoparticles in Carbon Dioxide Induced Ionic Liquids and Their Application to Selective Hydrogenation. *Angew. Chem.* **2009**, *121*, 1105−1108.
(247) McClure, S. M.; Lundwall, M. J.; Goodman, D. W. Planar Oxide Supported Rhodium Nanoparticles as Model Catalysts. *Proc. Natl. Acad. Sci. U. S. A.* **2011**, *108*, 931−936.
(248) Kanuru, V. K.; Humphrey, S. M.; Kyffin, J. M. W.; Jefferson, D. A.; Burton, J. W.; Armbruster, M.; Lambert, R. M. Evidence for Heterogeneous Sonogashira Coupling of Phenylacetylene and Iodobenzene Catalyzed by Well Defined Rhodium Nanoparticles. *Dalton Trans* **2009**, *2009*, 7602−7605.
(249) Gandhi, H. S.; Graham, G. W.; McCabe, R. W. Automotive Exhaust Catalysis. *J. Catal.* **2003**, *216*, 433−442.
(250) Yu, N.-F.; Tian, N.; Zhou, Z.-Y.; Huang, L.; Xiao, J.; Wen, Y.-H.; Sun, S.-G. Electrochemical Synthesis of Tetrahexahedral Rhodium Nanocrystals with Extraordinarily High Surface Energy and High Electrocatalytic Activity. *Angew. Chem., Int. Ed.* **2014**, *53*, 5097−5101.
(251) Park, K. H.; Jang, K.; Kim, H. J.; Son, S. U. Near-Monodisperse Tetrahedral Rhodium Nanoparticles on Charcoal: The Shape-Dependent Catalytic Hydrogenation of Arenes. *Angew. Chem., Int. Ed.* **2007**, *46*, 1152−1155.
(252) Humphrey, S. M.; Grass, M. E.; Habas, S. E.; Niesz, K.; Somorjai, G. A.; Tilley, T. D. Rhodium Nanoparticles from Cluster Seeds: Control of Size and Shape by Precursor Addition Rate. *Nano Lett.* **2007**, *7*, 785−790.
(253) Zhang, Y.; Grass, M. E.; Habas, S. E.; Tao, F.; Zhang, T.; Yang, P.; Somorjai, G. A. One-Step Polyol Synthesis and Langmuir−Blodgett Monolayer Formation of Size-Tunable Monodisperse Rhodium Nanocrystals with Catalytically Active (111) Surface Structures. *J. Phys. Chem. C* **2007**, *111*, 12243−12253.
(254) Zettsu, N.; McLellan, J. M.; Wiley, B.; Yin, Y.; Li, Z.-Y.; Xia, Y. Synthesis, Stability, and Surface Plasmonic Properties of Rhodium Multipods, and Their Use as Substrates for Surface-Enhanced Raman Scattering. *Angew. Chem., Int. Ed.* **2006**, *45*, 1288−1292.

https://doi.org/10.1021/acs.chemrev.3c00033
Chem. Rev. 2023, 123, 3493−3542

(255) Zhang, Y.; Grass, M. E.; Huang, W.; Somorjai, G. A. Seedless Polyol Synthesis and CO Oxidation Activity of Monodisperse (111)- and (100)-Oriented Rhodium Nanocrystals in Sub-10 nm Sizes. *Langmuir* **2010**, *26*, 16463−16468.
(256) Biacchi, A. J.; Schaak, R. E. The Solvent Matters: Kinetic versus Thermodynamic Shape Control in the Polyol Synthesis of Rhodium Nanoparticles. *ACS Nano* **2011**, *5*, 8089−8099.
(257) Jang, K.; Kim, H. J.; Son, S. U. Low-Temperature Synthesis of Ultrathin Rhodium Nanoplates via Molecular Orbital Symmetry Interaction between Rhodium Precursors. *Chem. Mater.* **2010**, *22*, 1273−1275.
(258) Zhang, N.; Shao, Q.; Pi, Y.; Guo, J.; Huang, X. Solvent-Mediated Shape Tuning of Well-Defined Rhodium Nanocrystals for Efficient Electrochemical Water Splitting. *Chem. Mater.* **2017**, *29*, 5009−5015.
(259) Zhao, L.; Xu, C.; Su, H.; Liang, J.; Lin, S.; Gu, L.; Wang, X.; Chen, M.; Zheng, N. Single-Crystalline Rhodium Nanosheets with Atomic Thickness. *Adv. Sci.* **2015**, *2*, 1500100.
(260) Hou, C.; Zhu, J.; Liu, C.; Wang, X.; Kuang, Q.; Zheng, L. Formaldehyde-Assisted Synthesis of Ultrathin Rh Nanosheets for Applications in CO Oxidation. *CrystEngComm* **2013**, *15*, 6127−6130.
(261) Zhang, J.; Chen, M.; Chen, J.; Li, H.; Wang, S.; Kuang, Q.; Cao, Z.; Xie, Z. Synthesis of Single-Crystal Hyperbranched Rhodium Nanoplates with Remarkable Catalytic Properties. *Sci. China Mater.* **2017**, *60*, 685−696.
(262) Duan, H.; Yan, N.; Yu, R.; Chang, C.-R.; Zhou, G.; Hu, H.-S.; Rong, H.; Niu, Z.; Mao, J.; Asakura, H.; et al. Ultrathin Rhodium Nanosheets. *Nat. Commun.* **2014**, *5*, 3093.
(263) Knight, M. W.; King, N. S.; Liu, L.; Everitt, H. O.; Nordlander, P.; Halas, N. J. Aluminum for Plasmonics. *ACS Nano* **2014**, *8*, 834−840.
(264) Jacobson, C. R.; Solti, D.; Renard, D.; Yuan, L.; Lou, M.; Halas, N. J. Shining Light on Aluminum Nanoparticle Synthesis. *Acc. Chem. Res.* **2020**, *53*, 2020−2030.
(265) Jacobson, C. R.; Wu, G.; Alemany, L. B.; Naidu, G. N.; Lou, M.; Yuan, Y.; Bayles, A.; Clark, B. D.; Cheng, Y.; Ali, A.; et al. A Dual Catalyst Strategy for Controlling Aluminum Nanocrystal Growth. *Nano Lett.* **2022**, *22*, 5570−5574.
(266) Castilla, M.; Schuermans, S.; Gérard, D.; Martin, J.; Maurer, T.; Hananel, U.; Markovich, G.; Plain, J.; Proust, J. Colloidal Synthesis of Crystalline Aluminum Nanoparticles for UV Plasmonics. *ACS Photonics* **2022**, *9*, 880−887.
(267) Clark, B. D.; Jacobson, C. R.; Lou, M.; Yang, J.; Zhou, L.; Gottheim, S.; DeSantis, C. J.; Nordlander, P.; Halas, N. J. Aluminum Nanorods. *Nano Lett.* **2018**, *18*, 1234−1240.
(268) Riegsinger, S.; Popescu, R.; Gerthsen, D.; Feldmann, C. Room-Temperature Liquid-Phase Synthesis of Aluminium Nanoparticles. *Chem. Commun.* **2022**, *58*, 7499−7502.
(269) Clark, B. D.; DeSantis, C. J.; Wu, G.; Renard, D.; McClain, M. J.; Bursi, L.; Tsai, A.-L.; Nordlander, P.; Halas, N. J. Ligand-Dependent Colloidal Stability Controls the Growth of Aluminum Nanocrystals. *J. Am. Chem. Soc.* **2019**, *141*, 1716−1724.
(270) McClain, M. J.; Schlather, A. E.; Ringe, E.; King, N. S.; Liu, L.; Manjavacas, A.; Knight, M. W.; Kumar, I.; Whitmire, K. H.; Everitt, H. O.; et al. Aluminum Nanocrystals. *Nano Lett.* **2015**, *15*, 2751−2755.
(271) Barulin, A.; Claude, J.-B.; Patra, S.; Moreau, A.; Lumeau, J.; Wenger, J. Preventing Aluminum Photocorrosion for Ultraviolet Plasmonics. *J. Phys. Chem. Lett.* **2019**, *10*, 5700−5707.
(272) Cui, M.-L.; Chen, Y.-S.; Xie, Q.-F.; Yang, D.-P.; Han, M.-Y. Synthesis, Properties and Applications of Noble Metal Iridium Nanomaterials. *Coord. Chem. Rev.* **2019**, *387*, 450−462.
(273) Hu, H.; Xin, J. H.; Hu, H.; Wang, X.; Miao, D.; Liu, Y. Synthesis and Stabilization of Metal Nanocatalysts for Reduction Reactions − a Review. *J. Mater. Chem. A* **2015**, *3*, 11157−11182.
(274) Xu, D.; Diao, P.; Jin, T.; Wu, Q.; Liu, X.; Guo, X.; Gong, H.; Li, F.; Xiang, M.; Ronghai, Y. Iridium Oxide Nanoparticles and Iridium/Iridium Oxide Nanocomposites: Photochemical Fabrication and Application in Catalytic Reduction of 4-Nitrophenol. *ACS Appl. Mater. Interfaces* **2015**, *7*, 16738−16749.
(275) Cano, I.; Tschan, M. J.-L.; Martinez-Prieto, L. M.; Philippot, K.; Chaudret, B.; van Leeuwen, P. W. N. M. Enantioselective Hydrogenation of Ketones by Iridium Nanoparticles Ligated with Chiral Secondary Phosphine Oxides. *Catal. Sci. Technol.* **2016**, *6*, 3758−3766.
(276) Scholten, J. D. From Soluble to Supported Iridium Metal Nanoparticles: Active and Recyclable Catalysts for Hydrogenation Reactions. *Curr. Org. Chem.* **2013**, *17*, 348−363.
(277) Lu, T.; Wei, H.; Yang, X.; Li, J.; Wang, X.; Zhang, T. Microemulsion-Controlled Synthesis of One-Dimensional Ir Nanowires and Their Catalytic Activity in Selective Hydrogenation of o-Chloronitrobenzene. *Langmuir* **2015**, *31*, 90−95.
(278) Cui, M.; Zhou, J.; Zhao, Y.; Song, Q. Facile Synthesis of Iridium Nanoparticles with Superior Peroxidase-like Activity for Colorimetric Determination of H2O2 and Xanthine. *Sens. Actuators B Chem.* **2017**, *243*, 203−210.
(279) Su, H.; Liu, D.-D.; Zhao, M.; Hu, W.-L.; Xue, S.-S.; Cao, Q.; Le, X.-Y.; Ji, L.-N.; Mao, Z.-W. Dual-Enzyme Characteristics of Polyvinylpyrrolidone-Capped Iridium Nanoparticles and Their Cellular Protective Effect against H_2O_2-Induced Oxidative Damage. *ACS Appl. Mater. Interfaces* **2015**, *7*, 8233−8242.
(280) Jin, G.; Liu, J.; Wang, C.; Gu, W.; Ran, G.; Liu, B.; Song, Q. Ir Nanoparticles with Multi-Enzyme Activities and Its Application in the Selective Oxidation of Aromatic Alcohols. *Appl. Catal. B Environ.* **2020**, *267*, 118725.
(281) Wang, X.; Hu, Y.; Wei, H. Nanozymes in Bionanotechnology: From Sensing to Therapeutics and Beyond. *Inorg. Chem. Front.* **2016**, *3*, 41−60.
(282) Feng, L.; Dong, Z.; Liang, C.; Chen, M.; Tao, D.; Cheng, L.; Yang, K.; Liu, Z. Iridium Nanocrystals Encapsulated Liposomes as Near-Infrared Light Controllable Nanozymes for Enhanced Cancer Radiotherapy. *Biomaterials* **2018**, *181*, 81−91.
(283) Chakrapani, K.; Sampath, S. Spontaneous Assembly of Iridium Nanochain-like Structures: Surface Enhanced Raman Scattering Activity Using Visible Light. *Chem. Commun.* **2014**, *50*, 3061−3063.
(284) Sakthikumar, K.; Anantharaj, S.; Ede, S. R.; Karthick, K.; Ravi, G.; Karthik, T.; Kundu, S. Prompt Synthesis of Iridium Organosol on DNA for Catalysis and SERS Applications. *J. Mater. Chem. C* **2017**, *5*, 11947−11957.
(285) Kang, G.; Matikainen, A.; Stenberg, P.; Färm, E.; Li, P.; Ritala, M.; Vahimaa, P.; Honkanen, S.; Tan, X. High Aspect-Ratio Iridium-Coated Nanopillars for Highly Reproducible Surface-Enhanced Raman Scattering (SERS). *ACS Appl. Mater. Interfaces* **2015**, *7*, 11452−11459.
(286) Cui, M.; Wang, C.; Yang, D.; Song, Q. Fluorescent Iridium Nanoclusters for Selective Determination of Chromium(VI). *Microchim. Acta* **2018**, *185*, 8.
(287) Vankayala, R.; Gollavelli, G.; Mandal, B. K. Highly Fluorescent and Biocompatible Iridium Nanoclusters for Cellular Imaging. *J. Mater. Sci. Mater. Med.* **2013**, *24*, 1993−2000.
(288) Cui, M.; Zhao, Y.; Wang, C.; Song, Q. Synthesis of 2.5 nm Colloidal Iridium Nanoparticles with Strong Surface Enhanced Raman Scattering Activity. *Microchim. Acta* **2016**, *183*, 2047−2053.
(289) Kundu, S.; Liang, H. Shape-Selective Formation and Characterization of Catalytically Active Iridium Nanoparticles. *J. Colloid Interface Sci.* **2011**, *354*, 597−606.
(290) Cheng, Z.; Huang, B.; Pi, Y.; Li, L.; Shao, Q.; Huang, X. Partially Hydroxylated Ultrathin Iridium Nanosheets as Efficient Electrocatalysts for Water Splitting. *Natl. Sci. Rev.* **2020**, *7*, 1340−1348.
(291) Assaf, N. W.; Suleiman, I. A.; Shawaqfeh, A. T. The Surface Energy Phase Diagrams of CO Adsorption on the Low Index Iridium Surfaces and the Morphology of Iridium Nanoparticles. *J. Cryst. Growth* **2022**, *593*, 126774.
(292) Liu, C.; Zhu, L.; Ren, P.; Wen, X.; Li, Y.-W.; Jiao, H. High-Coverage CO Adsorption and Dissociation on Ir(111), Ir(100), and Ir(110) from Computations. *J. Phys. Chem. C* **2019**, *123*, 6487−6495.
(293) Christmann, K.; Ertl, G. Interactions of CO and O2 with Ir(110)Surfaces. *Z. Für Naturforschung A* **1973**, *28*, 1144−1148b.
(294) Nabais, C.; Schneider, R.; Bellouard, C.; Lambert, J.; Willmann, P.; Billaud, D. A New Method for the Size- and Shape-Controlled

https://doi.org/10.1021/acs.chemrev.3c00033
Chem. Rev. 2023, 123, 3493−3542

Synthesis of Lead Nanostructures. *Mater. Chem. Phys.* **2009**, *117*, 268−275.
(295) Resa, I.; Moreira, H.; Bresson, B.; Mahler, B.; Dubertret, B.; Aubin, H. Synthesis of Monodisperse Superconducting Lead Nanocrystals. *J. Phys. Chem. C* **2009**, *113*, 7120−7122.
(296) Wang, Y.; Cai, L.; Xia, Y. Monodisperse Spherical Colloids of Pb and Their Use as Chemical Templates to Produce Hollow Particles. *Adv. Mater.* **2005**, *17*, 473−477.
(297) Wang, Y.; Jiang, X.; Herricks, T.; Xia, Y. Single Crystalline Nanowires of Lead: Large-Scale Synthesis, Mechanistic Studies, and Transport Measurements. *J. Phys. Chem. B* **2004**, *108*, 8631−8640.
(298) Lu, X. L.; Wang, W.; Zhang, G. Q.; Li, X. G. Dual-Activity Controlled Asymmetric Synthesis of Superconducting Lead Hemispheres. *Adv. Funct. Mater.* **2007**, *17*, 2198−2202.
(299) Lin, X.-M.; Claus, H.; Welp, U.; Beloborodov, I. S.; Kwok, W.-K.; Crabtree, G. W.; Jaeger, H. M. Growth and Properties of Superconducting Anisotropic Lead Nanoprisms. *J. Phys. Chem. C* **2007**, *111*, 3548−3550.
(300) Liu, Y.; Ai, K.; Liu, J.; Yuan, Q.; He, Y.; Lu, L. A High-Performance Ytterbium-Based Nanoparticulate Contrast Agent for In Vivo X-Ray Computed Tomography Imaging. *Angew. Chem., Int. Ed.* **2012**, *51*, 1437−1442.
(301) Lee, N.; Choi, S. H.; Hyeon, T. Nano-Sized CT Contrast Agents. *Adv. Mater.* **2013**, *25*, 2641−2660.
(302) Chen, G.; Agren, H.; Ohulchanskyy, T. Y.; Prasad, P. N. Light Upconverting Core−Shell Nanostructures: Nanophotonic Control for Emerging Applications. *Chem. Soc. Rev.* **2015**, *44*, 1680−1713.
(303) Smith, B. R.; Gambhir, S. S. Nanomaterials for In Vivo Imaging. *Chem. Rev.* **2017**, *117*, 901−986.
(304) Ibrahim, A. A.; Ahmad, R.; Umar, A.; Al-Assiri, M. S.; Al-Salami, A. E.; Kumar, R.; Ansari, S. G.; Baskoutas, S. Two-Dimensional Ytterbium Oxide Nanodisks Based Biosensor for Selective Detection of Urea. *Biosens. Bioelectron.* **2017**, *98*, 254−260.
(305) Hammond, C. *The Basics of Crystallography and Diffraction*; Oxford University Press, 2015.
(306) Partridge, P. G. The Crystallography and Deformation Modes of Hexagonal Close-Packed Metals. *Metall. Rev.* **1967**, *12*, 169−194.
(307) Asselin, J.; Boukouvala, C.; Hopper, E. R.; Ramasse, Q. M.; Biggins, J. S.; Ringe, E. Tents, Chairs, Tacos, Kites, and Rods: Shapes and Plasmonic Properties of Singly Twinned Magnesium Nanoparticles. *ACS Nano* **2020**, *14*, 5968−5980.
(308) Paik, T.; Gordon, T. R.; Prantner, A. M.; Yun, H.; Murray, C. B. Designing Tripodal and Triangular Gadolinium Oxide Nanoplates and Self-Assembled Nanofibrils as Potential Multimodal Bioimaging Probes. *ACS Nano* **2013**, *7*, 2850−2859.
(309) Cao, Y. C. Synthesis of Square Gadolinium-Oxide Nanoplates. *J. Am. Chem. Soc.* **2004**, *126*, 7456−7457.
(310) Michelakaki, I.; Boukos, N.; Dragatogiannis, D. A.; Stathopoulos, S.; Charitidis, C. A.; Tsoukalas, D. Synthesis of Hafnium Nanoparticles and Hafnium Nanoparticle Films by Gas Condensation and Energetic Deposition. *Beilstein J. Nanotechnol.* **2018**, *9*, 1868−1880.
(311) Krajczewski, J.; Ambroziak, R.; Kudelski, A. Formation and Selected Catalytic Properties of Ruthenium, Rhodium, Osmium and Iridium Nanoparticles. *RSC Adv.* **2022**, *12*, 2123−2144.
(312) Xu, J.; Chen, X.; Xu, Y.; Du, Y.; Yan, C. Ultrathin 2D Rare-Earth Nanomaterials: Compositions, Syntheses, and Applications. *Adv. Mater.* **2020**, *32*, 1806461.
(313) Zhu, X.; Zhang, J.; Liu, J.; Zhang, Y. Recent Progress of Rare-Earth Doped Upconversion Nanoparticles: Synthesis, Optimization, and Applications. *Adv. Sci.* **2019**, *6*, 1901358.
(314) Si, R.; Zhang, Y.-W.; You, L.-P.; Yan, C.-H. Rare-Earth Oxide Nanopolyhedra, Nanoplates, and Nanodisks. *Angew. Chem., Int. Ed.* **2005**, *44*, 3256−3260.
(315) Wang, D.; Kang, Y.; Ye, X.; Murray, C. B. Mineralizer-Assisted Shape-Control of Rare Earth Oxide Nanoplates. *Chem. Mater.* **2014**, *26*, 6328−6332.
(316) Ghosh, S.; Lu, H.-C.; Cho, S. H.; Maruvada, T.; Price, M. C.; Milliron, D. J. Colloidal ReO_3 Nanocrystals: Extra Re d-Electron Instigating a Plasmonic Response. *J. Am. Chem. Soc.* **2019**, *141*, 16331−16343.
(317) Ghosh, D.; Pradhan, S.; Chen, W.; Chen, S. Titanium Nanoparticles Stabilized by Ti−C Covalent Bonds. *Chem. Mater.* **2008**, *20*, 1248−1250.
(318) Ranjbar Bahadori, S.; Hart, R.; Hao, Y.-W. Synthesis of Cobalt, Palladium, and Rhenium Nanoparticles. *Tungsten* **2020**, *2*, 261−288.
(319) Liang, Y.; Feng, R.; Yang, S.; Ma, H.; Liang, J.; Chen, J. Rechargeable Mg Batteries with Graphene-like MoS_2 Cathode and Ultrasmall Mg Nanoparticle Anode. *Adv. Mater.* **2011**, *23*, 640−643.
(320) Zhang, X.; Yang, R.; Yang, J.; Zhao, W.; Zheng, J.; Tian, W.; Li, X. Synthesis of Magnesium Nanoparticles with Superior Hydrogen Storage Properties by Acetylene Plasma Metal Reaction. *Int. J. Hydrog. Energy* **2011**, *36*, 4967−4975.
(321) Aurbach, D.; Lu, Z.; Schechter, A.; Gofer, Y.; Gizbar, H.; Turgeman, R.; Cohen, Y.; Moshkovich, M.; Levi, E. Prototype Systems for Rechargeable Magnesium Batteries. *Nature* **2000**, *407*, 724−727.
(322) Pasquini, L.; Callini, E.; Piscopiello, E.; Montone, A.; Antisari, M. V.; Bonetti, E. Metal-Hydride Transformation Kinetics in Mg Nanoparticles. *Appl. Phys. Lett.* **2009**, *94*, 041918.
(323) Jeon, K.-J.; Moon, H. R.; Ruminski, A. M.; Jiang, B.; Kisielowski, C.; Bardhan, R.; Urban, J. J. Air-Stable Magnesium Nanocomposites Provide Rapid and High-Capacity Hydrogen Storage without Using Heavy-Metal Catalysts. *Nat. Mater.* **2011**, *10*, 286−290.
(324) Liu, W.; Aguey-Zinsou, K.-F. Size Effects and Hydrogen Storage Properties of Mg Nanoparticles Synthesised by an Electroless Reduction Method. *J. Mater. Chem. A* **2014**, *2*, 9718−9726.
(325) Vijayakumar Sheela, H.; Madhusudhanan, V.; Krishnan, G. Substrate-Independent and Catalyst-Free Synthesis of Magnesium Nanowires. *Nanoscale Adv.* **2019**, *1*, 1754−1762.
(326) Li, W.; Li, C.; Zhou, C.; Ma, H.; Chen, J. Metallic Magnesium Nano/Mesoscale Structures: Their Shape-Controlled Preparation and Mg/Air Battery Applications. *Angew. Chem., Int. Ed.* **2006**, *45*, 6009−6012.
(327) Ohno, T.; Yamauchi, K. Magnesium Twinned Particles Grown in Inert Gases. *Jpn. J. Appl. Phys.* **1981**, *20*, 1385−1391.
(328) Sterl, F.; Strohfeldt, N.; Walter, R.; Griessen, R.; Tittl, A.; Giessen, H. Magnesium as Novel Material for Active Plasmonics in the Visible Wavelength Range. *Nano Lett.* **2015**, *15*, 7949−7955.
(329) Duan, X.; Liu, N. Magnesium for Dynamic Nanoplasmonics. *Acc. Chem. Res.* **2019**, *52*, 1979−1989.
(330) Viyannalage, L.; Lee, V.; Dennis, R. V.; Kapoor, D.; Haines, C. D.; Banerjee, S. From Grignard's Reagents to Well-Defined Mg Nanostructures: Distinctive Electrochemical and Solution Reduction Routes. *Chem. Commun.* **2012**, *48*, 5169−5171.
(331) Biggins, J. S.; Yazdi, S.; Ringe, E. Magnesium Nanoparticle Plasmonics. *Nano Lett.* **2018**, *18*, 3752−3758.
(332) Jeong, H.-H.; Mark, A. G.; Fischer, P. Magnesium Plasmonics for UV Applications and Chiral Sensing. *Chem. Commun.* **2016**, *52*, 12179−12182.
(333) Hopper, E. R.; Wayman, T. M. R.; Asselin, J.; Pinho, B.; Boukouvala, C.; Torrente-Murciano, L.; Ringe, E. Size Control in the Colloidal Synthesis of Plasmonic Magnesium Nanoparticles. *J. Phys. Chem. C* **2022**, *126*, 563−577.
(334) Gutierrez, Y.; Ortiz, D.; Sanz, J. M.; Saiz, J. M.; Gonzalez, F.; Everitt, H. O.; Moreno, F. How an Oxide Shell Affects the Ultraviolet Plasmonic Behavior of Ga, Mg, and Al Nanostructures. *Opt. Express* **2016**, *24*, 20621−20631.
(335) Asselin, J.; Hopper, E. R.; Ringe, E. Improving the Stability of Plasmonic Magnesium Nanoparticles in Aqueous Media. *Nanoscale* **2021**, *13*, 20649−20656.
(336) Puntes, V. F.; Gorostiza, P.; Aruguete, D. M.; Bastus, N. G.; Alivisatos, A. P. Collective Behaviour in Two-Dimensional Cobalt Nanoparticle Assemblies Observed by Magnetic Force Microscopy. *Nat. Mater.* **2004**, *3*, 263−268.
(337) Sun, S.; Murray, C. B. Synthesis of Monodisperse Cobalt Nanocrystals and Their Assembly into Magnetic Superlattices (Invited). *J. Appl. Phys.* **1999**, *85*, 4325−4330.

https://doi.org/10.1021/acs.chemrev.3c00033
Chem. Rev. 2023, 123, 3493−3542

(338) Puntes, V. F.; Krishnan, K. M.; Alivisatos, A. P. Colloidal Nanocrystal Shape and Size Control: The Case of Cobalt. *Science* **2001**, *291*, 2115−2117.
(339) Puntes, V. F.; Zanchet, D.; Erdonmez, C. K.; Alivisatos, A. P. Synthesis of Hcp-Co Nanodisks. *J. Am. Chem. Soc.* **2002**, *124*, 12874−12880.
(340) Dumestre, F.; Chaudret, B.; Amiens, C.; Respaud, M.; Fejes, P.; Renaud, P.; Zurcher, P. Unprecedented Crystalline Super-Lattices of Monodisperse Cobalt Nanorods. *Angew. Chem., Int. Ed.* **2003**, *42*, 5213−5216.
(341) Zhang, L.; Wang, H.; Li, J. Solution Reduction Synthesis and Characterizations of HCP Co Nanoplatelets. *Mater. Chem. Phys.* **2009**, *116*, 514−518.
(342) Wang, H.; Zhang, L.; Huang, J.; Li, J. Facile Synthesis and Characterization of Co Nanoplatelets with Tunable Dimensions via Solution Reduction Process. *J. Nanoparticle Res.* **2011**, *13*, 1709−1715.
(343) Li, H.; Liao, S. A Magnetic-Field-Assisted Solution-Phase Route to Cobalt Thin Film Composed of Cobalt Nanosheets. *J. Mater. Chem.* **2009**, *19*, 5207−5211.
(344) Piccinno, F.; Gottschalk, F.; Seeger, S.; Nowack, B. Industrial Production Quantities and Uses of Ten Engineered Nanomaterials in Europe and the World. *J. Nanoparticle Res.* **2012**, *14*, 1109.
(345) Schneider, S. L.; Lim, H. W. A Review of Inorganic UV Filters Zinc Oxide and Titanium Dioxide. *Photodermatol. Photoimmunol. Photomed.* **2019**, *35*, 442−446.
(346) Ghanta, S. R.; Rao, M. H.; Muralidharan, K. Single-Pot Synthesis of Zinc Nanoparticles, Borane (BH_3) and *Closo*-Dodecaborate $(B_{12}H_{12})^{2-}$ Using $LiBH_4$ under Mild Conditions. *Dalton Trans* **2013**, *42*, 8420−8425.
(347) Schutte, K.; Meyer, H.; Gemel, C.; Barthel, J.; Fischer, R. A.; Janiak, C. Synthesis of Cu, Zn and Cu/Zn Brass Alloy Nanoparticles from Metal Amidinate Precursors in Ionic Liquids or Propylene Carbonate with Relevance to Methanol Synthesis. *Nanoscale* **2014**, *6*, 3116−3126.
(348) He, M.; Protesescu, L.; Caputo, R.; Krumeich, F.; Kovalenko, M. V. A General Synthesis Strategy for Monodisperse Metallic and Metalloid Nanoparticles (In, Ga, Bi, Sb, Zn, Cu, Sn, and Their Alloys) via in Situ Formed Metal Long-Chain Amides. *Chem. Mater.* **2015**, *27*, 635−647.
(349) Axet, M. R.; Philippot, K. Catalysis with Colloidal Ruthenium Nanoparticles. *Chem. Rev.* **2020**, *120*, 1085−1145.
(350) Bell, T. E.; Torrente-Murciano, L. H_2 Production via Ammonia Decomposition Using Non-Noble Metal Catalysts: A Review. *Top. Catal.* **2016**, *59*, 1438−1457.
(351) Zhao, M.; Xia, Y. Crystal-Phase and Surface-Structure Engineering of Ruthenium Nanocrystals. *Nat. Rev. Mater.* **2020**, *5*, 440−459.
(352) Xu, J.; Kong, X. Amorphous/Crystalline Heterophase Ruthenium Nanosheets for PH-Universal Hydrogen Evolution. *Small Methods* **2022**, *6*, 2101432.
(353) Li, J.; Hou, M.; Zhang, Z. Insight into the Effects of the Crystal Phase of Ru over Ultrathin Ru@Pt Core−Shell Nanosheets for Methanol Electrooxidation. *Nanoscale* **2022**, *14*, 8096−8102.
(354) Yin, A.-X.; Liu, W.-C.; Ke, J.; Zhu, W.; Gu, J.; Zhang, Y.-W.; Yan, C.-H. Ru Nanocrystals with Shape-Dependent Surface-Enhanced Raman Spectra and Catalytic Properties: Controlled Synthesis and DFT Calculations. *J. Am. Chem. Soc.* **2012**, *134*, 20479−20489.
(355) Watt, J.; Yu, C.; Chang, S. L. Y.; Cheong, S.; Tilley, R. D. Shape Control from Thermodynamic Growth Conditions: The Case of Hcp Ruthenium Hourglass Nanocrystals. *J. Am. Chem. Soc.* **2013**, *135*, 606−609.
(356) Viau, G.; Brayner, R.; Poul, L.; Chakroune, N.; Lacaze, E.; Fiévet-Vincent, F.; Fiévet, F. Ruthenium Nanoparticles: Size, Shape, and Self-Assemblies. *Chem. Mater.* **2003**, *15*, 486−494.
(357) Chen, G.; Zhang, J.; Gupta, A.; Rosei, F.; Ma, D. Shape-Controlled Synthesis of Ruthenium Nanocrystals and Their Catalytic Applications. *New J. Chem.* **2014**, *38*, 1827−1833.
(358) Kong, X.; Xu, K.; Zhang, C.; Dai, J.; Norooz Oliaee, S.; Li, L.; Zeng, X.; Wu, C.; Peng, Z. Free-Standing Two-Dimensional Ru Nanosheets with High Activity toward Water Splitting. *ACS Catal.* **2016**, *6*, 1487−1492.
(359) Ramamoorthy, R. K.; Soulantica, K.; Del Rosal, I.; Arenal, R.; Decorse, P.; Piquemal, J.-Y.; Chaudret, B.; Poteau, R.; Viau, G. Ruthenium Icosahedra and Ultrathin Platelets: The Role of Surface Chemistry on the Nanoparticle Structure. *Chem. Mater.* **2022**, *34*, 2931−2944.
(360) Wang, J.; Wang, S.-Q. Surface Energy and Work Function of Fcc and Bcc Crystals: Density Functional Study. *Surf. Sci.* **2014**, *630*, 216−224.
(361) Kelly, A.; Knowles, K. M. *Crystallography and Crystal Defects*; John Wiley & Sons, 2020.
(362) Hopper, E. R.; Boukouvala, C.; Johnstone, D. N.; Biggins, J. S.; Ringe, E. On the Identification of Twinning in Body-Centred Cubic Nanoparticles. *Nanoscale* **2020**, *12*, 22009−22013.
(363) Wang, C.; Xu, L.; Li, X.; Lin, Q. Divalent Europium Nanocrystals: Controllable Synthesis, Properties, and Applications. *ChemPhysChem* **2012**, *13*, 3765−3772.
(364) Meffre, A.; Lachaize, S.; Gatel, C.; Respaud, M.; Chaudret, B. Use of Long Chain Amine as a Reducing Agent for the Synthesis of High Quality Monodisperse Iron(0) Nanoparticles. *J. Mater. Chem.* **2011**, *21*, 13464−13469.
(365) Son, S. U.; Jang, Y.; Yoon, K. Y.; An, C.; Hwang, Y.; Park, J.-G.; Noh, H.-J.; Kim, J.-Y.; Park, J.-H.; Hyeon, T. Synthesis of Monodisperse Chromium Nanoparticles from the Thermolysis of a Fischer Carbene Complex. *Chem. Commun.* **2005**, *2005*, 86−88.
(366) Malyshev, D.; Bosca, F.; Crites, C.-O. L.; Hallett-Tapley, G. L.; Netto-Ferreira, J. C.; Alarcon, E. I.; Scaiano, J. C. Size-Controlled Photochemical Synthesis of Niobium Nanoparticles. *Dalton Trans* **2013**, *42*, 14049−14052.
(367) Khani, A. H.; Rashidi, A. M.; Kashi, G. Synthesis of Tungsten Nanoparticles by Reverse Micelle Method. *J. Mol. Liq.* **2017**, *241*, 897−903.
(368) Che, J. G.; Chan, C. T.; Jian, W.-E.; Leung, T. C. Surface Atomic Structures, Surface Energies, and Equilibrium Crystal Shape of Molybdenum. *Phys. Rev. B* **1998**, *57*, 1875−1880.
(369) Sun, M.; Stolte, N.; Wang, J.; Wei, J.; Chen, P.; Xu, Z.; Wang, W.; Pan, D.; Bai, X. The Lightest 2D Nanomaterial: Freestanding Ultrathin Li Nanosheets by In Situ Nanoscale Electrochemistry. *Small* **2021**, *17*, 2101641.
(370) Amorós, J.; Ravi, S. Correlation among Several Physicochemical Properties of Alkali Metals in the Light of the Corresponding States Principle. *Phys. Chem. Liq.* **2011**, *49*, 9−20.
(371) Guan, J.; Yan, G.; Wang, W.; Liu, J. External Field-Assisted Solution Synthesis and Selectively Catalytic Properties of Amorphous Iron Nanoplatelets. *J. Mater. Chem.* **2012**, *22*, 3909−3915.
(372) Bondi, J. F.; Oyler, K. D.; Ke, X.; Schiffer, P.; Schaak, R. E. Chemical Synthesis of Air-Stable Manganese Nanoparticles. *J. Am. Chem. Soc.* **2009**, *131*, 9144−9145.
(373) Zhao, X.; Di, Q.; Wu, X.; Liu, Y.; Yu, Y.; Wei, G.; Zhang, J.; Quan, Z. Mild Synthesis of Monodisperse Tin Nanocrystals and Tin Chalcogenide Hollow Nanostructures. *Chem. Commun.* **2017**, *53*, 11001−11004.
(374) Kravchyk, K.; Protesescu, L.; Bodnarchuk, M. I.; Krumeich, F.; Yarema, M.; Walter, M.; Guntlin, C.; Kovalenko, M. V. Monodisperse and Inorganically Capped Sn and Sn/SnO_2 Nanocrystals for High-Performance Li-Ion Battery Anodes. *J. Am. Chem. Soc.* **2013**, *135*, 4199−4202.
(375) Castilla-Amorós, L.; Chien, T.-C. C.; Pankhurst, J. R.; Buonsanti, R. Modulating the Reactivity of Liquid Ga Nanoparticle Inks by Modifying Their Surface Chemistry. *J. Am. Chem. Soc.* **2022**, *144*, 1993−2001.
(376) Yarema, M.; Wörle, M.; Rossell, M. D.; Erni, R.; Caputo, R.; Protesescu, L.; Kravchyk, K. V.; Dirin, D. N.; Lienau, K.; von Rohr, F.; et al. Monodisperse Colloidal Gallium Nanoparticles: Synthesis, Low Temperature Crystallization, Surface Plasmon Resonance and Li-Ion Storage. *J. Am. Chem. Soc.* **2014**, *136*, 12422−12430.
(377) Chockla, A. M.; Harris, J. T.; Korgel, B. A. Colloidal Synthesis of Germanium Nanorods. *Chem. Mater.* **2011**, *23*, 1964−1970.

(378) Vaughn, D. D. I.; Bondi, J. F.; Schaak, R. E. Colloidal Synthesis of Air-Stable Crystalline Germanium Nanoparticles with Tunable Sizes and Shapes. *Chem. Mater.* **2010**, *22*, 6103−6108.
(379) Chou, N. H.; Oyler, K. D.; Motl, N. E.; Schaak, R. E. Colloidal Synthesis of Germanium Nanocrystals Using Room-Temperature Benchtop Chemistry. *Chem. Mater.* **2009**, *21*, 4105−4107.
(380) Chou, N. H.; Ke, X.; Schiffer, P.; Schaak, R. E. Room-Temperature Chemical Synthesis of Shape-Controlled Indium Nanoparticles. *J. Am. Chem. Soc.* **2008**, *130*, 8140−8141.
(381) Boldt, R.; Kaiser, M.; Köhler, D.; Krumeich, F.; Ruck, M. High-Yield Synthesis and Structure of Double-Walled Bismuth-Nanotubes. *Nano Lett.* **2010**, *10*, 208−210.
(382) Khanna, P. K.; Jun, K.-W.; Hong, K. B.; Baeg, J.-O.; Chikate, R. C.; Das, B. K. Colloidal Synthesis of Indium Nanoparticles by Sodium Reduction Method. *Mater. Lett.* **2005**, *59*, 1032−1036.
(383) Wu, F.-Y.; Yang, C. C.; Wu, C.-M.; Wang, C.-W.; Li, W.-H. Superconductivity in Zero-Dimensional Indium Nanoparticles. *J. Appl. Phys.* **2007**, *101*, 09G111.
(384) Lim, T. H.; Ingham, B.; Kamarudin, K. H.; Etchegoin, P. G.; Tilley, R. D. Solution Synthesis of Monodisperse Indium Nanoparticles and Highly Faceted Indium Polyhedra. *Cryst. Growth Des.* **2010**, *10*, 3854−3858.
(385) Das, R.; Soni, R. K. Synthesis and Surface-Enhanced Raman Scattering of Indium Nanotriangles and Nanowires. *RSC Adv.* **2017**, *7*, 32255−32263.
(386) Wang, J.; Yang, Q.; Zhang, Z. Growth of One-Dimensional Hierarchical Multilayered Indium Nanostructures. *Cryst. Growth Des.* **2009**, *9*, 3036−3043.
(387) Ning, W.; Kong, F.; Han, Y.; Du, H.; Yang, J.; Tian, M.; Zhang, Y. Robust Surface State Transport in Thin Bismuth Nanoribbons. *Sci. Rep.* **2014**, *4*, 7086.
(388) Qi, X.-L.; Zhang, S.-C. Topological Insulators and Superconductors. *Rev. Mod. Phys.* **2011**, *83*, 1057−1110.
(389) Li, L.; Checkelsky, J. G.; Hor, Y. S.; Uher, C.; Hebard, A. F.; Cava, R. J.; Ong, N. P. Phase Transitions of Dirac Electrons in Bismuth. *Science* **2008**, *321*, 547−550.
(390) Behnia, K.; Balicas, L.; Kopelevich, Y. Signatures of Electron Fractionalization in Ultraquantum Bismuth. *Science* **2007**, *317*, 1729−1731.
(391) Dong, A.; Tang, R.; Buhro, W. E. Solution-Based Growth and Structural Characterization of Homo- and Heterobranched Semiconductor Nanowires. *J. Am. Chem. Soc.* **2007**, *129*, 12254−12262.
(392) Wang, F.; Dong, A.; Sun, J.; Tang, R.; Yu, H.; Buhro, W. E. Solution−Liquid−Solid Growth of Semiconductor Nanowires. *Inorg. Chem.* **2006**, *45*, 7511−7521.
(393) Gutiérrez, M.; Henglein, A. Nanometer-Sized Bi Particles in Aqueous Solution: Absorption Spectrum and Some Chemical Properties. *J. Phys. Chem.* **1996**, *100*, 7656−7661.
(394) Fang, J.; Stokes, K. L.; Zhou, W. L.; Wang, W.; Lin, J. Self-Assembled Bismuth Nanocrystallites. *Chem. Commun.* **2001**, 1872−1873.
(395) Wang, J.; Wang, X.; Peng, Q.; Li, Y. Synthesis and Characterization of Bismuth Single-Crystalline Nanowires and Nanospheres. *Inorg. Chem.* **2004**, *43*, 7552−7556.
(396) Wang, Y. W.; Hong, B. H.; Kim, K. S. Size Control of Semimetal Bismuth Nanoparticles and the UV−Visible and IR Absorption Spectra. *J. Phys. Chem. B* **2005**, *109*, 7067−7072.
(397) Wang, W. Z.; Poudel, B.; Ma, Y.; Ren, Z. F. Shape Control of Single Crystalline Bismuth Nanostructures. *J. Phys. Chem. B* **2006**, *110*, 25702−25706.
(398) Wang, F.; Tang, R.; Yu, H.; Gibbons, P. C.; Buhro, W. E. Size- and Shape-Controlled Synthesis of Bismuth Nanoparticles. *Chem. Mater.* **2008**, *20*, 3656−3662.
(399) Wang, Y.; Chen, J.; Chen, L.; Chen, Y.-B.; Wu, L.-M. Shape-Controlled Solventless Syntheses of Nano Bi Disks and Spheres. *Cryst. Growth Des.* **2010**, *10*, 1578−1584.
(400) Manna, G.; Bose, R.; Pradhan, N. Photocatalytic Au−Bi2S3 Heteronanostructures. *Angew. Chem., Int. Ed.* **2014**, *53*, 6743−6746.
(401) Sun, H.; Li, H.; Harvey, I.; Sadler, P. J. Interactions of Bismuth Complexes with Metallothionein(II). *J. Biol. Chem.* **1999**, *274*, 29094−29101.
(402) Song, Y.; Li, W.; Jing, H.; Liang, X.; Zhou, Y.; Li, N.; Feng, S. Spatiotemporal Sonodynamic Therapy for the Treatment of Rheumatoid Arthritis Based on Z-Scheme Heterostructure Sonosensitizer of HO-1 Inhibitor Jointed Bismuth Nanotriangle. *Chem. Eng. J.* **2022**, *438*, 135558.
(403) Fu, R.; Xu, S.; Lu, Y.-N.; Zhu, J.-J. Synthesis and Characterization of Triangular Bismuth Nanoplates. *Cryst. Growth Des.* **2005**, *5*, 1379−1385.
(404) Sun, Z.; Umar, A.; Zeng, J.; Luo, X.; Song, L.; Zhang, Z.; Chen, Z.; Li, J.; Su, F.; Huang, Y. Highly Pure Gold Nanotriangles with Almost 100% Yield for Surface-Enhanced Raman Scattering. *ACS Appl. Nano Mater.* **2022**, *5*, 1220−1231.
(405) Zhang, X.-Y.; Hu, A.; Zhang, T.; Lei, W.; Xue, X.-J.; Zhou, Y.; Duley, W. W. Self-Assembly of Large-Scale and Ultrathin Silver Nanoplate Films with Tunable Plasmon Resonance Properties. *ACS Nano* **2011**, *5*, 9082−9092.
(406) Kim, J.; Song, X.; Ji, F.; Luo, B.; Ice, N. F.; Liu, Q.; Zhang, Q.; Chen, Q. Polymorphic Assembly from Beveled Gold Triangular Nanoprisms. *Nano Lett.* **2017**, *17*, 3270−3275.
(407) Fu, Q.; Ran, G.; Xu, W. Direct Self-Assembly of CTAB-Capped Au Nanotriangles. *Nano Res.* **2016**, *9*, 3247−3256.
(408) Vutukuri, H. R.; Badaire, S.; de Winter, D. A. M.; Imhof, A.; van Blaaderen, A. Directed Self-Assembly of Micron-Sized Gold Nanoplatelets into Oriented Flexible Stacks with Tunable Interplate Distance. *Nano Lett.* **2015**, *15*, 5617−5623.
(409) Zhan, P.; Wen, T.; Wang, Z.; He, Y.; Shi, J.; Wang, T.; Liu, X.; Lu, G.; Ding, B. DNA Origami Directed Assembly of Gold Bowtie Nanoantennas for Single-Molecule Surface-Enhanced Raman Scattering. *Angew. Chem., Int. Ed.* **2018**, *57*, 2846−2850.
(410) Kim, J.-Y.; Lee, J.-S. Synthesis and Thermodynamically Controlled Anisotropic Assembly of DNA−Silver Nanoprism Conjugates for Diagnostic Applications. *Chem. Mater.* **2010**, *22*, 6684−6691.
(411) Zhou, Y.; Zhou, X.; Park, D. J.; Torabi, K.; Brown, K. A.; Jones, M. R.; Zhang, C.; Schatz, G. C.; Mirkin, C. A. Shape-Selective Deposition and Assembly of Anisotropic Nanoparticles. *Nano Lett.* **2014**, *14*, 2157−2161.
(412) Neal, R. D.; Hughes, R. A.; Preston, A. S.; Golze, S. D.; Demille, T. B.; Neretina, S. Substrate-Immobilized Noble Metal Nanoplates: A Review of Their Synthesis, Assembly, and Application. *J. Mater. Chem. C* **2021**, *9*, 12974−13012.
(413) Neal, R. D.; Lawson, Z. R.; Tuff, W. J.; Xu, K.; Kumar, V.; Korsa, M. T.; Zhukovskyi, M.; Rosenberger, M. R.; Adam, J.; Hachtel, J. A.; et al. Large-Area Periodic Arrays of Atomically Flat Single-Crystal Gold Nanotriangles Formed Directly on Substrate Surfaces. *Small* **2022**, *18*, 2205780.
(414) Shevchenko, E. V.; Talapin, D. V.; Kotov, N. A.; O'Brien, S.; Murray, C. B. Structural Diversity in Binary Nanoparticle Superlattices. *Nature* **2006**, *439*, 55−59.
(415) Jones, M. R.; Macfarlane, R. J.; Prigodich, A. E.; Patel, P. C.; Mirkin, C. A. Nanoparticle Shape Anisotropy Dictates the Collective Behavior of Surface-Bound Ligands. *J. Am. Chem. Soc.* **2011**, *133*, 18865−18869.
(416) Park, K.; Koerner, H.; Vaia, R. A. Depletion-Induced Shape and Size Selection of Gold Nanoparticles. *Nano Lett.* **2010**, *10*, 1433−1439.
(417) Young, K. L.; Jones, M. R.; Zhang, J.; Macfarlane, R. J.; Esquivel-Sirvent, R.; Nap, R. J.; Wu, J.; Schatz, G. C.; Lee, B.; Mirkin, C. A. Assembly of Reconfigurable One-Dimensional Colloidal Superlattices Due to a Synergy of Fundamental Nanoscale Forces. *Proc. Natl. Acad. Sci. U. S. A.* **2012**, *109*, 2240−2245.
(418) Zoric, I.; Zach, M.; Kasemo, B.; Langhammer, C. Gold, Platinum, and Aluminum Nanodisk Plasmons: Material Independence, Subradiance, and Damping Mechanisms. *ACS Nano* **2011**, *5*, 2535−2546.

https://doi.org/10.1021/acs.chemrev.3c00033
Chem. Rev. 2023, 123, 3493−3542

(419) Fan, Z.; Huang, X.; Tan, C.; Zhang, H. Thin Metal Nanostructures: Synthesis, Properties and Applications. *Chem. Sci.* **2015**, *6*, 95−111.
(420) Kinkhabwala, A.; Yu, Z.; Fan, S.; Avlasevich, Y.; Müllen, K.; Moerner, W. E. Large Single-Molecule Fluorescence Enhancements Produced by a Bowtie Nanoantenna. *Nat. Photonics* **2009**, *3*, 654−657.
(421) Aćimović, S. S.; Kreuzer, M. P.; González, M. U.; Quidant, R. Plasmon Near-Field Coupling in Metal Dimers as a Step toward Single-Molecule Sensing. *ACS Nano* **2009**, *3*, 1231−1237.
(422) Gao, C.; Lu, Z.; Liu, Y.; Zhang, Q.; Chi, M.; Cheng, Q.; Yin, Y. Highly Stable Silver Nanoplates for Surface Plasmon Resonance Biosensing. *Angew. Chem., Int. Ed.* **2012**, *51*, 5629−5633.
(423) Suh, J. Y.; Kim, C. H.; Zhou, W.; Huntington, M. D.; Co, D. T.; Wasielewski, M. R.; Odom, T. W. Plasmonic Bowtie Nanolaser Arrays. *Nano Lett.* **2012**, *12*, 5769−5774.
(424) Liu, D.; Yang, D.; Gao, Y.; Ma, J.; Long, R.; Wang, C.; Xiong, Y. Flexible Near-Infrared Photovoltaic Devices Based on Plasmonic Hot-Electron Injection into Silicon Nanowire Arrays. *Angew. Chem., Int. Ed.* **2016**, *55*, 4577−4581.
(425) Wang, B.; Zou, Y.; Lu, H.; Kong, W.; Singh, S. C.; Zhao, C.; Yao, C.; Xing, J.; Zheng, X.; Yu, Z.; et al. Boosting Perovskite Photodetector Performance in NIR Using Plasmonic Bowtie Nanoantenna Arrays. *Small* **2020**, *16*, 2001417.
(426) Yu, K.; Devkota, T.; Beane, G.; Wang, G. P.; Hartland, G. V. Brillouin Oscillations from Single Au Nanoplate Opto-Acoustic Transducers. *ACS Nano* **2017**, *11*, 8064−8071.
(427) Yu, K.; Yang, Y.; Wang, J.; Hartland, G. V.; Wang, G. P. Nanoparticle−Fluid Interactions at Ultrahigh Acoustic Vibration Frequencies Studied by Femtosecond Time-Resolved Microscopy. *ACS Nano* **2021**, *15*, 1833−1840.
(428) Munkhbat, B.; Canales, A.; Küçüköz, B.; Baranov, D. G.; Shegai, T. O. Tunable Self-Assembled Casimir Microcavities and Polaritons. *Nature* **2021**, *597*, 214−219.
(429) Wang, J.; Yu, K.; Yang, Y.; Hartland, G. V.; Sader, J. E.; Wang, G. P. Strong Vibrational Coupling in Room Temperature Plasmonic Resonators. *Nat. Commun.* **2019**, *10*, 1527.
(430) Bu, L.; Zhang, N.; Guo, S.; Zhang, X.; Li, J.; Yao, J.; Wu, T.; Lu, G.; Ma, J.-Y.; Su, D.; et al. Biaxially Strained PtPb/Pt Core/Shell Nanoplate Boosts Oxygen Reduction Catalysis. *Science* **2016**, *354*, 1410−1414.
(431) Luo, S.; Zhang, L.; Liao, Y.; Li, L.; Yang, Q.; Wu, X.; Wu, X.; He, D.; He, C.; Chen, W.; et al. A Tensile-Strained Pt−Rh Single-Atom Alloy Remarkably Boosts Ethanol Oxidation. *Adv. Mater.* **2021**, *33*, 2008508.
(432) Liu, M.; Liu, Z.; Xie, M.; Zhang, Z.; Zhang, S.; Cheng, T.; Gao, C. Ligand-Mediated Self-Terminating Growth of Single-Atom Pt on Au Nanocrystals for Improved Formic Acid Oxidation Activity. *Adv. Energy Mater.* **2022**, *12*, 2103195.
(433) Chan, G. H.; Zhao, J.; Hicks, E. M.; Schatz, G. C.; Van Duyne, R. P. Plasmonic Properties of Copper Nanoparticles Fabricated by Nanosphere Lithography. *Nano Lett.* **2007**, *7*, 1947−1952.
(434) Xiong, Y.; McLellan, J. M.; Chen, J.; Yin, Y.; Li, Z.-Y.; Xia, Y. Kinetically Controlled Synthesis of Triangular and Hexagonal Nanoplates of Palladium and Their SPR/SERS Properties. *J. Am. Chem. Soc.* **2005**, *127*, 17118−17127.
(435) Langhammer, C.; Schwind, M.; Kasemo, B.; Zoric, I. Localized Surface Plasmon Resonances in Aluminum Nanodisks. *Nano Lett.* **2008**, *8*, 1461−1471.
(436) Brioude, A.; Pileni, M. P. Silver Nanodisks: Optical Properties Study Using the Discrete Dipole Approximation Method. *J. Phys. Chem. B* **2005**, *109*, 23371−23377.
(437) Kelly, K. L.; Coronado, E.; Zhao, L. L.; Schatz, G. C. The Optical Properties of Metal Nanoparticles: The Influence of Size, Shape, and Dielectric Environment. *J. Phys. Chem. B* **2003**, *107*, 668−677.
(438) Ye, J.; Chen, C.; Roy, W. V.; Van Dorpe, P.; Maes, G.; Borghs, G. The Fabrication and Optical Property of Silver Nanoplates with Different Thicknesses. *Nanotechnology* **2008**, *19*, 325702.
(439) Cui, X.; Qin, F.; Ruan, Q.; Zhuo, X.; Wang, J. Circular Gold Nanodisks with Synthetically Tunable Diameters and Thicknesses. *Adv. Funct. Mater.* **2018**, *28*, 1705516.
(440) Zhang, Q.; Ge, J.; Pham, T.; Goebl, J.; Hu, Y.; Lu, Z.; Yin, Y. Reconstruction of Silver Nanoplates by UV Irradiation: Tailored Optical Properties and Enhanced Stability. *Angew. Chem., Int. Ed.* **2009**, *48*, 3516−3519.
(441) Smith, K. W.; Yang, J.; Hernandez, T.; Swearer, D. F.; Scarabelli, L.; Zhang, H.; Zhao, H.; Moringo, N. A.; Chang, W.-S.; Liz-Marzán, L. M.; et al. Environmental Symmetry Breaking Promotes Plasmon Mode Splitting in Gold Nanotriangles. *J. Phys. Chem. C* **2018**, *122*, 13259−13266.
(442) Losquin, A.; Zagonel, L. F.; Myroshnychenko, V.; Rodríguez-González, B.; Tencé, M.; Scarabelli, L.; Förstner, J.; Liz-Marzán, L. M.; García de Abajo, F. J.; Stéphan, O.; et al. Unveiling Nanometer Scale Extinction and Scattering Phenomena through Combined Electron Energy Loss Spectroscopy and Cathodoluminescence Measurements. *Nano Lett.* **2015**, *15*, 1229−1237.
(443) O'Brien, M. N.; Jones, M. R.; Kohlstedt, K. L.; Schatz, G. C.; Mirkin, C. A. Uniform Circular Disks With Synthetically Tailorable Diameters: Two-Dimensional Nanoparticles for Plasmonics. *Nano Lett.* **2015**, *15*, 1012−1017.
(444) Wang, M.; Wu, Z.; Krasnok, A.; Zhang, T.; Liu, M.; Liu, H.; Scarabelli, L.; Fang, J.; Liz-Marzán, L. M.; Terrones, M.; et al. Dark-Exciton-Mediated Fano Resonance from a Single Gold Nanostructure on Monolayer WS2 at Room Temperature. *Small* **2019**, *15*, 1900982.
(445) Qin, F.; Cui, X.; Ruan, Q.; Lai, Y.; Wang, J.; Ma, H.; Lin, H.-Q. Role of Shape in Substrate-Induced Plasmonic Shift and Mode Uncovering on Gold Nanocrystals. *Nanoscale* **2016**, *8*, 17645−17657.
(446) Cui, X.; Lai, Y.; Qin, F.; Shao, L.; Wang, J.; Lin, H.-Q. Strengthening Fano Resonance on Gold Nanoplates with Gold Nanospheres. *Nanoscale* **2020**, *12*, 1975−1984.
(447) Cui, X.; Lai, Y.; Ai, R.; Wang, H.; Shao, L.; Chen, H.; Zhang, W.; Wang, J. Anapole States and Toroidal Resonances Realized in Simple Gold Nanoplate-on-Mirror Structures. *Adv. Optical Mater.* **2020**, *8*, 2001173.
(448) Rajeeva, B. B.; Hernandez, D. S.; Wang, M.; Perillo, E.; Lin, L.; Scarabelli, L.; Pingali, B.; Liz-Marzán, L. M.; Dunn, A. K.; Shear, J. B.; et al. Regioselective Localization and Tracking of Biomolecules on Single Gold Nanoparticles. *Adv. Sci.* **2015**, *2*, 1500232.
(449) Wang, M.; Bangalore Rajeeva, B.; Scarabelli, L.; Perillo, E. P.; Dunn, A. K.; Liz-Marzán, L. M.; Zheng, Y. Molecular-Fluorescence Enhancement via Blue-Shifted Plasmon-Induced Resonance Energy Transfer. *J. Phys. Chem. C* **2016**, *120*, 14820−14827.
(450) Yin, H.; Guo, Y.; Cui, X.; Lu, W.; Yang, Z.; Yang, B.; Wang, J. Plasmonic and Sensing Properties of Vertically Oriented Hexagonal Gold Nanoplates. *Nanoscale* **2018**, *10*, 15058−15070.
(451) Matsuura, T.; Imaeda, K.; Hasegawa, S.; Suzuki, H.; Imura, K. Characterization of Overlapped Plasmon Modes in a Gold Hexagonal Plate Revealed by Three-Dimensional Near-Field Optical Microscopy. *J. Phys. Chem. Lett.* **2019**, *10*, 819−824.
(452) Imaeda, K.; Hasegawa, S.; Imura, K. Observation of the Plasmon Mode Transition from Triangular to Hexagonal Nanoplates. *J. Chem. Phys.* **2022**, *156*, 044702.
(453) Hasegawa, S.; Imaeda, K.; Imura, K. Plasmon-Enhanced Fluorescence Near Single Gold Nanoplates Studied by Scanning Near-Field Two-Photon Excitation Microscopy. *J. Phys. Chem. C* **2021**, *125*, 21070−21076.
(454) Nelayah, J.; Kociak, M.; Stéphan, O.; García de Abajo, F. J.; Tencé, M.; Henrard, L.; Taverna, D.; Pastoriza-Santos, I.; Liz-Marzán, L. M.; Colliex, C. Mapping Surface Plasmons on a Single Metallic Nanoparticle. *Nat. Phys.* **2007**, *3*, 348−353.
(455) Schmidt, F. P.; Ditlbacher, H.; Hofer, F.; Krenn, J. R.; Hohenester, U. Morphing a Plasmonic Nanodisk into a Nanotriangle. *Nano Lett.* **2014**, *14*, 4810−4815.
(456) Imaeda, K.; Hasegawa, S.; Imura, K. Imaging of Plasmonic Eigen Modes in Gold Triangular Mesoplates by Near-Field Optical Microscopy. *J. Phys. Chem. C* **2018**, *122*, 7399−7409.

https://doi.org/10.1021/acs.chemrev.3c00033
Chem. Rev. 2023, 123, 3493−3542

(457) Losquin, A.; Camelio, S.; Rossouw, D.; Besbes, M.; Pailloux, F.; Babonneau, D.; Botton, G. A.; Greffet, J.-J.; Stéphan, O.; Kociak, M. Experimental Evidence of Nanometer-Scale Confinement of Plasmonic Eigenmodes Responsible for Hot Spots in Random Metallic Films. *Phys. Rev. B* **2013**, *88*, 115427.
(458) Frank, B.; Kahl, P.; Podbiel, D.; Spektor, G.; Orenstein, M.; Fu, L.; Weiss, T.; Horn-von Hoegen, M.; Davis, T. J.; Meyer zu Heringdorf, F.-J.; Giessen, H.; et al. Short-Range Surface Plasmonics: Localized Electron Emission Dynamics from a 60-Nm Spot on an Atomically Flat Single-Crystalline Gold Surface. *Sci. Adv.* **2017**, *3*, No. e1700721.
(459) Podbiel, D.; Kahl, P.; Makris, A.; Frank, B.; Sindermann, S.; Davis, T. J.; Giessen, H.; Hoegen, M. H.; Meyer zu Heringdorf, F.-J. Imaging the Nonlinear Plasmoemission Dynamics of Electrons from Strong Plasmonic Fields. *Nano Lett.* **2017**, *17*, 6569−6574.
(460) Davis, T. J.; Janoschka, D.; Dreher, P.; Frank, B.; Meyer zu Heringdorf, F.-J.; Giessen, H. Ultrafast Vector Imaging of Plasmonic Skyrmion Dynamics with Deep Subwavelength Resolution. *Science* **2020**, *368*, No. eaba6415.
(461) Dabrowski, M.; Dai, Y.; Petek, H. Ultrafast Photoemission Electron Microscopy: Imaging Plasmons in Space and Time. *Chem. Rev.* **2020**, *120*, 6247−6287.
(462) Zengin, G.; Wersäll, M.; Nilsson, S.; Antosiewicz, T. J.; Käll, M.; Shegai, T. Realizing Strong Light-Matter Interactions between Single-Nanoparticle Plasmons and Molecular Excitons at Ambient Conditions. *Phys. Rev. Lett.* **2015**, *114*, 157401.
(463) Geisler, M.; Cui, X.; Wang, J.; Rindzevicius, T.; Gammelgaard, L.; Jessen, B. S.; Gonçalves, P. A. D.; Todisco, F.; Bøggild, P.; Boisen, A.; et al. Single-Crystalline Gold Nanodisks on WS2Mono- and Multilayers for Strong Coupling at Room Temperature. *ACS Photonics* **2019**, *6*, 994−1001.
(464) Wersäll, M.; Munkhbat, B.; Baranov, D. G.; Herrera, F.; Cao, J.; Antosiewicz, T. J.; Shegai, T. Correlative Dark-Field and Photoluminescence Spectroscopy of Individual Plasmon−Molecule Hybrid Nanostructures in a Strong Coupling Regime. *ACS Photonics* **2019**, *6*, 2570−2576.
(465) Wang, M.; Krasnok, A.; Zhang, T.; Scarabelli, L.; Liu, H.; Wu, Z.; Liz-Marzán, L. M.; Terrones, M.; Alù, A.; Zheng, Y. Tunable Fano Resonance and Plasmon−Exciton Coupling in Single Au Nanotriangles on Monolayer WS2 at Room Temperature. *Adv. Mater.* **2018**, *30*, 1705779.
(466) Huang, J.-S.; Callegari, V.; Geisler, P.; Brüning, C.; Kern, J.; Prangsma, J. C.; Wu, X.; Feichtner, T.; Ziegler, J.; Weinmann, P.; et al. Atomically Flat Single-Crystalline Gold Nanostructures for Plasmonic Nanocircuitry. *Nat. Commun.* **2010**, *1*, 150.
(467) Cui, X.; Qin, F.; Lai, Y.; Wang, H.; Shao, L.; Chen, H.; Wang, J.; Lin, H. Molecular Tunnel Junction-Controlled High-Order Charge Transfer Plasmon and Fano Resonances. *ACS Nano* **2018**, *12*, 12541−12550.
(468) Yang, L.; Xie, X.; Yang, J.; Xue, M.; Wu, S.; Xiao, S.; Song, F.; Dang, J.; Sun, S.; Zuo, Z.; et al. Strong Light−Matter Interactions between Gap Plasmons and Two-Dimensional Excitons under Ambient Conditions in a Deterministic Way. *Nano Lett.* **2022**, *22*, 2177−2186.
(469) Deeb, C.; Guo, Z.; Yang, A.; Huang, L.; Odom, T. W. Correlating Nanoscopic Energy Transfer and Far-Field Emission to Unravel Lasing Dynamics in Plasmonic Nanocavity Arrays. *Nano Lett.* **2018**, *18*, 1454−1459.
(470) Lin, P.-T.; Chu, H.-Y.; Lu, T.-W.; Lee, P.-T. Trapping Particles Using Waveguide-Coupled Gold Bowtie Plasmonic Tweezers. *Lab. Chip* **2014**, *14*, 4647−4652.
(471) Fromm, D. P.; Sundaramurthy, A.; Schuck, P. J.; Kino, G.; Moerner, W. E. Gap-Dependent Optical Coupling of Single "Bowtie" Nanoantennas Resonant in the Visible. *Nano Lett.* **2004**, *4*, 957−961.
(472) Roxworthy, B. J.; Ko, K. D.; Kumar, A.; Fung, K. H.; Chow, E. K. C.; Liu, G. L.; Fang, N. X.; Toussaint, K. C., Jr. Application of Plasmonic Bowtie Nanoantenna Arrays for Optical Trapping, Stacking, and Sorting. *Nano Lett.* **2012**, *12*, 796−801.
(473) Kim, S.; Jin, J.; Kim, Y.-J.; Park, I.-Y.; Kim, Y.; Kim, S.-W. High-Harmonic Generation by Resonant Plasmon Field Enhancement. *Nature* **2008**, *453*, 757−760.
(474) Hentschel, M.; Utikal, T.; Giessen, H.; Lippitz, M. Quantitative Modeling of the Third Harmonic Emission Spectrum of Plasmonic Nanoantennas. *Nano Lett.* **2012**, *12*, 3778−3782.
(475) Hatab, N. A.; Hsueh, C.-H.; Gaddis, A. L.; Retterer, S. T.; Li, J.-H.; Eres, G.; Zhang, Z.; Gu, B. Free-Standing Optical Gold Bowtie Nanoantenna with Variable Gap Size for Enhanced Raman Spectroscopy. *Nano Lett.* **2010**, *10*, 4952−4955.
(476) Koenderink, A. F. Single-Photon Nanoantennas. *ACS Photonics* **2017**, *4*, 710−722.
(477) Tserkezis, C.; Esteban, R.; Sigle, D. O.; Mertens, J.; Herrmann, L. O.; Baumberg, J. J.; Aizpurua, J. Hybridization of Plasmonic Antenna and Cavity Modes: Extreme Optics of Nanoparticle-on-Mirror Nanogaps. *Phys. Rev. A* **2015**, *92*, 053811.
(478) Zhu, W.; Esteban, R.; Borisov, A. G.; Baumberg, J. J.; Nordlander, P.; Lezec, H. J.; Aizpurua, J.; Crozier, K. B. Quantum Mechanical Effects in Plasmonic Structures with Subnanometre Gaps. *Nat. Commun.* **2016**, *7*, 11495.
(479) Wang, Q.; Li, C.; Hou, L.; Zhang, H.; Gan, X.; Liu, K.; Premaratne, M.; Xiao, F.; Zhao, J. Unveiling Radial Breathing Mode in a Particle-on-Mirror Plasmonic Nanocavity. *Nanophotonics* **2022**, *11*, 487−494.
(480) Belacel, C.; Habert, B.; Bigourdan, F.; Marquier, F.; Hugonin, J.-P.; Michaelis de Vasconcellos, S.; Lafosse, X.; Coolen, L.; Schwob, C.; Javaux, C.; et al. Controlling Spontaneous Emission with Plasmonic Optical Patch Antennas. *Nano Lett.* **2013**, *13*, 1516−1521.
(481) Qin, J.; Chen, Y.-H.; Zhang, Z.; Zhang, Y.; Blaikie, R. J.; Ding, B.; Qiu, M. Revealing Strong Plasmon-Exciton Coupling between Nanogap Resonators and Two-Dimensional Semiconductors at Ambient Conditions. *Phys. Rev. Lett.* **2020**, *124*, 063902.
(482) Huang, H.; Wang, H.; Li, S.; Jiang, J.; Liu, Y.; Cai, M.; Shao, L.; Chen, H.; Wang, J. WS_2−Flake-Sandwiched, Au-Nanodisk-Enabled High-Quality Fabry−Pérot Nanoresonators for Photoluminescence Modulation. *ACS Nano* **2022**, *16*, 14874−14884.
(483) Chen, H.; Jiang, Z.; Hu, H.; Kang, B.; Zhang, B.; Mi, X.; Guo, L.; Zhang, C.; Li, J.; Lu, J.; et al. Sub-50-Ns Ultrafast Upconversion Luminescence of a Rare-Earth-Doped Nanoparticle. *Nat. Photonics* **2022**, *16*, 651−657.
(484) Li, G.-C.; Zhang, Q.; Maier, S. A.; Lei, D. Plasmonic Particle-on-Film Nanocavities: A Versatile Platform for Plasmon-Enhanced Spectroscopy and Photochemistry. *Nanophotonics* **2018**, *7*, 1865−1889.
(485) Joshi, G. K.; McClory, P. J.; Dolai, S.; Sardar, R. Improved Localized Surface Plasmon Resonance Biosensing Sensitivity Based on Chemically-Synthesized Gold Nanoprisms as Plasmonic Transducers. *J. Mater. Chem.* **2012**, *22*, 923−931.
(486) Joshi, G. K.; Smith, K. A.; Johnson, M. A.; Sardar, R. Temperature-Controlled Reversible Localized Surface Plasmon Resonance Response of Polymer-Functionalized Gold Nanoprisms in the Solid State. *J. Phys. Chem. C* **2013**, *117*, 26228−26237.
(487) Charles, D. E.; Aherne, D.; Gara, M.; Ledwith, D. M.; Gun'ko, Y. K.; Kelly, J. M.; Blau, W. J.; Brennan-Fournet, M. E. Versatile Solution Phase Triangular Silver Nanoplates for Highly Sensitive Plasmon Resonance Sensing. *ACS Nano* **2010**, *4*, 55−64.
(488) Charles, D. E.; Gara, M.; Aherne, D.; Ledwith, D. M.; Kelly, J. M.; Blau, W. J.; Brennan-Fournet, M. E. Scaling of Surface Plasmon Resonances in Triangular Silver Nanoplate Sols for Enhanced Refractive Index Sensing. *Plasmonics* **2011**, *6*, 351−362.
(489) Richard-Lacroix, M.; Deckert, V. Direct Molecular-Level near-Field Plasmon and Temperature Assessment in a Single Plasmonic Hotspot. *Light Sci. Appl.* **2020**, *9*, 35.
(490) Lin, L.; Peng, X.; Wang, M.; Scarabelli, L.; Mao, Z.; Liz-Marzán, L. M.; Becker, M. F.; Zheng, Y. Light-Directed Reversible Assembly of Plasmonic Nanoparticles Using Plasmon-Enhanced Thermophoresis. *ACS Nano* **2016**, *10*, 9659−9668.
(491) Feng, N.; Shen, J.; Chen, Y.; Li, C.; Hu, Y.; Zhang, L.; Chen, S.; Fan, Q.; Huang, W.; Wang, L. Multifunctional Shape-Dependent Plasmonic Nanoprobe by Enzymatic Etching of Single Gold Triangular Nanoplate. *Nano Res.* **2020**, *13*, 3364−3370.

https://doi.org/10.1021/acs.chemrev.3c00033
Chem. Rev. 2023, 123, 3493−3542

(492) Xia, Y.; Ye, J.; Tan, K.; Wang, J.; Yang, G. Colorimetric Visualization of Glucose at the Submicromole Level in Serum by a Homogenous Silver Nanoprism−Glucose Oxidase System. *Anal. Chem.* **2013**, *85*, 6241−6247.
(493) Luo, X.; Qiao, L.; Xia, Z.; Yu, J.; Wang, X.; Huang, J.; Shu, C.; Wu, C.; He, Y. Shape- and Size-Dependent Refractive Index Sensing and SERS Performance of Gold Nanoplates. *Langmuir* **2022**, *38*, 6454−6463.
(494) Chen, H.; Kou, X.; Yang, Z.; Ni, W.; Wang, J. Shape- and Size-Dependent Refractive Index Sensitivity of Gold Nanoparticles. *Langmuir* **2008**, *24*, 5233−5237.
(495) Najem, M.; Carcenac, F.; Taliercio, T.; Gonzalez-Posada, F. Aluminum Bowties for Plasmonic-Enhanced Infrared Sensing. *Adv. Optical Mater.* **2022**, *10*, 2201025.
(496) Tan, K.; Yang, G.; Chen, H.; Shen, P.; Huang, Y.; Xia, Y. Facet Dependent Binding and Etching: Ultra-Sensitive Colorimetric Visualization of Blood Uric Acid by Unmodified Silver Nanoprisms. *Biosens. Bioelectron.* **2014**, *59*, 227−232.
(497) Zeng, J.; Zhang, Y.; Zeng, T.; Aleisa, R.; Qiu, Z.; Chen, Y.; Huang, J.; Wang, D.; Yan, Z.; Yin, Y. Anisotropic Plasmonic Nanostructures for Colorimetric Sensing. *Nano Today* **2020**, *32*, 100855.
(498) Saa, L.; Coronado-Puchau, M.; Pavlov, V.; Liz-Marzán, L. M. Enzymatic Etching of Gold Nanorods by Horseradish Peroxidase and Application to Blood Glucose Detection. *Nanoscale* **2014**, *6*, 7405−7409.
(499) Zhu, D.; Liu, B.; Wei, G. Two-Dimensional Material-Based Colorimetric Biosensors: A Review. *Biosensors* **2021**, *11*, 259.
(500) Liu, L.; Corma, A. Metal Catalysts for Heterogeneous Catalysis: From Single Atoms to Nanoclusters and Nanoparticles. *Chem. Rev.* **2018**, *118*, 4981−5079.
(501) Zeb Gul Sial, M. A.; Ud Din, M. A.; Wang, X. Multimetallic Nanosheets: Synthesis and Applications in Fuel Cells. *Chem. Soc. Rev.* **2018**, *47*, 6175−6200.
(502) Dai, Y.; Liu, S.; Zheng, N. C_2H_2 Treatment as a Facile Method to Boost the Catalysis of Pd Nanoparticulate Catalysts. *J. Am. Chem. Soc.* **2014**, *136*, 5583−5586.
(503) Andoy, N. M.; Zhou, X.; Choudhary, E.; Shen, H.; Liu, G.; Chen, P. Single-Molecule Catalysis Mapping Quantifies Site-Specific Activity and Uncovers Radial Activity Gradient on Single 2D Nanocrystals. *J. Am. Chem. Soc.* **2013**, *135*, 1845−1852.
(504) Li, Z.; Kurouski, D. Probing the Redox Selectivity on Au@Pd and Au@Pt Bimetallic Nanoplates by Tip-Enhanced Raman Spectroscopy. *ACS Photonics* **2021**, *8*, 2112−2119.
(505) Han, Y.; Yan, Y.; Wu, Z.; Jiang, Y.; Li, X.; Xu, Q.; Yang, X.; Zhang, H.; Yang, D. Facile Synthesis of Pd@Ru Nanoplates with Controlled Thickness as Efficient Catalysts for Hydrogen Evolution Reaction. *CrystEngComm* **2018**, *20*, 4230−4236.
(506) Zhan, C.; Bu, L.; Sun, H.; Huang, X.; Zhu, Z.; Yang, T.; Ma, H.; Li, L.; Wang, Y.; Geng, H.; et al. Medium/High-Entropy Amalgamated Core/Shell Nanoplate Achieves Efficient Formic Acid Catalysis for Direct Formic Acid Fuel Cell. *Angew. Chem., Int. Ed.* **2023**, *62*, No. e202213783.
(507) Feng, Y.; Shao, Q.; Lv, F.; Bu, L.; Guo, J.; Guo, S.; Huang, X. Intermetallic PtBi Nanoplates Boost Oxygen Reduction Catalysis with Superior Tolerance over Chemical Fuels. *Adv. Sci.* **2020**, *7*, 1800178.
(508) Chen, M. S.; Goodman, D. W. The Structure of Catalytically Active Gold on Titania. *Science* **2004**, *306*, 252−255.
(509) Wang, L.; Zhu, Y.; Wang, J.-Q.; Liu, F.; Huang, J.; Meng, X.; Basset, J.-M.; Han, Y.; Xiao, F.-S. Two-Dimensional Gold Nanostructures with High Activity for Selective Oxidation of Carbon−Hydrogen Bonds. *Nat. Commun.* **2015**, *6*, 6957.
(510) Gao, C.; Lyu, F.; Yin, Y. Encapsulated Metal Nanoparticles for Catalysis. *Chem. Rev.* **2021**, *121*, 834−881.
(511) Xu, H.; Shang, H.; Wang, C.; Du, Y. Recent Progress of Ultrathin 2D Pd-Based Nanomaterials for Fuel Cell Electrocatalysis. *Small* **2021**, *17*, 2005092.
(512) Zhou, Y.; Jin, C.; Li, Y.; Shen, W. Dynamic Behavior of Metal Nanoparticles for Catalysis. *Nano Today* **2018**, *20*, 101−120.
(513) Herves, P.; Perez-Lorenzo, M.; Liz-Marzan, L. M.; Dzubiella, J.; Lu, Y.; Ballauff, M. Catalysis by Metallic Nanoparticles in Aqueous Solution: Model Reactions. *Chem. Soc. Rev.* **2012**, *41*, 5577−5587.
(514) Zhang, Y.; Cui, Z.; Li, L.; Guo, L.; Yang, S. Two-Dimensional Structure Au Nanosheets Are Super Active for the Catalytic Reduction of 4-Nitrophenol. *Phys. Chem. Chem. Phys.* **2015**, *17*, 14656−14661.
(515) Ye, S.; Brown, A. P.; Stammers, A. C.; Thomson, N. H.; Wen, J.; Roach, L.; Bushby, R. J.; Coletta, P. L.; Critchley, K.; Connell, S. D.; et al. Sub-Nanometer Thick Gold Nanosheets as Highly Efficient Catalysts. *Adv. Sci.* **2019**, *6*, 1900911.
(516) Balakrishnan, T.; Choi, S.-M. Encapsulation of Atomically Thin Gold Nanosheets within Porous Silica for Enhanced Structural Stability and Superior Catalytic Performance. *New J. Chem.* **2022**, *46*, 18699−18709.
(517) Zhang, Y.; Lucas, J. M.; Song, P.; Beberwyck, B.; Fu, Q.; Xu, W.; Alivisatos, A. P. Superresolution Fluorescence Mapping of Single-Nanoparticle Catalysts Reveals Spatiotemporal Variations in Surface Reactivity. *Proc. Natl. Acad. Sci. U. S. A.* **2015**, *112*, 8959−8964.
(518) Gilroy, K. D.; Ruditskiy, A.; Peng, H.-C.; Qin, D.; Xia, Y. Bimetallic Nanocrystals: Syntheses, Properties, and Applications. *Chem. Rev.* **2016**, *116*, 10414−10472.
(519) Zhang, G.; Cao, D.; Guo, S.; Fang, Y.; Wang, Q.; Cheng, S.; Zuo, W.; Yang, Z.; Cui, P. Tuning the Selective Ethanol Oxidation on Tensile-Trained Pt(110) Surface by Ir Single Atoms. *Small* **2022**, *18*, 2202587.
(520) Maties, G.; Luu, M.; Ait-Oukaci, K.; Lecerf, I.; Marcelot, C.; Fondet, A.; Cayez, S.; Gatel, C.; Blon, T.; Chaudret, B.; et al. Ferromagnetic Ni Nanoparticle with Controlled Anisotropy: From Polyhedral to Planar Tetrapods. *J. Phys. Chem. C* **2022**, *126*, 20668−20677.
(521) Zhou, S.; Wen, M.; Wang, N.; Wu, Q.; Wu, Q.; Cheng, L. Highly Active NiCo Alloy Hexagonal Nanoplates with Crystal Plane Selective Dehydrogenation and Visible-Light Photocatalysis. *J. Mater. Chem.* **2012**, *22*, 16858−16864.
(522) Fedou, J.; Viarbitskaya, S.; Marty, R.; Sharma, J.; Paillard, V.; Dujardin, E.; Arbouet, A. From Patterned Optical Near-Fields to High Symmetry Acoustic Vibrations in Gold Crystalline Platelets. *Phys. Chem. Chem. Phys.* **2013**, *15*, 4205−4213.
(523) Chang, W.-S.; Wen, F.; Chakraborty, D.; Su, M.-N.; Zhang, Y.; Shuang, B.; Nordlander, P.; Sader, J. E.; Halas, N. J.; Link, S. Tuning the Acoustic Frequency of a Gold Nanodisk through Its Adhesion Layer. *Nat. Commun.* **2015**, *6*, 7022.
(524) Yi, C.; Su, M.-N.; Dongare, P. D.; Chakraborty, D.; Cai, Y.-Y.; Marolf, D. M.; Kress, R. N.; Ostovar, B.; Tauzin, L. J.; Wen, F.; et al. Polycrystallinity of Lithographically Fabricated Plasmonic Nanostructures Dominates Their Acoustic Vibrational Damping. *Nano Lett.* **2018**, *18*, 3494−3501.
(525) Yan, Z.; Bao, Y.; Manna, U.; Shah, R. A.; Scherer, N. F. Enhancing Nanoparticle Electrodynamics with Gold Nanoplate Mirrors. *Nano Lett.* **2014**, *14*, 2436−2442.
(526) Lu, J.; Yang, H.; Zhou, L.; Yang, Y.; Luo, S.; Li, Q.; Qiu, M. Light-Induced Pulling and Pushing by the Synergic Effect of Optical Force and Photophoretic Force. *Phys. Rev. Lett.* **2017**, *118*, 043601.

https://doi.org/10.1021/acs.chemrev.3c00033
Chem. Rev. 2023, 123, 3493−3542